Fakultät für Elektrotechnik und Informationstechnik
Technische Universität München

Development of a CO_2 sensor using TDLAS-WMS and its application for emission analysis in Munich

Lijuan Lan

Vollständiger Abdruck der von der Fakultät für Elektrotechnik und Informationstechnik der Technischen Universität München zur Erlangung des akademischen Grades eines

Doktor-Ingenieurs (Dr.-Ing.)

genehmigten Dissertation.

Vorsitzender:
Prof. Dr.-Ing. Thomas Eibert

Prüfende der Dissertation:
1. Prof. Dr.-Ing. Jia Chen
2. Prof. Dr. rer. nat. Mark Wenig,
   Ludwig-Maximilians-Universität München

Die Dissertation wurde am 07.10.2019 bei der Technischen Universität München eingereicht und durch die Fakultät für Elektrotechnik und Informationstechnik am 17.03.2020 angenommen.

Abstract

This thesis develops an in-situ carbon dioxide (CO_2) and water vapor (H_2O) concentrations measurement system based on the TDLAS (tunable diode laser absorption spectroscopy), WMS (wavelength modulation spectroscopy), and VCSEL (vertical-cavity surface-emitting laser). The system gets rid of the calibration process and employs the multi-harmonics to improve the measurement precision. A digital lock-in amplifier (LIA) is built to generate the zeroth to fifth harmonics simultaneously. The RAM (residual amplitude modulation) in the first harmonic has been eliminated so that the first harmonic can be utilized for the gas concentration monitoring. The precision of the measurement system is evaluated by the Allan Deviation analysis and the accuracy is verified by comparing with the commercial NDIR (nondispersive infrared) sensor. The Allan Deviation plots illustrate that the multi-harmonic detection can effectively enhance the precision when the first harmonic is contained in the detection. The first-to-third harmonics detection acquires the best precision of 0.02 ppm for CO_2 and 1.0 ppm for H_2O with a 10-minute integrating time.

The continuous observation of atmospheric CO_2 concentrations was carried out in Munich city center over one year from February 2018 to January 2019. The measurement results are used to study the CO_2 variations and to predict the potential CO_2 emission sources in Munich. The results demonstrate that the ground-based CO_2 concentrations have distinct seasonal, monthly, weekly, and diurnal variations. The urban CO_2 concentrations are affected by various factors, while the VPR (vegetation photosynthesis and respiration) and PBL (planetary boundary layer) height variations dominate the diurnal cycles in warm months. The air parcel backward trajectories are computed to track the air movements based on the HySPLIT (Hybrid Single Particle Lagrangian Integrated Trajectory) model. The winter CO_2 with the trajectory clustering, PSCF (potential source contribution function), and CWT (concentration weighted trajectory) methods are utilized to analyze the anthropogenic activities in Munich. The analyses demonstrate that local emissions have great impacts on urban CO_2 concentrations, with main emission sources at the north and southeast of the measurement site. To better understand the summer CO_2 concentrations, an HLC (hourly lowest concentration) method is proposed to determine the VPR and PBL effects in summer. After eliminating the concentrations caused by the natural factors, the CO_2 concentrations observed in July 2018 can be used for analyzing the anthropogenic activities in summer in urban areas.

Zusammenfassung

In dieser Dissertation wird ein in-situ Messsystem zur Messung der CO_2 und H_2O Konzentration entwickelt basierend auf TDLAS (Tunable Diode Laser Absorption Spectroscopy), WMS (Wavelength Modulation Spectroscopy) und VCSEL (Vertical-Cavity Surface-Emitting Laser). Anstelle des Kalibrierprozesses, nutzt das Messsystem Multi-Harmonische zur Verbesserung der Messgenauigkeit. Es wird ein digitaler Lock-in-Verstärker (LIV) gebaut, um simultan die nullte bis fünfte Harmonische zu erzeugen. Durch die Eliminierung der RAM (residual amplitude modulation) in der ersten Harmonischen, kann die erste Harmonische für die Gaskonzentrationsüberwachung verwendet werden. Die Präzision des Messsystems wird mit der Allan-Deviations-Analyse untersucht und durch den Vergleich mit dem kommerziellen NDIR (nondispersive infrared) Sensor verifiziert. Die Detektion der ersten bis dritten Harmonischen erzielt die höchste Messgenauigkeit von 0,02 ppm für CO_2 und 1,0 ppm für H_2O bei einer Integrationszeit von 10 Minuten.

Die kontinuierliche Messung von CO_2 wurde über den Zeitraum von einem Jahr von Feb. 2018 bis Jan. 2019 in München durchgeführt. Die Messergebnisse werden verwendet, um CO_2 Schwankungen zu untersuchen und potenzielle CO_2 Emissionsquellen in München vorauszusagen. Die Ergebnisse zeigen deutliche saisonale, monatliche, wöchentliche und tageszyklische Schwankungen der bodengebundenen CO_2 Konzentrationen. Die urbanen CO_2 Konzentrationen werden durch verschiedene Faktoren beeinflusst. Die Schwankungen der VPR (Vegetation Photosynthesis and Respiration) und Höhe der PBL (Planetary Boundary Layer) dominieren den tageszyklischen Verlauf während der warmen Monate. Die Rückwärtstrajektorien der Luftteilchen werden anhand des HySPLIT (Hybrid Single Particle Lagrangian Integrated Trajectory) Models berechnet zur Verfolgung der Luftbewegungen. Das Winter CO_2 mit der Trajektorien Clusterbildung, PSCF (potential source contribution function) und CWT (concentration weighted trajectory) Methoden wird zur Analyse der anthropogenen Aktivitäten in München verwendet. Die Analyse zeigt, dass lokale Emissionen einen großen Einfluss auf urbane CO_2 Konzentrationen haben mit Hauptemissionsquellen im Norden und Südosten der Messstelle. Zum besseren Verständnis der Sommer CO_2 Konzentrationen, wird ein HLC (Hourly Lowest Concentration) Model vorgeschlagen, um die VPR und PBL Effekte im Sommer zu bestimmen. Nach Eliminierung, der durch natürliche Faktoren verursachten, Konzentrationen, kann die im Juli 2018 gemessene CO_2 Konzentration zur Analyse der anthropogenen Aktivitäten im urbanen Raum im Sommer verwendet werden.

Contents

1 Introduction

1.1 Background

It is well-known that greenhouse gases (GHG) have significant negative impacts on the environment, e.g. climate change. The total anthropogenic GHG emissions have continued increasing worldwide during the last 60 years. Carbon dioxide (CO_2), one of the dominant GHG, comes mainly from the burning of fossil fuels, cement production and flaring [1]. Figure 1.1 illustrates the atmospheric CO_2 concentration measured at Mauna Loa, Hawaii, starting from March 1958 [2, 3]. The recorded CO_2 (red line) has a seasonal cycle, that is each year during the growing seasons (spring and summer) in Northern Hemisphere, atmospheric CO_2 concentration decreases due to the CO_2 being uptaken by the plant leaves. The seasonally corrected data (black line), however, shows a continuing trend of growth at around 2 ppm (parts per million) per year. Consequently, the atmospheric CO_2 level has now exceeded 410 ppm as shown in Figure 1.1.

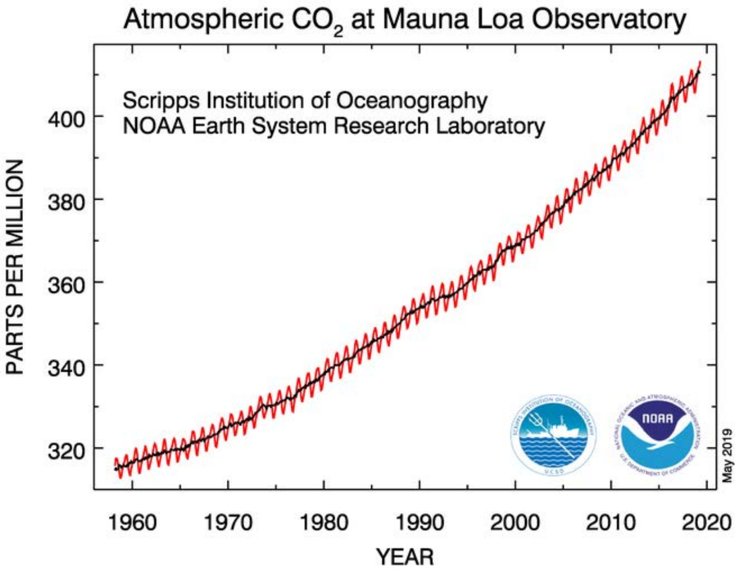

Figure 1.1: Monthly mean atmospheric carbon dioxide at Mauna Loa Observatory, Hawaii (started from March of 1958). The red periodic oscillation curve represents the monthly mean CO_2 data measured as the mole fraction in dry air (ppm) and the black line through the curve is the data after correction for the seasonal average cycle [2].

Research has found that cities and their surroundings sustain around 54% of the global population (WHO (2014)) but contribute nearly 70% of the total anthropogenic CO_2 emissions (UNHabitat (2011)) [4, 5]. Thus, an accurate, compact, portable, and long-term measurement system is urgently needed in environmental sensing in order to better study the CO_2 distribution and seasonal cycle near the ground. It will also be useful for the real-time measurement of CO_2 concentration in all weather conditions, for accurately monitoring and controlling the source of carbon emission in urban areas, and for helping with the urban pollutant emission modeling and for supplying some policy supports to the government.

1.2 Methodologies

Joseph von Fraunhofer invented the first spectroscope in 1814, followed by a series of scientific discoveries that set the fundamentals for modern spectroscopy and also quantum physics. The Fraunhofer lines, which are named after him, are dark lines in the sun spectrum. Back then, he assumed the discrete dark lines were part of the sun spectrum itself. His drawing can be seen in Figure 1.2 [6, 7]. Today, people know that the Fraunhofer lines (also known as the absorption lines) occur at a particular wavelength when the sunlight is absorbed by atoms and ions of elements - namely O_2, Na, H, He, Fe, Mg, which create the best-known Fraunhofer lines in the solar atmosphere. Due to the characteristic fingerprints of the Fraunhofer lines, nowadays the lines are widely used in element and gas detections.

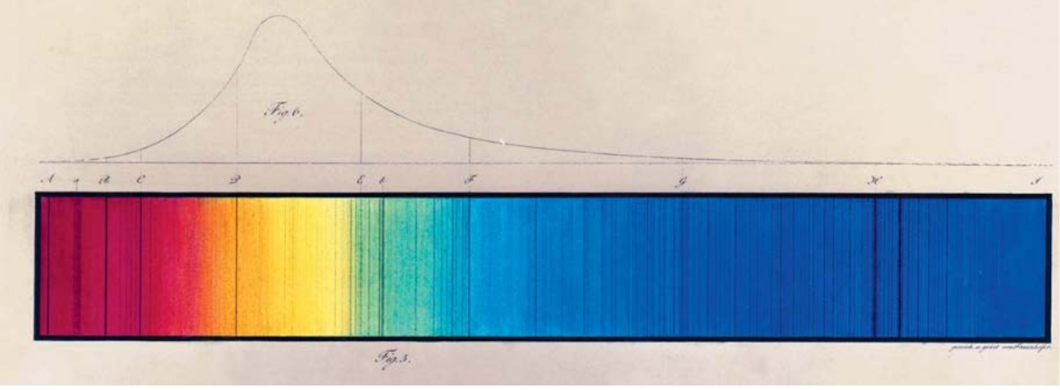

Figure 1.2: The original drawing by Fraunhofer showing black lines in the sun spectrum [6].

There are many techniques to measure atmospheric CO_2 concentration, but the spectroscopic methodologies are the main methods since they are non-contact, fast response and non-interfering with the measured medium [8]. The methodologies can be separated into the satellite measurement, ground-based remote sensing, and in-situ measurement.

Space-based sensing with satellites is a prevailing tool to achieve global observation of atmospheric CO_2 [9]. Currently, there are several satellites that have the capacity of CO_2 mapping in active service: Atmospheric Infrared Sounder (AIRS) by NASA [10, 11], Greenhouse Gases Observing Satellite (GOSAT, GOSAT-2) by Japan Aerospace Exploration Agency (JAXA) [12–14], Orbiting Carbon Observatory 2 and 3 (OCO-2, OCO-3) by NASA [15–18], Chinese Earth observation satellite known as TanSat (or CarbonSat)[19–22], Greenhouse Gas Satellite - Demonstrator GHGSat-D (nicknamed Claire) satellite by Canada [23]. The spectrometers of the satellites are passive optical instruments, which make use of the sunlight spectra, designed to map the CO_2 concentration in two bands (around 1.6 μm and 2 μm) using a passive infrared spectrometer with an echelle grating, whose spectral resolution is about 0.5 cm^{-1} [24, 25]. However, these spectrometers only work in the daytime, and are prone to various interferences, e.g. clouds and aerosols; usually the sensitivity in the lowermost layer of the troposphere, with strong gradient gas distribution, is typically not high due to the unfavorable weighting function, of which the spectrometers cannot measure accurately at high latitudes [9]. Moreover, because of the large observational footprint and periodical orbiting of the space-based satellite, it is hard to estimate the GHG concentration at a high spatial and temporal resolution.

Figure 1.3: TCCON stations all over the world [26].

Fourier Transform Infrared (FTIR) spectroscopy can be performed by a broadband infrared spectrometer using interferometry, e.g. based on a Michelson interferometer. The input light is first divided into two beams by a beam splitter, and then combined into one beam again during which the optical path difference is adjusted by the movable reflection mirror in one arm. Their interferogram is recorded by a detector which covers all the spectral information and the true spectrum is retrieved from a Fourier transform of the interferogram. FTIR has been widely used for the gas measurement. With regard to the atmospheric CO_2, a ground-based worldwide FTIR network, i.e., the Total Carbon Column Observing Network (TCCON) [27, 28], has been established with 30 stations distributed all over the world presently, as shown in Figure 1.3 [26, 29]. TCCON uses near-infrared solar spectral absorption to accurately and precisely retrieve column-averaged abundance of CO_2 and other gases (CH_4, N_2O, HF, CO, H_2O, and HDO). For convenient measurement, the EM27/SUN is a miniature ground-based tabletop FTIR spectrometer that can be employed in urban GHG emission studies in various locations [30–32]. We have developed a completely automated enclosure for the EM27/SUN and performed differential column measurements to detect the CO_2 and CH_4 emissions in urban areas [33–36]. However, since the instrument utilizes solar light as light source, it has limitations in its application. For example, the measurement can only be carried out in the presence of sunshine, thus, concentration data for rainy days and at night cannot be collected. Also, the column concentration is the average of the light range between the earth and the sun, rather than the concentration at the ground-level.

Nondispersive infrared (NDIR) spectrometry and cavity ring down spectrometry (CRDS) are two common techniques used in the in-situ CO_2 concentration measurement, and they can detect the emission sources with high precision and sensitivity. NDIR uses a continuous broadband infrared light as the light source. When the light beam passes through the measured gas, certain light wavelengths will be absorbed by the gas, and then the gas concentration can be deduced by the light attenuation at specific wavelengths according to the Beer-Lambert Law. The main components of the NDIR sensor are an infrared light source and an infrared photodetector, in front of which is an optical filter or a monochromator whose focus wavelength is the absorption line of the gas of interest [37–40]. The NDIR sensor measures the gas concentration based on the attenuation of the infrared light; while the light intensity without gas absorption should be detected by a reference cell. For this reason, the light intensity should be calibrated periodically or using an additional reference chamber, which is filled with standard gas or none absorbing gas, is set in the system to measure the initial light intensity. Thus, NDIR has some disadvantages such as the frequency instability of the optical filter due to the control exacted by the piezo, which would susceptible lead to longtime drift. As a result, the researchers must periodically calibrate the accuracy of the instrument.

In CRDS, two or more high reflectivity mirrors (reflectivity of 99.999%) are formed in a gas cell with thousands of reflection paths so that the effective path length can be extended to many kilometers [41–44]. Therefore, CRDS enables the monitoring of trace gases to the ppb (parts per billion) or even smaller levels. Hence, it is a highly sensitive optical spectroscopy instrument specified for the trace gases detection. However, the high costs of the high-finesse optical cavity and the high reflectivity mirrors, and the difficulties in the light path adjustment and maintenance are the disadvantages of the CRDS. Moreover, similar to NDIR, CRDS should be calibrated periodically or the data captured from the instrument must be corrected all the time.

1.3 TDLAS

Tunable diode laser absorption spectroscopy (TDLAS) is suited for trace gas in-situ monitoring because the tunable diode laser scans across the absorption line at extremely small bandwidth. The bandwidth is in an order of 1×10^{-3} cm^{-1} (around 30 MHz) or smaller, which is about one tenth of the linewidth [45–47]. The absorption line profile can be detected in more detail so that TDLAS becomes a highly sensitive approach for gas monitoring. When combined with the wavelength modulation spectroscopy (WMS), TDLAS can effectively remove the noise and improve sensitivity, precision, and signal-to-noise ratio (SNR) in harsh environments and in trace gases measurements [48–51]. Unlike the traditional distributed-feedback (DFB) laser, the vertical-cavity surface-emitting laser (VCSEL) has many unique features, such as low power consumption, fast frequency modulation responses and wide wavelength tuning range which covers several absorption lines. The wide tuning VCSEL can be used to measure different gas species simultaneously, because the VCSEL scans across more than 10 nm which contain several absorption lines [52–61].

Due to the random variation of the initial phase, the TDLAS-WMS harmonics are randomly assigned to the X and Y axes in the lock-in amplifier (LIA). Hence, to obtain the complete harmonic signal, the most common methods are to manually adjust the reference signal phase or to use the scalar of the two axes. The former method is inconvenient in the practical measurement, while the latter one is widely used in the traditional second harmonic detection. The first harmonic has the highest SNR among the harmonics, so theoretically it should have a higher precision than the second harmonic in the gas concentration measurement. In the well-known "calibration-free $nf/1f$" method, the first harmonic is treated as the light intensity signal to normalize the other harmonics [62–64]. However, the first harmonic contains the residual amplitude modulation (RAM) signal, which should be acquired from the absorption-free condition. RAM is always characterized carefully prior to the measurement or from a separated laser beam. Those RAM characterization processes make the "calibration-free $nf/1f$" approach an uncompleted calibration-free algorithm and the operations are inconvenient and complex [65]. Moreover, the RAM in the first harmonic is much stronger than that in the other harmonics. When using the wide tuning VCSEL, the RAM deforms the first harmonic as a non-linear offset with a gradient. Therefore, the magnitude of the X and Y components in the first harmonic cannot be employed directly to infer the gas concentration.

People prefer to use the second harmonic for gas measurement because of its high SNR in the spectrum center [66], the other harmonics, especially the odd order harmonics, are always ignored for their low SNR at the line center. However, each harmonic contains useful information about the gas parameters and only using one or two harmonics would waste the information as well as reduce the measurement precision. Scientists have studied the multi-harmonics for a long time. For example, Johnstone used the RAM in the first harmonic to recover the absorption line shape based on the phasor decomposition method. However, this method is valid under small modulation index ($m < 0.5$) which leading to low harmonic SNR. Nonetheless, it can be used for any m values if the tuning coefficient is given and higher harmonics are employed [67–70]. An external optical fiber and the balanced detection were applied to null RAM in the intensity modulated experiment, which increased the complexity in operation and signal processing [71–73]. Hangauer utilized multi-harmonic to reconstruct the transmission [74–76]. Peng employed the first harmonic and odd-harmonic to recover the absorbance shape [77, 78]. The ratios of the second and fourth harmonics at different modulation depths are employed for calculating the line shape [79, 80]. Among the approaches, the m was extended to higher values ($m > 2.0$).

In Chen's research, the one axis harmonic was utilized to measure the carbon monoxide (CO) concentration based on the linear least square curve fitting (LLSCF) algorithm [75, 81–85]. However, they have concluded that the second harmonic detection had better noise performance than the first harmonic detection. That is because the RAM was treated as a linear slope, which reduced the precision for the first harmonic detection. Chen also proposed a calibration-free method for CO sensing using the VCSEL laser [85]. The calibration-free method refers to the current to wavelength calibration. That is, the CH_4 absorption lines are utilized to calibrate the wavelength of the weak CO absorption line. In the algorithm, the zeroth harmonic is treated as incident light intensity to normalize other harmonics. Nevertheless, they only discussed one single harmonic and one absorption line in the detection.

1.4 Overview of Study

According to the aforementioned discussions, the main works of the study can be outlined in 10 points as follows:

(1) **The principle of TDLAS-WMS**: the basic principle of the TDLAS is introduced combined with the definitions of the line profiles (Gaussian, Lorentzian and Voigt Profiles) and broadenings (Doppler and pressure broadenings). The formula derivations of the WMS are presented with the higher orders sinusoidal modulation intensities. Thus, the expressions of the harmonic signals are obtained and the reference signal phase shift in the lock-in amplifier can be decided based on the deduced formulas.

(2) **Eliminate RAM signal in the first harmonic**: the RAM in the first harmonic is so strong that the harmonic is submerged in the RAM. The RAM signal is subtracted using the divided axes such that the first harmonic can be used for concentration measurement. The results illustrate that the first harmonic detection has better noise performance than the second or third harmonic detection.

(3) **Utilize the wide scanning range first harmonic for gas detection**: VCSEL enables the laser to scan at a wide wavelength range so that several gas species can be detected simultaneously.

(4) **A digital lock-in amplifier (LIA) to produce multi-harmonic**: the zeroth to fifth harmonic can be demodulated via the digital LIA synchronously. Moreover, the concentration-dependent harmonic and concentration-independent RAM signals are assigned to the X and Y axes automatically.

(5) **Multi-harmonic detection**: the multi-harmonic detection effectively improves the measurement precision when compared with the single harmonic detection.

(6) **Build up an automatic self-calibrated measurement system**: the system achieves characteristic of self-calibration because some intermediate properties in the measurement such as the light intensity, modulation depth, and wavelength are automatically inferred in the signal processing.

(7) **Continuously measure CO_2 concentration over one year in Munich**: the whole year measurement is implemented in Munich city center from February 2018 to January 2019. The results are helpful for studying the CO_2 variations in urban areas. Moreover, numerous data source, such as the wind speed and wind direction, the meteorological data, SIF from the OCO-2 satellite, are introduced for better interpretation the urban CO_2 concentration variations.

(8) **Utilize the HySPLIT model for air mass backward trajectory analysis**: the air mass backward trajectories are computed based on the HySPLIT (Hybrid Single Particle Lagrangian Integrated Trajectory) model, and the PSCF (potential source contribution function) and CWT (concentration weighted trajectory) methods are used to predict the potential emission sources. The winter CO_2 is utilized to analyze the anthropogenic activities in Munich in the wintertime. The results indicate that the PSCF is superior in predicting potential sources compared to the CWT when trajectories are unevenly distributed.

(9) **HLC method for determining the background concentration in summer**: propose a method to determine the CO_2 sources and sinks from the natural parts (VPR and PBL effects) which are served as the background concentration in the summer data. The HLC is used to analyze the July CO_2 and concludes that it is valid to analyze the anthropogenic activities in summer in urban areas.

(10) **Summary of the work and discussion of future improvements**: the entire work is summarized and some possible improvements and further advices of extensive works are discussed as the future research.

The detailed representation of the present study is divided into 6 chapters.

◇ **Chapter 2** will present the basic principle of the TDLAS and WMS. The Beer-Lambert Law is described at the very beginning together with the line strength and the dominant broadenings of the absorption line. The WMS theory is then introduced with the high-order light intensities and the phase shifts in the sinusoidal modulation. The expressions of the harmonics are derived. The relationship between the LIA reference signal phases and the phase shifts in the modulation are discussed. Under weak absorbance, the harmonic signals can be simplified and the zeroth harmonic approximates to the central light intensity. The error analysis of the approximation are discussed. The modulation intensities are employed to study the RAM effects in the different harmonics. Moreover, the modulation index in the first to fourth harmonics to presented in order to find a suitable modulation index range for multi-harmonic detection.

- ◇ **Chapter 3** will give the introduction of the experimental setup. The experimental components of the experimental setup are presented. A DAQ is served as the signal generator and recorder. The signal processing of the system is programmed in LabVIEW software platform, in which the system is able to control the DAQ, to generate the multiple harmonics and to calculate the gas concentration. The digital LIA is developed to produce the multiple harmonics from zeroth to fifth harmonics, and to eliminate the RAM signal in the first harmonic. The signal processing enables the measurement system to be a self-calibrated sensor, because the calibrations of the wavelength and the light intensities, and the determinations of the modulation depth and modulation index are automatically implemented in the process, and the gas concentrations are obtained without additional calibration. Furthermore, the absorption lines near 2004 nm (CO_2 and H_2O) and 2365 nm (CO and CH_4) which obtained from the HITRAN database are discussed in this chapter.

- ◇ **Chapter 4** will describe the performance of the measurement system, which includes the first harmonic detection and the multi-harmonic detection. The first harmonic detection with different scanning ranges and the multi-harmonic detections with three absorption lines are demonstrated, and the results are also compared with the second and third harmonic detections. Allan Deviation method is utilized to evaluate the precision of the sole-harmonic and multi-harmonic detections. The results conclude that the multi-harmonic detection can effectively improve the noise level and measurement precision. Multi-harmonic detection which contains the first harmonic has the higher precision than that excludes the first harmonic. The deviations are 0.02 ppm for CO_2 and 1.0 ppm for H_2O with a 10-minute integrating time. A commercial NDIR is used to compare the measurement of the developed system. The results reveal the high accuracy of the TDLAS-WMS sensor and the high consistency between these two sensors. The measurements in 2017 are preliminarily displayed the diurnal cycles of the ground-based CO_2 concentrations.

- ◇ **Chapter 5** will depict the one-year continuous measurement results in Munich. Some meteorological data, such as the ambient temperature, the wind speed and direction, the PBL (planetary boundary layer) height, the SIF (solar-induced fluorescence) data from the OCO-2 satellite, are utilized for the interpretations on the CO_2 daily, weekly, monthly and seasonal patterns. The analysis results illustrate that the CO_2 concentration in urban areas is an integrative role combining the vegetation photosynthesis and respiration (VPR), the meteorological conditions (PBL) and the local anthropogenic activities.

- ◇ **Chapter 6** will demonstrate the analysis on the observed CO_2 concentrations based on the HySPLIT model. At first, the basic principles of the HySPLIT method, the trajectory clustering, PSCF, and CWT methods are presented. Then, the winter CO_2 concentrations with the PSCF and CWT mapping methods are employed to predict the probable emission sources in Munich. The comparison between the PSCF and CWT methods is discussed. After that, some background concentrations obtained from the remote sites (ZSF, Zugspitze Schneefernerhaus, and HPB, Hohenpeißenberg) are employed as the background concentrations to analyze the summer CO_2 in Munich. Moreover, the weekend data is employed as the background concentration to study the CO_2 emissions during the workdays. Afterwards, the HLC method is proposed to determine the VPR and PBL effects in the summertime. Finally, the July 2018 CO_2 which eliminated the background concentration is utilized for analyzing the potential emission sources in urban areas. The differences among these methods are discussed, and it concludes that the HLC method can be used for the summer CO_2 analysis in urban areas.

◇ **Chapter 7** summarizes the whole work in the study. Some possible improvements and expansions of the measurement system, as well as some further accurate models and analyses are discussed as the possibilities for working in the future.

2 Theory of TDLAS-WMS

This chapter is the theory foundation of the study. At first the basic principle of TDLAS and is outlined; and the introductions of the line strength, the line profiles and the direct TDLAS for gas concentration measurement are also presented in the first section. Then, the theory of the WMS technique is expressed in the second section. The formula expressions of the harmonic signals, as well as the RAM signal and the phase shifts in WMS, are explained in this part. Subsequently, the simplifications of the harmonic signals under weak absorbance are discussed. The self-calibrated gas concentration measurement approaches based on the first harmonic and multi-harmonic are finally proposed. Some of the content has been published in Lan et al. 2019 [86].

2.1 Basic Theory of TDLAS

In terms of the absorption spectrum, the molecule at a low energy state can be excited to a high energy level when the molecule meets with a photo whose energy matches the energy difference between the two quantum mechanical states of the molecule. Different molecules have different energy levels so that theoretically their own absorption spectrums are easily distinguished in the energy transitions. For this reason, the characteristic fingerprints of the absorption spectrum enable to infer the gas properties such as the composition, concentration, pressure, and temperature, by measuring the absorption lines [87].

2.1.1 Beer-Lambert Law

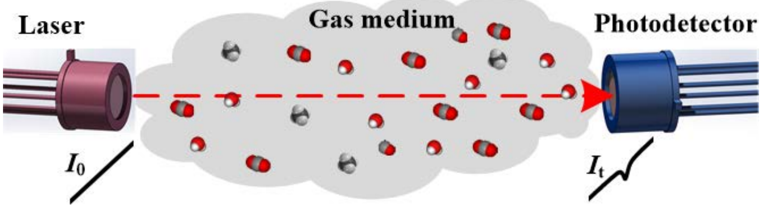

Figure 2.1: The schematic diagram of the Beer-Lambert Law, the symbols of I_0 and I_t and their curves in the diagram denote the intensities of the initial laser light and the transmitted laser light.

TDLAS is the acronym of tunable diode laser absorption spectroscopy. It measures the light attenuations given by the gas absorptions. By controlling the driving temperature and driving current, the wavelength emitted from a laser can be tuned at a very small bandwidth, in an order of 30 MHz or smaller, which is about one tenth of its absorption line width. Therefore, TDLAS is uniquely suited for trace gases detection given its properties of non-contact, high sensitivity, high precision and rapid response, and so on.

The basic principle of TDLAS is described by the Beer-Lambert Law. As displayed in Figure 2.1, when a monochromatic laser beam travels through the measured gas medium, the laser light can be absorbed by the gas molecules at a specified wavelength (wavenumber). The transmission of the laser light intensity is described as [45, 76, 83]:

$$\begin{aligned} \tau(v) &= \frac{I_t}{I_0} = \exp[-\alpha(v)] \\ &= \exp[-PS(T)CL\varphi(v)], \end{aligned} \tag{2.1}$$

where τ is the laser transmission; I_0 and I_t are the incident and transmitted laser light intensities, respectively; α is the absorbance; v [cm^{-1}] is the wavenumber, the relationship between the wavenumber and the wavelength (λ [nm]) is: $v = 1/\lambda$; $\alpha(v) = PS(T)CL\varphi(v)$, where P [atm], $S(T)$ [cm^{-2}/atm], C, and L [cm] are the total gas pressure, line strength, gas concentration, and absorbing path length, respectively; and $\varphi(v)$ [cm] is the line profile, which will be discussed in the following Section 2.1.3.

2.1.2 Line strength

The line strength $S(T)$ represents the strength of a absorption line. It is a temperature-dependent parameter and can be obtained from the HITRAN (HIgh-resolution TRANsmission) molecular absorption database, which is a compilation of spectroscopic parameters and can be used for predicting and simulating the transmissions and emissions of the spectroscopy [88]. The line strength data in HITRAN database is in a unit of [cm^{-1}/(molec·cm^{-2})], the following conversion formula is utilized to transform the unit in the HITRAN database into the unit of [cm^{-2}/atm]:

$$\begin{aligned} & S(T)[\mathrm{cm^{-2}/atm}] = S(T)[\mathrm{cm^{-1}/molec\cdot cm^{-2}}] \times \frac{N[\mathrm{molec}]}{PV[\mathrm{cm^3\cdot atm}]} \\ &= S(T)[\mathrm{cm^{-1}/molec\cdot cm^{-2}}] \times \frac{n[\mathrm{mol}]\cdot N_A[\mathrm{molec\cdot mol^{-1}}]\cdot atm[\mathrm{atm/Pa}]}{P[\mathrm{Pa}]V[\mathrm{m^3}]\times 10^6[\mathrm{cm^3\cdot m^{-3}}]} \\ &= S(T)[\mathrm{cm^{-1}/molec\cdot cm^{-2}}] \times \frac{N_A[\mathrm{molec\cdot mol^{-1}}]\cdot atm[\mathrm{atm/Pa}]}{R[\mathrm{Pa\cdot m^3\cdot mol^{-1}\cdot K^{-1}}]T[\mathrm{K}]\times 10^6[\mathrm{cm^3\cdot m^{-3}}]} \\ &\approx S(T)[\mathrm{cm^{-1}/molec\cdot cm^{-2}}] \times \frac{7.339\times 10^{21}}{T[\mathrm{K}]}[\frac{\mathrm{molec}}{\mathrm{cm^3\cdot atm}}]. \end{aligned} \tag{2.2}$$

where atm is the standard atmosphere with value of 101325 Pa; N_A is the Avogadro constant. The ideal gas law is applied in Eq. 2.2, that is: $PV = nRT$ and R is the ideal gas constant with value of 8.314 J/(mol·K); V [m^3], T [K] and n [mol] are the gas volume, temperature, and the number of moles of gas, respectively. The line strength is a vital factor to determine the measurement sensitivity when the other parameters are given. In infrared range, the longer the wavelength generally results in the higher the line strength. For example, the CO_2 gas molecule near 2.0 μm is about 50 times stronger than the absorption lines at 1.4 μm but more than 1000 times weaker than the absorption lines at 4.3 μm.

2.1.3 Line profile

The absorption line is not an exact "line" but has a certain broadening width. In general, the Doppler broadening and the pressure broadening are dominant. The line profiles ($\varphi(v)$) and their corresponding line widths (γ [cm^{-1}], also named half width at half maximum (HWHM)) are described in the follows.

2.1.3.1 Doppler broadening (Gaussian profile)

Doppler broadening is given by the Doppler Effect. The gas molecules would present another frequency of light when they are traveling. In most cases, the molecule motion is caused by the thermal motion. Then, the broadening is determined only by the mass of the molecule, the temperature and the line wavelength. The Doppler broadening is thus can be used to infer the gas temperature. Moreover, because the molecule velocity in x-, y- or z- direction is distributed as the Gaussian function, the Doppler broadening is described as the Gaussian profile, which is given as [83, 87]:

$$\varphi_G(v) = \frac{1}{\gamma_G} \cdot \sqrt{\frac{\ln 2}{\pi}} \cdot \exp[\frac{-\ln 2 \cdot (v - v_0)^2}{\gamma_G^2}], \tag{2.3}$$

where v_0 [cm^{-1}] is the center wavenumber of absorption line when the absorbance is maximum. The line width of the Gaussian profile, γ_G [cm^{-1}], is expressed as:

$$\begin{aligned} \gamma_G &= v_0 \sqrt{\frac{2 \ln 2 \cdot k_B T}{Mc^2}} \\ &\approx 3.581 \times 10^{-7} v_0 \sqrt{\frac{T}{Mr}}, \end{aligned} \tag{2.4}$$

where M [g/mol] is the molar mass and Mr is the relative molecular mass, they have the same value but vary in unit; k_B [$\mathrm{m}^2\mathrm{kgs}^{-2}\mathrm{K}^{-1}$] is the Boltzmann constant. Here, c [m/s] is defined as the light speed.

2.1.3.2 Pressure broadening (Lorentzian profile)

Pressure broadening occurs because of the collisions of atoms/molecules with the neighboring particles. Due to the increasing gas pressure and intense presence of electrons and ions, the spectral lines tend to be broadened or narrowed. The spectral line is presented by the Lorentzian Profile [83, 87]:

$$\varphi_L(v) = \frac{1}{\pi} \cdot \frac{\gamma_L}{(v - v_0)^2 + \gamma_L^2}, \tag{2.5}$$

where γ_L [cm^{-1}] is the line width of the Lorentzian Profile, and it is determined by:

$$\gamma_L = P[C\chi_{self} + (1 - C)\chi_{air}], \tag{2.6}$$

where χ_{self} [cm^{-1}/atm] and χ_{air} [cm^{-1}/atm] are the coefficients of self and air collisional broadening, respectively. The coefficients can be acquired from HITRAN database.

2.1.3.3 Voigt profile

When both pressure and Doppler broadenings are dominant, Voigt profile would be utilized for describing the line profile. The Voigt profile is the convolution of the Gaussian and Lorentzian profiles [83]:

$$\varphi(v) = \varphi_G(v) * \varphi_L(v). \tag{2.7}$$

However, there is no analytical closed-form expression for the Voigt profile. In this study, a weighted combination of Lorentzian and Gaussian profiles is used to approximate the Voigt profile [89]:

$$\varphi(v) = \frac{c_L}{\pi} \cdot \frac{\gamma}{(v - v_0)^2 + \gamma^2} + \frac{c_G}{\gamma} \cdot \sqrt{\frac{\ln 2}{\pi}} \cdot \exp[\frac{-\ln 2 \cdot (v - v_0)^2}{\gamma^2}], \tag{2.8}$$

where c_L and c_G are the weights of the Lorentzian and Gaussian profiles; their expressions are given as follows:

$$\begin{cases} c_L = 0.68188 + 0.61293d - 0.18384d^2 - 0.11568d^3 \\ c_G = 0.32460 - 0.61825d + 0.17681d^2 + 0.12109d^3, \end{cases} \tag{2.9}$$

where d is defined as $d = (\gamma_L - \gamma_G)/(\gamma_L + \gamma_G)$. Thus, $d \in [-1, 1]$; when d = 1, the line is the Lorentzian profile, while d= -1 would display the Gaussian profile. And the line width of the Voigt Profile (γ [cm^{-1}]) is approximately expressed as:

$$\gamma = 0.5346\gamma_L + \sqrt{0.2166 \cdot \gamma_L^2 + \gamma_G^2}. \tag{2.10}$$

The simulations of the different profiles (Gaussian, Lorentzian and Voigt) are displayed in Figure 2.2 where the prerequisites are that the line widths of these three line profiles are the same (as shown in the figure). From the curves, we can find that the Gaussian profile has the highest value near the line center and the energy distribution is centered at the line center. The Lorentzian profile extends its energy to a wider adjacent range with a squat outline. The Voigt profile locates between the Lorentzian and Gaussian profiles. The Voigt line profile is utilized as the absorption line profile in the thesis.

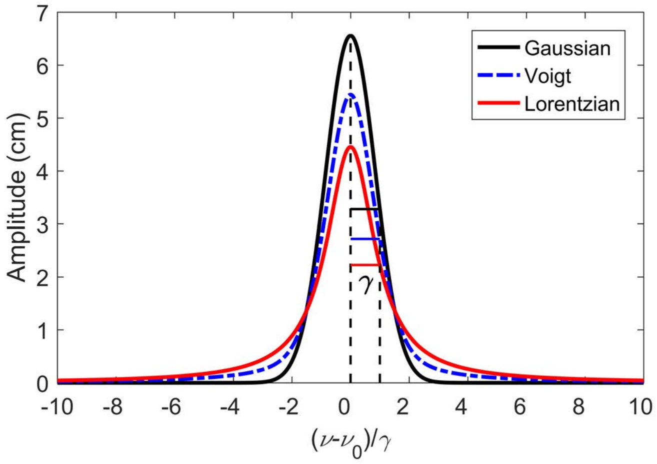

Figure 2.2: Line profile simulations at different broadenings with the same line widths.

In our study at the room temperature and atmospheric pressure, the pressure broadening, which is affected by the gas pressure and concentration (or the partial pressure), is more dominant than the Doppler broadening. That is, the Gaussian profile only takes a small proportion in the line profile. As our analysis, the temperature fluctuations, which result in the Doppler broadening, would lead to a negligible measurement error (less than 1.0 %).

2.1.4 Direct TDLAS

According to Eq. 2.1, the gas concentration (C) can be inferred at the absorption line center (v_0) when the peak line profile ($\varphi(v_0)$) , the pressure (P), temperature (T), and path length (L) are given [77]:

$$C = \frac{\alpha(v_0)}{PS(T)L\varphi(v_0)}. \tag{2.11}$$

In the process, the absorbance line profile in Figure 2.3(b) is obtained from the absorption signal as the black curve in Figure 2.3(a). The signal adjacent the absorption center which is the absence of gas absorption is served as the background signal. The baseline is computed using the polynomial curve fitting algorithm. The absorption signal and the baseline are utilized to calculate the absorbance line profile by the logarithm according to Eq. 2.1.

On the other hand, when we quadrature over the entire wavenumber with the absorbance line profile, the gas concentration can then be inferred from the following formula:

$$C = \frac{\int_{-\infty}^{+\infty} -\alpha(v)\mathrm{d}v}{PS(T)L} = \frac{A}{PS(T)L}, \tag{2.12}$$

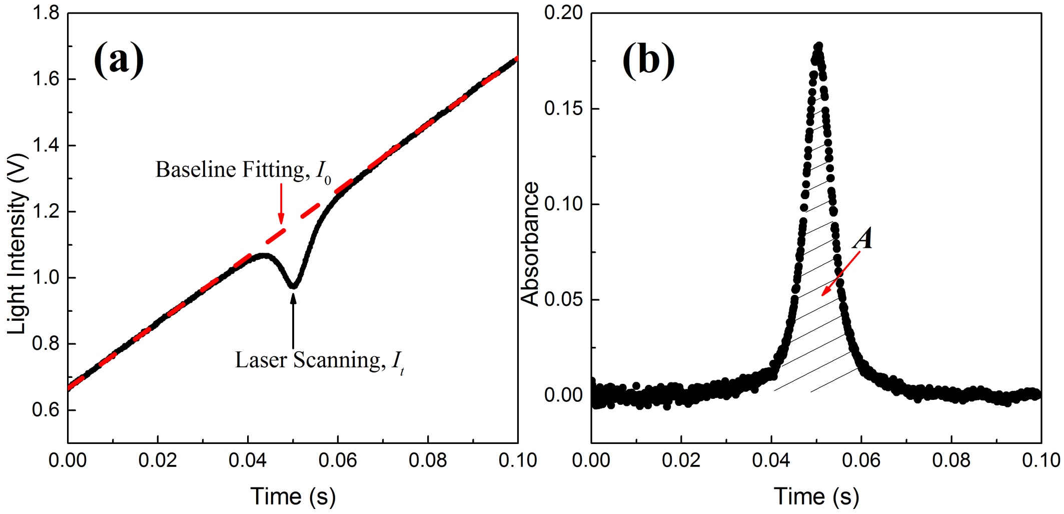

Figure 2.3: Direct TDLAS.

where A is the integral area of the absorbance. The integral value can enhance the accuracy for there might be some signal fluctuations at the peak point. Sometimes, a line profile fitting is implemented before the integral calculation so that the noise among the absorbance line can be removed. The formulas in Eq. (2.11) and 2.12 are also called as the direct absorption spectroscopy (Direct TDLAS). This method has many advantages such as easy operation and can perform absolute concentration without the calibration process. However, Direct TDLAS is easily affected by $1/f$ noise, laser intensity fluctuations, and baseline fitting errors. Those disadvantages often prevent the measurement accuracy, particularly in harsh environments or under weak absorbance conditions.

2.2 Wavelength Modulation Spectroscopy (WMS)

2.2.1 Theory of WMS

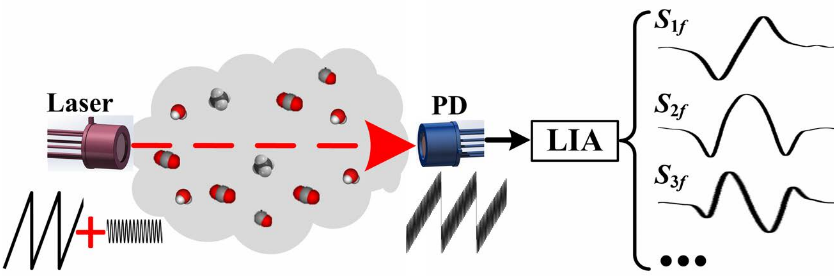

Figure 2.4: Wavelength modulation spectroscopy (WMS)

Wavelength Modulation Spectroscopy (WMS) is a method for sensitive absorbance measurements. Due to its advantages of efficient noise suppression, for example, insusceptible to $1/f$ noise, WMS enables to increase the sensitivity, precision and SNR in the trace gas measurements and in the harsh environments. In TDLAS-WMS, a high-frequency sinusoidal signal with small amplitude is riding on a low-frequency but long-scanning range laser injection current, and then the laser wavelength is modulated by these two signals. Instead of the transmission spectrum, the harmonic signals are obtained via the LIA [48, 66, 77, 78, 86, 90]. The instantaneous laser emitted wavenumber (v) can be written as:

$$v(t) = \overline{v} + a\cos(\omega t + \eta), \tag{2.13}$$

where $\overline{v}$ [cm^{-1}] is the central wavenumber, which is also the wavenumber of the central laser emission without the sinusoidal modulation and implemented by the slow ramp signal; a [cm^{-1}] is the modulation depth and the modulation index is defined as the modulation depth divided by the line width: $m = a/\gamma$; ω [rad/s] is the modulation angular frequency; and η [°] is the phase shift in wavelength with respect to the tuning current. It should be noted that the η is an arbitrary value in each measurement since the start recording point of the waveform is unfixed. The η will be discussed in the LIA part (Section 2.2.2).

When modulated by the high-frequency sinusoidal signal, the instantaneous emitted laser intensity (I_0) will become complex as shown in Eq. 2.14:

$$I_0(t) = \overline{I_0} + \sum_{k=1}^{\infty} I_k \cos(k(\omega t + \eta) + \psi_k), \tag{2.14}$$

where $\overline{I_0}$ denotes the central light intensity which is determined by the ramp signal; I_k is the k-th order sinusoidal modulation intensity; and ψ_k is the phase shift between the wavelength modulation and the k-th order light intensity modulation; the ψ_k are fixed when the modulation frequency (ω) is given. The ($\psi_k + k\eta$) is defined as the k-th order light intensity phase and θ is defined as: $\theta = \omega t + \eta$. When expanded the laser transmittance in Eq. 2.1 by the Fourier series:

$$\begin{aligned} \tau(\overline{v} + a\cos\theta) &= \frac{I_t}{I_0} = \exp[-\alpha(\overline{v} + a\cos\theta)] \\ &= \sum_{k=0}^{\infty} A_k \cos k\theta, \end{aligned} \tag{2.15}$$

where A_k is the k-th order Fourier component of the transmittance:

$$\begin{cases} A_0 &= \frac{1}{2\pi}\int_{-\pi}^{\pi} \tau(\overline{v} + a\cos\theta)\mathrm{d}\theta \\ A_k &= \frac{1}{\pi}\int_{-\pi}^{\pi} \tau(\overline{v} + a\cos\theta)\cdot\cos k\theta\cdot\mathrm{d}\theta, k = 1,2,3\cdots. \end{cases} \tag{2.16}$$

When there is no absorption in the spectroscopy, the laser transmittance is 1. Thus, according to Eq. 2.16, A_0=1 and A_k =0 ($k = 1,2,3\cdots$). When the laser is absorbed by certain gas media, the odd-order Fourier components of the transmittance at the line center are: $A_{2k-1}(v_0)$ =0 based on the symmetry of the absorption line. When substituting Eq. 2.14 into Eq. 2.15, the transmitted light intensity can be expressed as:

$$I_t = I_0\tau = [\overline{I_0} + \sum_{k=1}^{\infty} I_k \cos(k\theta + \psi_k)](\sum_{k=0}^{\infty} A_k \cos k\theta). \tag{2.17}$$

Then, the equation can be expanded as the following expressions:

$$\begin{aligned}
I_t =& \overline{I_0}\sum_{k=0}^{\infty} A_k \cos k\theta + I_1\cos(\theta+\psi_1)\sum_{k=0}^{\infty} A_k \cos k\theta \\
&+ I_2\cos(2\theta+\psi_2)\sum_{k=0}^{\infty} A_k \cos k\theta + I_3\cos(3\theta+\psi_3)\sum_{k=0}^{\infty} A_k \cos k\theta + \dots \\
=& \overline{I_0}(A_0 + A_1\cos\theta + A_2\cos 2\theta + A_3\cos 3\theta + \dots) \\
&+ I_1[A_0\cos(\theta+\psi_1) + A_1\cos\theta\cos(\theta+\psi_1) + A_2\cos 2\theta\cos(\theta+\psi_1) + \dots] \\
&+ I_2[A_0\cos(2\theta+\psi_2) + A_1\cos\theta\cos(2\theta+\psi_2) + A_2\cos 2\theta\cos(2\theta+\psi_2) + \dots] \\
&+ I_3[A_0\cos(3\theta+\psi_3) + A_1\cos\theta\cos(3\theta+\psi_3) + A_2\cos 2\theta\cos(3\theta+\psi_3) + \dots] + \dots.
\end{aligned} \tag{2.18}$$

The expression can be simplified based on the triangular formulas:

$$\begin{aligned}
I_t =& \overline{I_0}A_0 + \overline{I_0}A_1\cos\theta + \overline{I_0}A_2\cos 2\theta + \overline{I_0}A_3\cos 3\theta + \dots \\
&+0.5I_1A_1\cos\psi_1 + 0.5I_1\left\{\begin{array}{l}
[2A_0\cos(\theta+\psi_1) + A_2\cos(\theta-\psi_1)] \\
+[A_1\cos(2\theta+\psi_1) + A_3\cos(2\theta-\psi_1)] \\
+[A_2\cos(3\theta+\psi_1) + A_4\cos(3\theta-\psi_1)] \\
+[A_3\cos(4\theta+\psi_1) + A_5\cos(4\theta-\psi_1)] + \dots
\end{array}\right\} \\
&+0.5I_2A_2\cos\psi_2 + 0.5I_2\left\{\begin{array}{l}
[A_1\cos(\theta+\psi_2) + A_3\cos(\theta-\psi_2)] \\
+[2A_0\cos(2\theta+\psi_2) + A_4\cos(2\theta-\psi_2)] \\
+[A_1\cos(3\theta+\psi_2) + A_5\cos(3\theta-\psi_2)] \\
+[A_2\cos(4\theta+\psi_2) + A_6\cos(4\theta-\psi_2)] + \dots
\end{array}\right\} \\
&+0.5I_3A_3\cos\psi_3 + 0.5I_3\left\{\begin{array}{l}
[A_2\cos(\theta+\psi_3) + A_4\cos(\theta-\psi_3)] \\
+[A_1\cos(2\theta+\psi_3) + A_5\cos(2\theta-\psi_3)] \\
+[2A_0\cos(3\theta+\psi_3) + A_6\cos(3\theta-\psi_3)] \\
+[A_1\cos(4\theta+\psi_3) + A_7\cos(4\theta-\psi_3)] + \dots
\end{array}\right\} + \dots
\end{aligned} \tag{2.19}$$

After that, the expression of Eq. 2.19 is further expanded as the following:

$$\begin{aligned}
I_t =\, & \overline{I_0}A_0 + 0.5I_1A_1\cos\psi_1 + 0.5I_2A_2\cos\psi_2 + 0.5I_3A_3\cos\psi_3 + \ldots \\
& + \{\overline{I_0}A_1 + 0.5[I_1\cos\psi_1(2A_0 + A_2) + I_2\cos\psi_2(A_1 + A_3) + I_3\cos\psi_3(A_2 + A_4) + \ldots]\}\cos\theta \\
& - 0.5[I_1\sin\psi_1(2A_0 - A_2) + I_2\sin\psi_2(A_1 - A_3) + I_3\sin\psi_3(A_2 - A_4) + \ldots]\sin\theta \\
& + \{\overline{I_0}A_2 + 0.5[I_1\cos\psi_1(A_1 + A_3) + I_2\cos\psi_2(2A_0 + A_4) + I_3\cos\psi_3(A_1 + A_5) + \ldots]\}\cos 2\theta \\
& - 0.5[I_1\sin\psi_1(A_1 - A_3) + I_2\sin\psi_2(2A_0 - A_4) + I_3\sin\psi_3(A_1 - A_5) + \ldots]\sin 2\theta \\
& + \{\overline{I_0}A_3 + 0.5[I_1\cos\psi_1(A_2 + A_4) + I_2\cos\psi_2(A_1 + A_5) + I_3\cos\psi_3(2A_0 + A_6) + \ldots]\}\cos 3\theta \\
& - 0.5[I_1\sin\psi_1(A_2 - A_4) + I_2\sin\psi_2(A_1 - A_5) + I_3\sin\psi_3(2A_0 - A_6) + \ldots]\sin 3\theta \\
& + \{\overline{I_0}A_4 + 0.5[I_1\cos\psi_1(A_3 + A_5) + I_2\cos\psi_2(A_2 + A_6) + I_3\cos\psi_3(A_1 + A_7) + \ldots]\}\cos 4\theta \\
& - 0.5[I_1\sin\psi_1(A_3 - A_5) + I_2\sin\psi_2(A_2 - A_6) + I_3\sin\psi_3(A_1 - A_7) + \ldots]\sin 4\theta + \ldots .
\end{aligned} \tag{2.20}$$

To be simplified, the above equation can be abbreviated according to the modulation frequency ($k\theta$):

$$I_t = \sum_{k=0}^{\infty} X_k \cos k\theta - \sum_{k=0}^{\infty} Y_k \sin k\theta, \tag{2.21}$$

where X_k and Y_k are the k-th Fourier components of the light intensity which can be expressed as follows:

$$\begin{cases}
X_0 = \overline{I_0}A_0 + 0.5\sum_{k=1}^{\infty} I_k A_k \cos\psi_k \\
Y_0 = 0 \\
X_k = \overline{I_0}A_k + 0.5\sum_{i=1}^{\infty} I_i \cos\psi_i (2^{\delta_{ki}} A_{|k-i|} + A_{k+i}) \\
Y_k = 0.5\sum_{i=1}^{\infty} I_i \sin\psi_i (2^{\delta_{ki}} A_{|k-i|} - A_{k+i}), k = 1, 2, 3 \ldots,
\end{cases} \tag{2.22}$$

where δ_{ki} is the Kronecker delta, the value is 1 if $k = i$ and 0 otherwise.

2.2.2 Lock-in amplifier

Using a lock-in amplifier (LIA), the k-th Fourier components of the light intensity can be fixed and picked out by the same frequency reference signals as:

$$\begin{cases}
X_k^{\mathrm{LIA}} = [X_k \cos k\theta - Y_k \sin k\theta] \cos(k\omega t + \beta_k^{\mathrm{X}}) \\
Y_k^{\mathrm{LIA}} = [X_k \cos k\theta - Y_k \sin k\theta] \sin(k\omega t + \beta_k^{\mathrm{Y}}),
\end{cases} \tag{2.23}$$

where β_k^{X} and β_k^{Y} are the phases of the reference signals at the X and Y axes, respectively. From Eq. 2.23, we can see that the amplitude of the harmonic in each axis is decided by β_k^{X} and β_k^{Y}. For example on the X axis, the signal multiplied by the reference signal is expressed as:

$$\begin{aligned}X_k^{\mathrm{LIA}} &= [X_k\cos(k\omega t + k\eta) - Y_k\sin(k\omega t + k\eta)]\cos(k\omega t + \beta_k^{\mathrm{X}})\\ &= \frac{1}{2}X_k\cos(k\eta - \beta_k^{\mathrm{X}}) - \frac{1}{2}Y_k\sin(k\eta - \beta_k^{\mathrm{X}})\\ &+ \frac{1}{2}X_k\cos(2k\omega t + k\eta + \beta_k^{\mathrm{X}}) - \frac{1}{2}Y_k\sin(2k\omega t + k\eta + \beta_k^{\mathrm{X}}).\end{aligned} \tag{2.24}$$

On the Y axis, the signal would be:

$$\begin{aligned}Y_k^{\mathrm{LIA}} &= [X_k\cos(k\omega t + k\eta) - Y_k\sin(k\omega t + k\eta)]\sin(k\omega t + \beta_k^{\mathrm{Y}})\\ &= -\frac{1}{2}X_k\sin(k\eta - \beta_k^{\mathrm{Y}}) - \frac{1}{2}Y_k\cos(k\eta - \beta_k^{\mathrm{Y}})\\ &+ \frac{1}{2}X_k\cos(2k\omega t + k\eta + \beta_k^{\mathrm{Y}}) + \frac{1}{2}Y_k\sin(2k\omega t + k\eta + \beta_k^{\mathrm{Y}}).\end{aligned} \tag{2.25}$$

There are two kinds of signals in Eqs. 2.24 and 2.25: the DC signal without the modulation angular frequency (ω) and the signal with the modulation angular frequency. When the signals are sent to the low-pass filter, only the DC signals remained, the amplitudes of the harmonic in each axis are written:

$$\begin{cases} X_k^{\mathrm{LIA}} = \frac{1}{2}X_k\cos(k\eta - \beta_k^{\mathrm{X}}) - \frac{1}{2}Y_k\sin(k\eta - \beta_k^{\mathrm{X}})\\ Y_k^{\mathrm{LIA}} = -\frac{1}{2}X_k\sin(k\eta - \beta_k^{\mathrm{Y}}) - \frac{1}{2}Y_k\cos(k\eta - \beta_k^{\mathrm{Y}}).\end{cases} \tag{2.26}$$

In normal, the phases of the reference signal are set the same: $\beta_k^{\mathrm{X}} = \beta_k^{\mathrm{Y}}$ in the lock-in amplifier. However, because of the arbitrary variation in the phase shift in wavelength (η), the k-th Fourier components of the light intensity (X_k and Y_k) are configured randomly into the X and Y axes. In order to capture the entire harmonic signal, the scalars of the Fourier components are used as the complete harmonic signal when the high-order sinusoidal modulation intensities (I_k) are neglected:

$$\sqrt{(X_k^{\mathrm{LIA}})^2 + (Y_k^{\mathrm{LIA}})^2} = \frac{1}{2}\sqrt{(X_k)^2 + (Y_k)^2} = 0.5\overline{I_0}A_k. \tag{2.27}$$

Nevertheless, Eq. 2.27 will be invalid in the applications if the sinusoidal modulation intensities (I_k) are strong and cannot be ignored, especially in the first harmonic (Section 2.2.5). According to Eqs. 2.24 and 2.25, when setting the phases of the reference signal as:

$$\beta_k^{\mathrm{X}} = \beta_k^{\mathrm{Y}} = k\eta, \tag{2.28}$$

the k-th Fourier components (Eq. 2.26) would assigned on their own axes:

$$\begin{cases} X_k^{\mathrm{LIA}} = \frac{1}{2}X_k\\ Y_k^{\mathrm{LIA}} = -\frac{1}{2}Y_k.\end{cases} \tag{2.29}$$

As can be seen, Eqs. 2.28 and 2.29 would be a good solution if the η can be inferred. Notwithstanding, the η is an arbitrary value in each measurement. So people always manually readjust the reference signal phase to assign the harmonic signal into one axis. The operation is time-consuming and not so convenient in the long-term measurements. Therefore, to overcome this problem, we intend to build up a system which is more automatic in the phase shift determination and gas concentration measurement.

2.2.3 Under low or no absorbance

The aforementioned Eq. 2.16 has discussed about the k-th order Fourier component of the transmittance (A_k) when absence of the gas absorption. It concluded that the energy only stays at the zeroth Fourier component with A_0 =1 while the other components are 0. Thus, under the absorption-free conditions, Eq. 2.22 can be expressed as:

$$\begin{cases} X_0^{\mathrm{BG}} = \overline{I_0} \\ Y_0^{\mathrm{BG}} = 0 \\ X_k^{\mathrm{BG}} = I_k \cos \psi_k \\ Y_k^{\mathrm{BG}} = I_k \sin \psi_k, k = 1, 2, 3 \ldots. \end{cases} \tag{2.30}$$

Eq. 2.30 is caused by the nonlinear intensity modulation of the laser and it is defined as the Residual Amplitude Modulation (RAM) in WMS. Therefore, the k-th order sinusoidal modulation intensity (I_k) can be inferred from the RAM when there is no gas absorption. The RAM will be further discussed in Section 2.2.6.

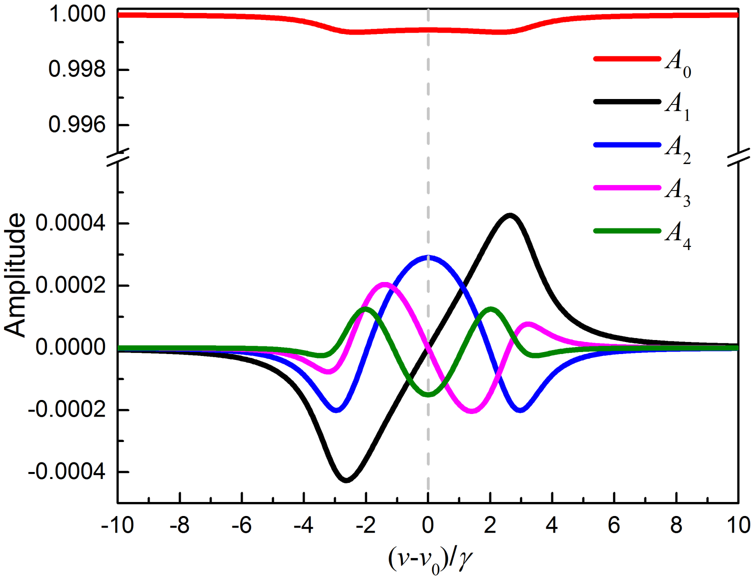

Figure 2.5: Simulations of the k-th order Fourier component of the transmittance (A_k) at the weak absorbance conditions (absorbance approximates 2‰) with modulation index of 3.0.

Furthermore, the simulations of A_k under weak absorbance conditions when $\alpha(v_0) \ll 10\%$ are illustrated in Figure 2.5. The simulations are based on the CO_2 absorption line at 2003.5 nm, the gas conditions are at the atmospheric pressure and temperature with light path length of 30 cm and gas concentration of 400 ppm. The modulation index is set 3.0. Under these gas parameters, the peak absorbance ($\alpha(v_0)$) is around 2‰.

The curves of the A_k indicate that the A_0 signal is much stronger than the other components. The A_0 approximately equals to 1 ($A_0 \approx 1$) while the other components are $A_1, A_2, A_3, A_4, \cdots \ll A_0$. In this case, $A_1, A_2, A_3, A_4, \cdots$ can approximate to 0 when compared with A_0. And then, the first, second and higher order Fourier components of the light intensity (X_k and Y_k, $k = 1, 2, 3 \cdots$) in Eq. 2.22 can be simplified as:

$$\begin{cases} X_k = \overline{I_0} A_k + I_k \cos \psi_k \\ Y_k = I_k \sin \psi_k, k = 1, 2, 3 \dots \end{cases} \tag{2.31}$$

The zeroth order Fourier component (X_0, Y_0) will described in Section 2.2.5. Comparing Eq. 2.30 with Eq. 2.22 and 2.23, the X_k and Y_k of the absorption signal contain the items of the RAM signal. So the RAM is also defined as the background signal when presence of gas absorption.

Moreover, combined the expressions in Eq. 2.29 and 2.31, the RAM signal can be separated into the two axes only when the reference signal phases in lock-in amplifier are set as shown in Eq. 2.28. The discussions in the following sections are all under this precondition.

2.2.4 Modulation intensities

Since the laser light intensity is nonlinear modulation (Eq. 2.14), the high-order sinusoidal modulation intensities (I_k) will become larger when the modulation depth (modulation index) increases. In the actual applications, the modulation index (m) is always set around 2.2 since the second harmonic signal reaches to its maximum. The absorption signal is assigned at the low harmonics such as the first and second harmonics, high-order harmonics are weak. However, when the modulation index increases, the high-order I_k becomes stronger, not only the high-order harmonics will be enhanced, but also the low-order harmonic will be deformed by the high-order I_k (RAM), as shown in Eq. 2.22. In that case, the high-order I_k should be taken into account in the actual measurement.

To study the modulation intensities, the recorded signal without gas absorption is utilized for FFT (Fast Fourier transform) analysis. The modulation sine signal is 6.0 kHz of frequency and 60 mV of amplitude, which is similar to all experiments in the study. And there is no ramp signal to scan across the absorption lines. The FFT result is shown in Figure 2.6, where all the intensities at their own frequency are normalized by the intensity at 0 (also named the central light intensity ($\overline{I_0}$)). As can be seen in the graph, except the zeroth intensity ($\overline{I_0}$), the first order light intensity (I_1, in an order of 10^{-2}), is about 100 times larger than the other intensities (in the order of 10^{-4} or even smaller). Therefore, the higher-order intensities can be neglected in the applications

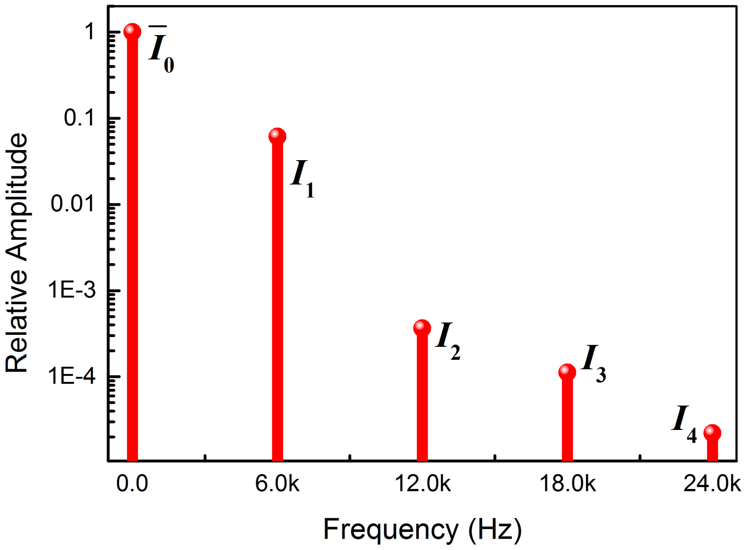

Figure 2.6: FFT analysis of the laser light intensity when there is no gas absorption and the ramp signal is not added in the modulation.

and the neglection would not introduce big measurement bias under this modulation depth (60 mV modulation amplitude).

According to the above discussions, when only the zeroth and the first order sinusoidal modulation intensities ($\overline{I_0}$ and I_1) are taken into account, Eq. 2.22 is further simplified as below, and Eq. 2.32 is used to express the harmonic signals in the study.

$$\begin{cases} X_0 = \overline{I_0} \\ Y_0 = 0 \\ X_1 = \overline{I_0} A_1 + I_1 \cos \psi_1 \\ Y_1 = I_1 \sin \psi_1 \\ X_k = \overline{I_0} A_k \\ Y_k = 0, k = 2, 3, 4 \ldots . \end{cases} \tag{2.32}$$

2.2.5 The zeroth harmonic

As displayed in Eq. 2.32, all the harmonics produced via the LIA contain the component of the central light intensity ($\overline{I_0}$). The harmonics are amplified by the central light intensity so that the harmonic signals are deformed and should be calibrated before the gas measurement. As mentioned above, the central light intensity is determined by the ramp signal which is a nonlinear modulation especially in the broad tuning. It is a signal which should be acquired from the absorption-free conditions. Moreover, in TDLAS-WMS, the laser light is tuned by the ramp and sinusoidal signals simultaneously, the central light intensity is submerged in the sine waveform. People usually take the first harmonic at the line center or the entire harmonic as the signal to calibrate the other harmonics, which is the well-known "calibration-free $nf/1f$" method. However, as shown in Eq. 2.32, the first harmonic contains the RAM signal; the "calibration-free $nf/1f$" method will then introduce the RAM signal in measurement. The RAM will be discussed in the following section. Moreover, the RAM should also be calibrated carefully prior to the measurement (without gas absorption) or from a separate absorption-free laser beam. The operations are inconvenient and complex. It would even induce measurement error when the light path drifts. We would like to find an approach to real-time determine the central light intensity ($\overline{I_0}$) so that the measurement can get rid of the calibration process and overcome the problem of light intensity fluctuations. In this way, the measurement system can be applied even in the vibration situations where the laser path is difficult to fix.

When the absorption is weak ($\ll 10\%$), the zeroth Fourier components of the light intensity (X_0 and Y_0) in Eq. 2.32 can be used to derive zeroth harmonic as:

$$S_{0f} = \sqrt{X_0^2 + Y_0^2} = X_0 \approx \overline{I_0} \tag{2.33}$$

That is to say, the central light intensity ($\overline{I_0}$) can be replaced by the zeroth harmonic (S_{0f}) in the optically thin samples (absorbance $\ll 10\%$). Thus, in TDLAS-WMS, the zeroth harmonic can be utilized to normalize the other harmonics.

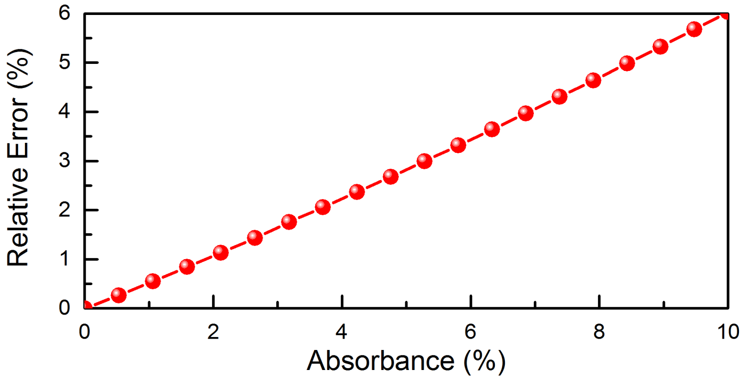

Figure 2.7: The error analysis of concentration measurement when the S_{0f} is served as $S_{0f} \approx \overline{I_0}$ to normalize the harmonics.

Figure 2.7 shows the gas concentration measurement (Sections 2.2.6 and 2.2.7) error analysis when the zeroth harmonic is treated as the central light intensity ($S_{0f} \approx \overline{I_0}$) to normalize the other harmonics. The simulation is carried out at low absorbance when the absorbance is less than 10%. From the plot, we can learn that the relative errors increase as the increment of the absorbance. For example, when the absorbance is 5%, the measurement error is less than 3%. However, when the absorbance is doubled, the error is about 6%. In order to ensure the measurement error within 1%, the absorbance should not exceed 2%. Therefore, for the trace gas measurement when the absorbance is extremely weak (absorbance $\ll 10\%$), the approximation of $S_{0f} \approx \overline{I_0}$ will not introduce a large measurement error. In the study, we intend to measure the CO_2 concentration in the urban areas using the laser wavelength at 2.0 μm with short path length (30 cm). According to the simulation in Figure 2.5, the absorbance is about 2‰ in most cases. Thus, the algorithm is satisfied in the measurements [86].

2.2.6 RAM in the first harmonic

In TDLAS-WMS, there is always an additional background signal in the harmonic signals due to the nonlinear intensity modulation of the real laser diodes, which is the so-called RAM signal. When there is an absence of gas absorption, the RAM appears as a signal at the modulation frequency. According to the discussion of the k-th order Fourier component of the transmittance (A_k) and the expression of Eq. 2.22, the RAM exits together with the item of A_0. Therefore, under weak absorbance, when the high-order Fourier components of the transmittance (A_k) are equal to 0 and $A_0 \approx 1$, the X and Y components of the first harmonic (X_{1f} and Y_{1f}) in Eq. 2.31 and Eq. 2.32 are simplified as follows:

$$\begin{cases} X_{1f} = A_1 + \frac{I_1}{I_0} \cos \psi_1 \\ Y_{1f} = \frac{I_1}{I_0} \sin \psi_1. \end{cases} \tag{2.34}$$

Eq. 2.34 has been normalized by the zeroth harmonic (S_{0f}), where the zeroth harmonic is approximate to $\overline{I_0}$ at the weak absorbance.

According to Eq. 2.34, the X_{1f} consists of two parts: the harmonic signal which is a concentration-dependent item and the cosine phase shift of the RAM signal; while the Y_{1f} is just the sine phase shift of the RAM signal which is concentration-independent. Therefore, the Y_{1f} can be used to measure the phase shift (ψ_1) between the wavelength modulation and the first order light intensity modulation when I_0, I_1 are given:

$$\psi_1 = \arcsin (Y_{1f} \frac{\overline{I_0}}{I_1}). \tag{2.35}$$

Then, the measured phase shift is employed to eliminate the RAM signal when it is substituted into the X_{1f} expression:

$$\begin{aligned} \overline{X_{1f}} &= X_{1f} - \frac{Y_{1f}}{\tan \psi_1} \\ &= A_1 = PS(T)LCH_1, \end{aligned} \tag{2.36}$$

where H_k is the k-th order Fourier component of the spectral line shape. The expressions of H_k are shown as:

$$\begin{cases} H_0 &= \frac{1}{2\pi} \int_{-\pi}^{\pi} \varphi(\overline{v} + a \cos \theta) \mathrm{d}\theta \\ H_k &= \frac{1}{\pi} \int_{-\pi}^{\pi} \varphi(\overline{v} + a \cos \theta) \cdot \cos k\theta \cdot \mathrm{d}\theta, k = 1, 2, 3 \cdots . \end{cases} \tag{2.37}$$

At the line center, H_k is approximately 0 when k is odd and equals to its maximum when k is even. And $A_k = PS(T)LCH_k$. Thus, the gas concentration can be inferred from ($\overline{X_{1f}}$):

$$C = \frac{\overline{X_{1f}}}{PS(T)LH_1}. \tag{2.38}$$

According to Eq. 2.38, the gas concentration can be inferred without the extra calibration against the standard reference gas. Thus, it is a self-calibrated method getting rid of the calibration process. Moreover, the phase shifts (ψ_k) between the wavelength modulation and the 2^{nd}, 3^{rd},$\cdots$ order laser light intensity modulations can be measured based on their corresponding Y_{kf}. As shown in Figure 2.6 and Eq. 2.32, the higher order light intensity ($I_2 \cdots I_k$) is much smaller than the first one, more than 100 times less than I_1. Therefore, in practical measurements, the 2^{nd} order RAM is treated as a linear offset while the higher orders are always neglected.

2.2.7 Multi-harmonic

Based on the above formula derivations, under weak absorbance condition, the harmonic signals (the first harmonic should prior to subtract the RAM signal) can be expressed as follows:

$$\begin{aligned} \overline{S_{kf}} &= \frac{S_{kf}}{S_{0f}} \approx \frac{S_{kf}}{\overline{I_0}} \\ &\approx PS(T)LCH_k, k = 1, 2, 3, \cdots, \end{aligned} \tag{2.39}$$

where $\overline{S_{kf}}$ is the k-th harmonic normalized by the zeroth harmonic. The profiles of the harmonic signals are linearly proportional to the gas concentration at a given gas pressure and temperature, thus, gas concentration can be determined directly as follows:

$$C = \frac{\overline{S_{kf}}}{PS(T)LH_k}, k = 1, 2, 3, \cdots. \tag{2.40}$$

In the measurement system, we can develop a lock-in amplifier which produces all harmonics simultaneously, and then, the zeroth harmonic is applied to eliminate the central light intensity in other harmonics. The normalized harmonics are obtained, and the gas concentration can subsequently be inferred according to Eq. 2.40. There is no additional reference installation throughout the entire process. Moreover, the Linear Least Squares Curve Fitting (LLSCF) algorithm can be utilized to infer the gas concentrations as follows [75, 90, 91]:

$$\hat{C} = \frac{1}{PS(T)L}(\Psi^T\Psi)^{-1}\Psi^T Y \tag{2.41}$$

where Ψ is the observation matrix including multiple Fourier components for different gas species, the offset and the normalized RAM; Y is a vector for the selected multiple harmonic signals; and $\hat{C} = (c_1, c_2, \cdots, l_O, l_R)^T$ is the optimum solved vector which contains the concentrations of different gas species, the levels of the offset and the RAM. Eq. 2.41 is a closed, convergent and fast computing expression from which the gas concentrations of different multi-harmonic combinations can be calculated. The LabVIEW data processing of the LIA and LLSCF algorithm for real-time CO_2 and H_2O concentrations measurement will be further introduced in the next chapter.

2.2.8 Modulation index

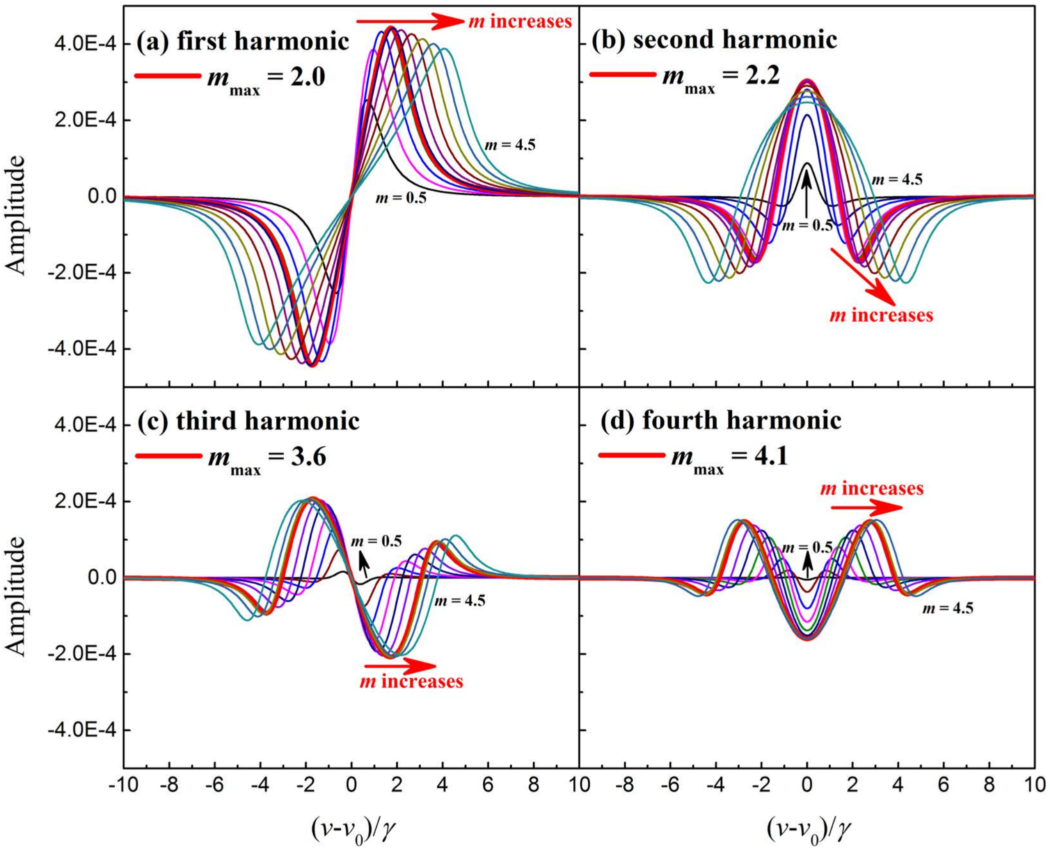

Figure 2.8: The first, second, third and fourth harmonic curves vary with modulation index (m), where the m is ranging from 0.5 to 4.5.

In the thesis, the multi-harmonics (from the zeroth to fifth harmonics) are studied for the gas concentration measurements. Due to the nonlinear modulation of the laser, the modulation depth (a) among the long scanning range is varying, as well as the modulation index (m). The different harmonics are produced at the wide modulation index ranges. Moreover, as shown in Figure 2.8, the harmonic amplitude decreases as the order increases, the first harmonic has the highest amplitude and largest SNR among all the other harmonics. On the other hand, the harmonic amplitude varies with the modulation index. The optimal modulation indices of each harmonic are different.

To ensure all harmonics have the optimal SNRs in the detection, the first to fourth harmonic signals are simulated at different modulation indices ranging from 0.5 to 4.5. The results are shown in Figure 2.8, where the simulation gas properties (P, T, L, C and v_0,) are the same as that in Figure 2.5. The maximum amplitudes are plotted as the red-thick lines in each harmonics with their own optimal modulation index ($m_{\max}$). The $m_{\max}$ is the modulation index when the harmonic reaches to its maximum amplitude. As displayed in the graph, the first and second harmonics have their max signals at $m = 2.0$ and $m = 2.2$ respectively, while the $m_{\max}$ of the third and fourth harmonic increase to 3.6 and 4.1, respectively. The harmonics become weak when increased the orders of the harmonics. Therefore, to make the high-order harmonics, e.g. the third, fourth and fifth harmonics be better SNRs, the modulation depth should be set at higher value, around 3.0 to 4.0. However, as can be seen in the plots, the signal widths become wider as the m increases, that is, the signal energies spread from the absorption center to its adjacent. The harmonic signals are over-modulated and may result in overlapping with their adjacent absorption lines when using the high modulation indices.

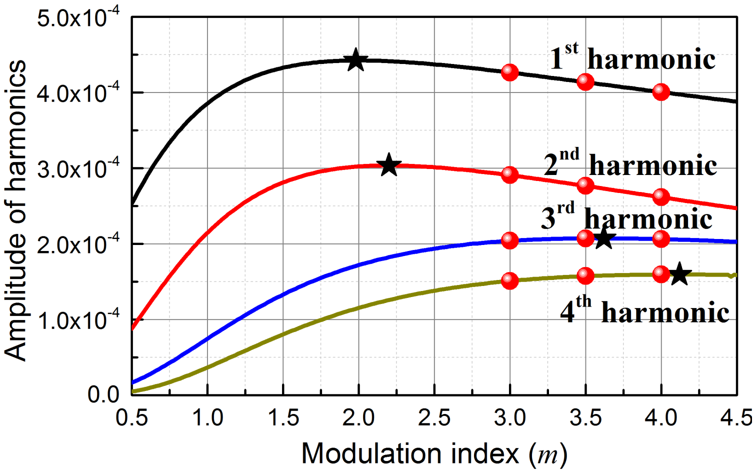

Figure 2.9: The amplitudes of the first, second, third and fourth harmonics vary with modulation index (m) ranging from 0.5 to 4.5. The black stars denote the maximum at each harmonics and the red dots are the harmonic amplitudes at m=3.0, 3.5 and 4.0.

The amplitudes of the first to fourth harmonics vary with the modulation index (m) are simulated and illustrated in Figure 2.9 and Table 2.1, where the gas parameters are the same as Figure 2.8. The relative amplitudes of the four harmonics become clear in Figure 2.9. As indicated in the figure and table, when m=2.0 or 2.2, the first and second harmonics would reach to their maximum values. After that, their amplitudes are slightly decrease as the increasing of m. On the other side, we can see that the amplitude of the third harmonic only takes 88% of its maximum when m= 2.2. The value for the fourth harmonic is even less, with 79%. When m increases to 3.0, the percentages of the

Table 2.1: Overview of the harmonics at different modulation indices, the percentage data are the harmonics amplitudes compared with their own maximum ($m_{\max}$).

Items	S_{1f}	S_{2f}	S_{3f}	S_{4f}
$m_{\max}$	2.0	2.2	3.6	4.1
m=2.2, percent of maximum	99.8%	100%	88.0%	78.9%
m=3.0, percent of maximum	96.4%	95.8%	98.4%	94.7%
m=3.5, percent of maximum	93.5%	91.1%	99.96%	98.6%
m=4.0, percent of maximum	90.5%	86.2%	99.5%	99.96%

third and fourth harmonics will raise to 98.4% and 94.7%, respectively, while the amplitudes of the first and second harmonics take still more than 95% of their maximums. If we set m at 4.0, the third and fourth harmonics will almost arrive their maximum levels, however, the amplitude remains in the second harmonic will reduce to 86.2%. As the percentages listed in Table 2.1, when setting m at 3.0 to 3.5, the amplitudes of all of the harmonics exceed 90%. Therefore, the optimal modulation indices can be set at 3.0 to 3.5, so that the SNR of the harmonics, especially the third and fourth harmonics, can be ensured.

2.3 Conclusion

This chapter mainly introduces the theory of the TDLAS (Tunable Diode Laser Absorption Spectroscopy) and WMS (Wavelength Modulation Spectroscopy). It is the theoretical foundations of the measurement system.

At first, the basic theory of TDLAS, Beer-Lambert Law, is presented. The line strength and the line profiles of the absorption line are demonstrated. The direct TDLAS method is a common way to calculate the absolute gas concentration without calibration. However, this method is easily affected by various noises and cannot be employed for trace gas measurement when the absorbance is thin.

Then, the WMS technique is presented with all modulation intensities. The harmonic formulas are derived and the residual amplitude modulation (RAM) is discussed at the absence of gas absorption. And the harmonic signals are further derived for gas concentration measurement based on several approximations. Among the procedure, some important issues are discussed as bellows:

1) **Lock-in amplifier**: The working principles in the lock-in amplifier as well as the relationship between the phases are presented in detail. The lock-in amplifier plays a vital role for the measurement system, not only it can produce the multiple harmonics synchronously, but also the reference signal phase is employed to assign the harmonic and RAM signals separately into two axes. Under the

presuppositions, the first harmonic can eliminate the RAM signal and then be used to detect the gas concentration.

2) **The orders of the modulation intensities**: owing to the nonlinear modulation of the laser, the laser light without gas absorption is used to study the laser properties and the background signal of the harmonics. It concludes that the first order light intensity is much stronger than the higher-order intensities. Hence, only the background signal (RAM) in the first harmonic should be considered in the measurement.

3) **The zeroth harmonic**: calibration process is always a big problem in gas sensing. Simulations have revealed that the zeroth order Fourier component of the transmittance is much stronger that the other orders under thin absorbance, so that we derive that the zeroth harmonic approximates to the central light intensity. Based on the derivations, the laser light intensity in the harmonics can be normalized by the zeroth harmonic. In this way, the measurement can get rid of the calibration process. The error analysis of the approximation is also conducted to quantify the uncertainties in the applications.

4) **Modulation index**: To find a suitable modulation index for the multiple harmonics, the first to fourth harmonics at the different modulation indices are simulated. Since the third and fourth harmonic amplitudes are smaller than the first and second harmonics, it is better to set the modulation index at the value when the third and fourth harmonics at its largest amplitudes. For this reason, it optimal modulation index range is about 3.0 to 3.5.

5) **RAM in the first harmonic**: the procedure of eliminating the RAM effect in the first harmonic is illustrated. And the obtained concentration-dependent signal is utilized for gas sensing.

6) **Multi-harmonic detection**: The formulas of multi-harmonics are discussed, and they are used for gas concentration measurement based on the LLSCF algorithm.

This chapter has presented the principle of the TDLAS-WMS. Moreover, the possible approximations, such as the low absorbance, the zeroth harmonic, and the modulation intensities, in the real measurements have been discussed. The corresponding errors analyses have also been presented. The discussions in this chapter will be useful in the experiment designs and the gas concentration measurements in the following chapters.

3 Experimental Foundation

This chapter will introduce the design of the TDLAS-WMS measurement system according to the formula derivations in the previous chapter, including the hardware and software designs. The purpose in the chapter is to build up a TDLAS-WMS compact measurement system with high precision, high SNR, high accuracy, and easy operation for measurement. The structure of the laser light path and the information of the experimental components will be presented in the first two sections. The absorbance of the absorption lines near 2.0 μm and 2.36 μm is simulated and the results are used for the line selection.

In TDLAS-WMS, the harmonic signals are produced from lock-in amplifier (LIA). Among all the harmonics, the first harmonic has the largest amplitude and highest SNR. Therefore, theoretically it can obtain the highest precision when it is employed in the gas detection. However, since the RAM effect in the first harmonic is so strong that the concentration-dependent harmonic is submerged by the RAM and cannot be utilized in gas concentration measurement. This chapter will establish a signal processing in LabVIEW software and aim to settle the following objectives based on the theory of TDLAS-WMS presented in the last chapter (The contents have been published in Lan et al. 2019 [86, 90]):

- ◇ Use an instrument (DAQ) to supply the modulation signals and record the absorption signal synchronously.
- ◇ Build up a digital LIA to produce multiple harmonics. In the LIA, the central laser light intensity can be captured to normalize the other harmonic signals.
- ◇ Enable the LIA to assign the concentration-dependent harmonics on one axis but not spread in two axes.
- ◇ Infer the RAM in the first harmonic and then eliminate the RAM signal; and finally obtain the concentration-dependent first harmonic.
- ◇ Determine the wavelength and modulation depth in the wide tuning range, and calculate the other intermediate properties for gas concentration measurement.
- ◇ Calculate the gas concentrations according to the first harmonic detection and multi-harmonic detection.

3.1 Experimental Setup

A schematic diagram of the TDLAS-WMS light path is shown in Figure 3.1. The measurement system consists of an infrared light source (VCSEL, Vertical-Cavity Surface-Emitting Laser, Vertilas [92]), an InGaAs amplified photodetector (PD, PDA10DT-EC, Thorlabs) and a concave mirror (CM254-075-G01, Thorlabs).

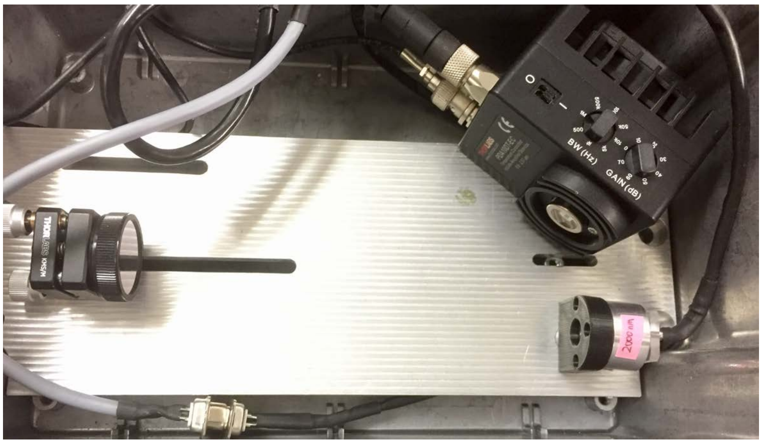

Figure 3.1: Schematic diagram of the light path, including the VCSEL laser housing with heating sink and holder, photodetector (PD) and reflective concave mirror.

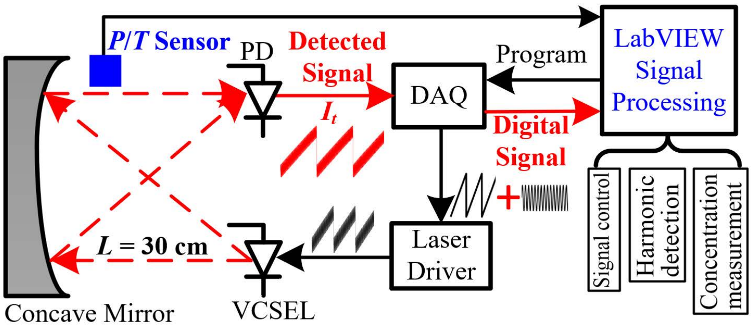

Figure 3.2: The flow diagram of TDLAS-WMS measurement system.

The block flow diagram of the TDLAS-WMS measurement system is displayed in Figure 3.2. In the measurement, the VCSEL is served as the light source. The infrared light emitting from the VCSEL is controlled by a laser driver (Arroyo Instruments 6301). Then, the light travels through the measured gas medium and reflected back by the reflective concave mirror. The focus length of the concave mirror is 75 mm. When the object distance and image distance are the same, the total path length is 30 cm according to the Gaussian mirror equation. Then, the absorbed light signal goes into and is detected by the PD. Subsequently, the detected signal is recorded and digitized via a high-speed memory data acquisition card (DAQ, NI USB-6361). The digitized data is sent into the signal processing to further calculate gas concentration. In this procedure, the DAQ is deployed not only as an oscilloscope to record and digitize the detected signal but also as a signal generator to provide the ramp and sinusoidal signals such that the laser wavelength is tuned and modulated. The driving current, the laser and absorption signals are also marked along the signal process in the flow diagram.

The layout of the measurement system can be divided into two parts: the hardware part as displayed in the left panel of Figure 3.2; and the software part as shown in the right panel of Figure 3.2. The hardware diagram includes the VCSEL, concave mirror, PD, laser driver and DAQ, while the software part is the signal processing which is conducted in the computer. As illustrated in Figure 3.2, the software development contains the signal control, the harmonic detection and the concentration measurement. The components and signal processing about the experimental system will be discussed in the following sections.

3.2 Experimental Components

3.2.1 VCSEL

VCSEL is the vertical-cavity surface-emitting laser, which the laser light emits perpendicularly from the top surface of the chip. The sample pictures of two types of InP-based VCSELs are shown in Figure 3.3, the laser with emitting wavelength center of 2004 nm is used for CO_2 and H_2O monitoring (left in Figure 3.3), and the laser with 2365 nm emitting center is utilized for CH_4 and CO detections (right in Figure 3.3). The 2004 nm laser will be operated for CO_2 and H_2O gas concentration measurements in the study.

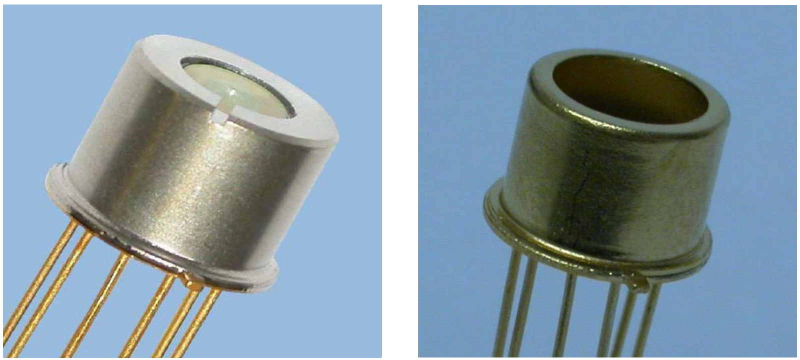
(a) 2004 nm (b) 2365 nm

Figure 3.3: Sample pictures of VCSEL (left: 2004 nm; right: 2365 nm).

Unlike the common tunable laser, for example, DFB (distributed feedback) laser, the VCSEL has several advantages in gas monitoring. Since it doesn't have to cleave the individual chip out of a wafer and has high reflectivity mirror (DBR: distributed Bragg reflector, reflectivity more than 99%) inside the laser chip, VCSEL has unique features

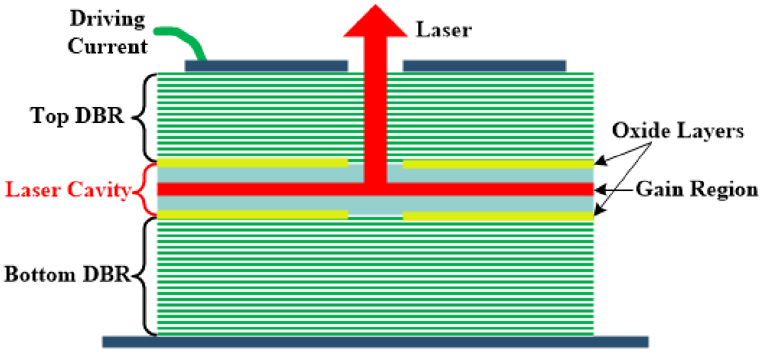

Figure 3.4: VCSEL emits the light perpendicularly from the surface [93].

of low threshold and operating currents. Therefore it has low power consumption and low power output. The structure of VCSEL is exhibited in Figure 3.4, the top DBR and bottom DBR form an Fabry-Perot Resonator (F-P Resonator) that the free spectral range (FSR) is determined by:

$$\delta v = \frac{c}{2d} \tag{3.1}$$

where c is the light speed and d is the thickness between the two DBRs. For VCSEL, the d is much smaller (only a few micrometers) than the other types of laser, so that the FSR of VCSEL is larger than the other type of laser. Thus, a wider wavelength range is allowed to go through the F-P resonator. Moreover, the resistance inside the cavity of VCSEL is much larger than the other types of laser, when the VCSEL is tuned by current, the heat inside the cavity increases more, and leading to a wider wavelength emission in the cavity. The optical and electrical reasons result in the VCSEL being characterized by the speed and wide wavelength tuning range. Therefore, the wavelength emits from the VCSEL is able to cover multiple gas absorption lines. VCSEL can thus be employed for simultaneously detecting several gas species. What's more, surface-vertical emission gives VCSEL easily alignment and packaging in applications.

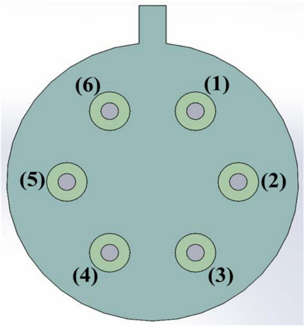

Figure 3.5: Bottom view of VCSEL

Pin	Function
(1)	TEC+
(2)	LD Cathode
(3)	LD Anode
(4)	Thermistor
(5)	Thermistor
(6)	TEC-

Table 3.1: Pin assignment of VCSEL (bottom view)

The bottom view of the laser is shown in Figure 3.5, where there are six pins at the tail of the laser. The assignments of the pins are shown in Table 3.1. The thermistors pins (pins 4 and 5) are used to measure the laser chip temperature. The TEC (thermoelectric cooler) pins (pins 1 and 6) are utilized to control the chip temperature inside the laser diode. When the laser temperature is controlled, the emitting wavelength is driven by the driving current which is loaded via the LD (laser diode) pins (pins 2 and 3).

Table 3.2: Laser driver parameters calibrated by the Vertilas Company near 2.0 μm.

20°C	1.58 mA	4.76 mA	7.94 mA	11.12 mA	14.30 mA
Wavelength (nm)	2001.79	2002.73	2003.94	2005.47	2007.26
40°C	1.87 mA	4.59 mA	7.31 mA	10.03 mA	12.75 mA
Wavelength (nm)	2004.70	2005.49	2006.54	2007.82	2009.33

Table 3.2 indicates the driving parameters of the laser at different wavelength with controlling temperatures of 20°C and 40°C, respectively, in which the data are provided by the Vertilas Company [92]. At the same controlling temperature, the emitting wavelength increases as the tuning current increases.

3.2.2 Photodetector (PD)

Figure 3.6: Photodetector (PD, PDA10DT-EC, Thorlabs)

As shown in Figure 3.6, the photodetector from Thorlabs Company (PD, PDA10DT-EC) applied in the study is an amplified, thermoelectrically cooled, switchable-gain, switchable-bandwidth, and InGaAs photoconductive detector. The InGaAs sensitive wavelength range is from 0.9 μm to 2.570 μm. The thermoelectric cooler (TEC) in conjunction with a fan outside the PD is a cooling system, which are working to maintain the temperature of the photosensitive material, InGaAs, at a constant of -10 °C. In this way, the PD can work normally and ensure the lowest output offsets and noises. Above the PD, the four-pin connector is connected to the power supply to control the chip temperature in inside the PD; the PNC connector is the output of the PD. The tapped holes located at the bottom and sides of the PD are used to hold the PD on the optical board. There are two switches on the side of the PD, which are the bandwidth and the gain adjustments. In the TDLAS-WMS system, to ensure the high resolution and low noise level of the detection, the bandwidth and the gain of the detector are set 1 MHz and 30 dB, respectively.

3.2.3 Laser driver

The VCSEL laser used in the system has a low driving current within a range of 1.5 to 12.5 mA. Thus, the laser diode controller, Arroyo Instruments 6301, with 50 mA of the driving range, is deployed to drive the laser input current in the measurement system. The front interface of laser driver is displayed in Figure 3.7. There are the "Laser Enable" and "Power" switches on the left panel. In the second panel, the "Menu" is to set the limitations of the laser controller, including the controlling temperature and current ranges, the internal resistance, the PID tune and so on; the "Select" button is to select the Laser or the TEC controlling modules; the "Laser" and "TEC" buttons are used to turn on/off the laser and TEC controlling. There are a digital screen, Range, a knob, a BNC connector and buttons for the "Function Keys" on the third panel. The Range is set at the 50mA for our experiment and the knob is used to change the controlling parameters. The functions of the laser diode controller contain the laser driver and the temperature controller.

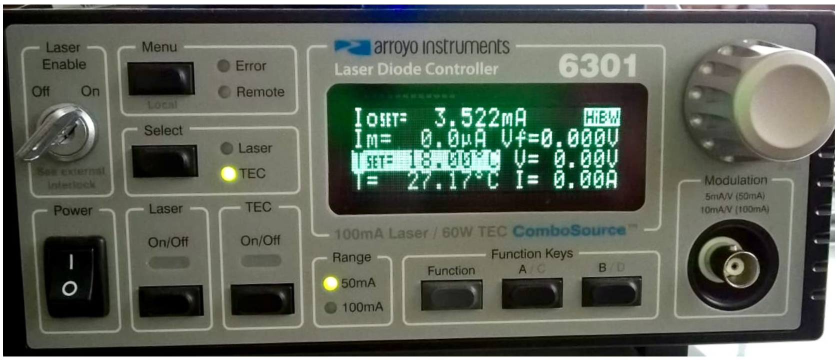

Figure 3.7: Front interface of laser driver (Arroyo Instruments 6301)

For the laser driver, the internal modulation is a constant current with a resolution of 0.002 mA. And the laser temperature is controlled with a resolution of 0.01 °C. An external positive analog voltage modulation can be connected via the BNC connector at the right-bottom corner. When setting the driving range to 50 mA, the voltage to current index of the laser driver is 5 mA/V. A PID loop is set in charge of the laser chip temperature. For the temperature controller, an auto tune can be utilized for the automatic PID parameter calculation. The setting and reading parameters of the laser are simultaneously displayed on the main screen of the interface.

3.2.4 DAQ

The DAQ is a high-speed memory data acquisition card from National Instrument (NI, USB-6361). As shown in Figure 3.8, there are 8 analog inputs and 2 analog outputs with ADC (Analog-to-Digital Converter) resolutions of 16 bits. The maximum sampling rate is 2MS/s with single channel. In this study, only one analog input and one analog output are employed as signal recording and signal generating, respectively. The DAQ is programed by the computer software, called LabVIEW. The NI-DAQmx VIs (Virtual Instruments) supported by the NI Company is installed in the LabVIEW software to connect DAQ to computer and to drive the DAQ.

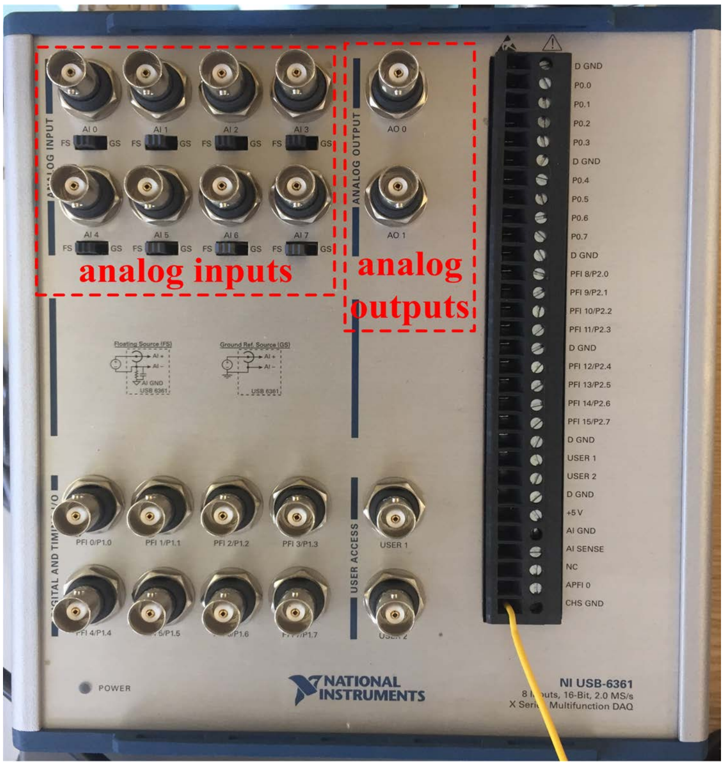

Figure 3.8: DAQ (NI USB-6361) is served as the signal generator and recorder

3.3 Absorption Database

3.3.1 Simulation at 2004 nm

The CO_2 and H_2O molecules have a large number of absorption lines near 2.0 μm. The CO_2 absorption lines near 2004 nm are selected to detect the CO_2 concentration in the study. The parameters of the absorption lines are downloaded from the HITRAN 2012 database and shown in Table 3.3 and Figure 3.9(a) [88].

Table 3.3: Spectroscopic parameters for the selected transitions for CO_2 near 2.004 μm.

λ_0 **(nm)**	v_0 **(cm^{-1})**	S**(296K) (cm^{-2}/atm)**	χ_{air}**(cm^{-1}/atm)**	χ_{self}**(cm^{-1}/atm)**
2002.026	4994.941	2.54×10^{-2}	0.07	0.096
2002.506	4993.743	2.79×10^{-2}	0.071	0.097
2002.998	4992.516	2.99×10^{-2}	0.072	0.099
2003.503	4991.259	3.13×10^{-2}	0.074	0.1
2004.019	4989.972	3.19×10^{-2}	0.075	0.102
2004.548	4988.655	3.16×10^{-2}	0.077	0.104
2005.090	4987.308	3.03×10^{-2}	0.079	0.106
2005.643	4985.932	2.79×10^{-2}	0.081	0.108
2006.209	4984.527	2.45×10^{-2}	0.0832	0.111
2006.786	4983.091	2.02×10^{-2}	0.0854	0.114
2007.377	4981.626	1.50×10^{-2}	0.0872	0.116

In the wavelength range near 2004 nm, the water-vapor absorption lines cannot be ignored. Considering the overlap of these two gases absorption lines, the spectroscopy parameters of the H_2O are listed in Table 3.4 and Figure 3.9(a).

The line strength of the CO_2 and H_2O molecules near 2004 nm are also plotted in Figure 3.9(a), in which the black lines and red lines represent CO_2 and H_2O, respectively. Figure 3.9(b) demonstrates the simulated absorbance of these absorption lines according to atmospheric conditions, where the pressure, temperature and path length are 0.95 atm, 296 K and 30 cm, respectively, CO_2 and H_2O concentrations are 450 ppm and 5.0 ‰, respectively. In Figure 3.9(b), the blue curve is the summation of the two gases. From Figure 3.9(a) and Table 3.3, we can learn that the three CO_2 lines at 2003 nm to 2004 nm (Line A, B C) almost have the largest line strength. Line B and C are relative isolated while Line A are overlapped with the H_2O line (Line F). Therefore, in order to measure the CO_2 and H_2O concentrations simultaneously and to verify that the LLSCF algorithm can be used for gas detection even when the lines are overlapping, the absorption lines between 2002.6 nm and 2004.5 nm (Figure 3.9(b), CO_2: Line A, B C; H_2O: Line F) are selected to measure the gas concentrations in the following experiments. Moreover, under the simulation conditions, the CO_2 absorbance of the

Table 3.4: Spectroscopic parameters for the selected transitions for H_2O near 2.004 μm.

λ_0 **(nm)**	v_0 **(cm^{-1})**	S**(296K) (cm^{-2}/atm)**	χ_{air}**(cm^{-1}/atm)**	χ_{self}**(cm^{-1}/atm)**
2002.303	4994.248	2.76×10^{-4}	0.0855	0.489
2002.829	4992.938	1.26×10^{-3}	0.0785	0.417
2004.492	4988.794	5.43×10^{-4}	0.0568	0.298
2004.532	4988.694	1.72×10^{-4}	0.058	0.33
2004.545	4988.664	6.56×10^{-4}	0.075	0.44
2005.143	4987.175	9.05×10^{-5}	0.099	0.492
2005.270	4986.858	1.61×10^{-4}	0.089	0.404
2005.535	4986.201	4.74×10^{-4}	0.0836	0.4
2005.819	4985.494	3.15×10^{-4}	0.08	0.353
2006.086	4984.832	2.12×10^{-4}	0.086	0.412
2006.347	4984.182	1.03×10^{-4}	0.078	0.355
2006.994	4982.576	8.62×10^{-4}	0.082	0.38

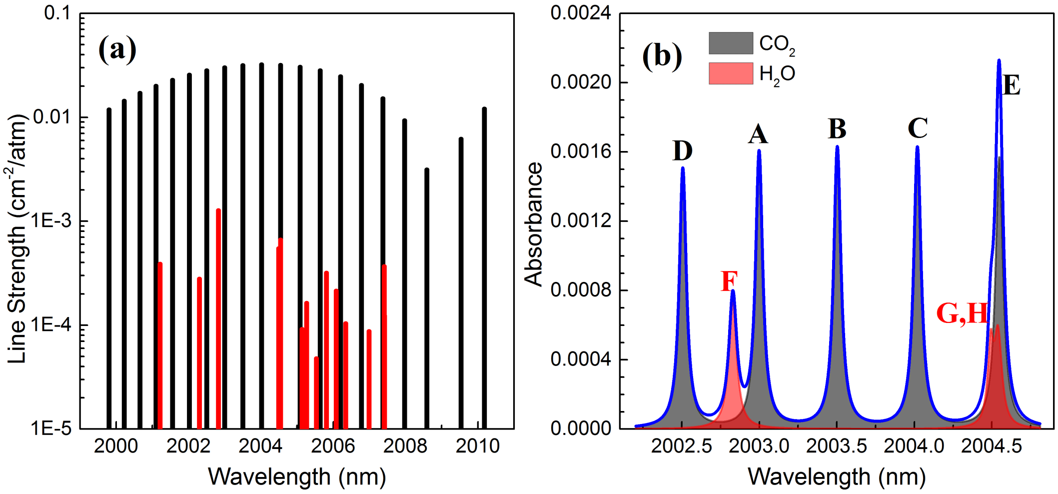

Figure 3.9: Simulations of the CO_2 and H_2O absorption lines near 2004 nm under atmospheric conditions (P=0.95 atm, T=296 K, L=30 cm, C_{CO_2}=450 ppm, C_{H_2O}=5.0 ‰) (a) is the spectrum line strength ($S(T)$) given from HITRAN, the unit has been transformed into [cm^{-2}/atm]; (b) is the simulated absorbance from 2002.2 nm to 2004.8 nm; the blue curve is the total absorbance of CO_2 and H_2O.

absorption lines is less than 2.0 ‰, which meet the assumption of weak absorbance as discussed in Section 2.2.3.

3.3.2 Simulation at 2365 nm

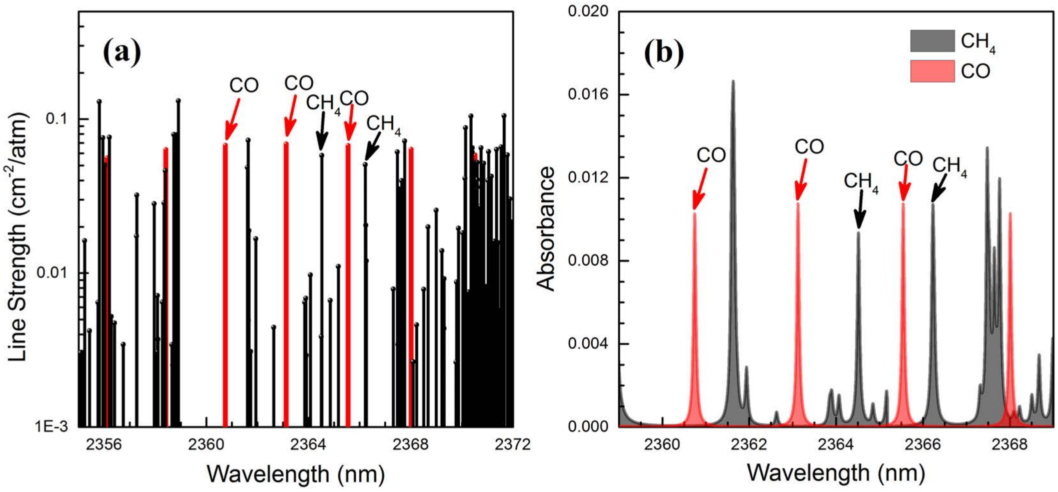

Figure 3.10: Simulations of the CO and CH_4 absorption lines near 2365 nm under atmospheric conditions (P=0.95 atm, T=296 K, L=300 cm, C_{CO}=100 ppm, C_{CH_4}=100 ppm) (a) is the spectrum line strength ($S(T)$) given from HITRAN, the unit has been transformed into [$\mathrm{cm}^{-2}/\mathrm{atm}$]; (b) is the simulated absorbance from 2359 nm to 2369 nm. The absorption lines which can be used for detection have been marked in the figure.

The line strengths of CO and CH_4 absorption lines near 2365 nm are shown in Figure 3.10(a). It can be seen that there are many CO and CH_4 absorption lines in the wavelength range. Some of the CO and CH_4 absorption lines are relative isolated as denoted in the graph. The simulations of these lines are exhibited in Figure 3.10(b), where the simulated conditions are as follows: the pressure, temperature and path length are 0.95 atm, 296 K, and 300 cm (3.0 m), respectively, and CO and CH_4 concentrations are 100 pppm and 100 ppm, respectively. As the curves shown in Figure 3.10(b), the simulated absorbance of the target gases can reach to more than 1.0% which is only a little weaker than the plots in Figure 3.9(b). Therefore, the simulated conditions are suitable for gas sensing based on the aforementioned multi-harmonic detection. However, the path length of the CO and CH_4 detections is extended 10 times than that of the CO_2 and H_2O detections at 2000 nm. To build up a compact measurement system, a multiple-path gas cell is needed for the CO and CH_4 detections.

3.4 Measurement System

As shown in Figure 3.2, the signal processing contains three sections: signal controller, harmonic detection, and concentration measurement. Signal controller refers to the signal generating and signal detecting. The signal controller is used to produce the modulation signals and to record the detected signal. The harmonic detection is separated into the digital lock-in amplifier (LIA) to produce the zeroth to fifth harmonics and the RAM determination in the first harmonic signal. The last section is the concentration calculation based on the LLSCF algorithm. All the computations are programmed in the LabVIEW software.

3.4.1 Signal control

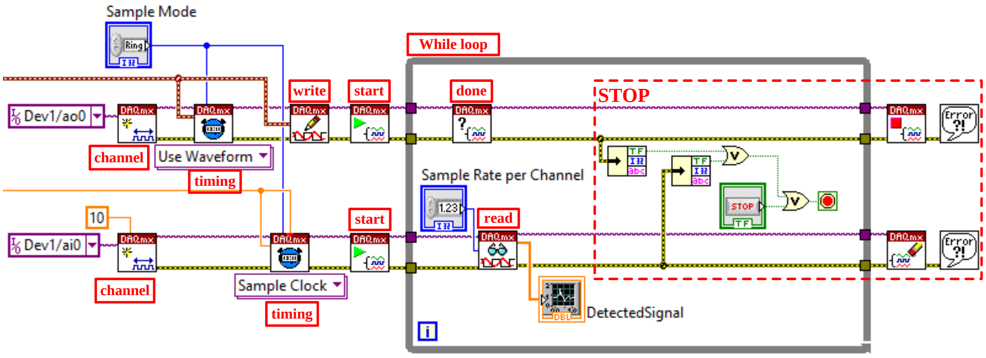

Figure 3.11: LabVIEW block diagram for signal control

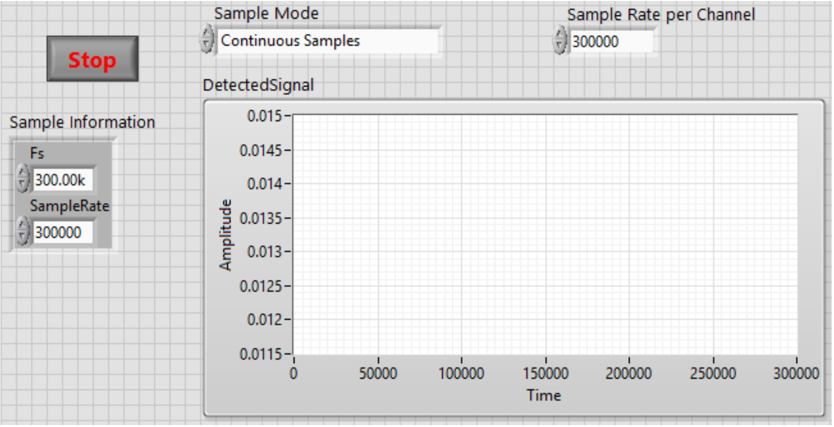

Sample Mode: Continuous Samples

Sample Rate per Channel: 300000

Sample Information

Fs: 300.00k

SampleRate: 300000

Figure 3.12: LabVIEW Front Panel of signal generating and detecting

LabVIEW (Laboratory Virtual Instrument Engineering Workbench) provides a graphical development environment for users to visualize and understand the applications, such as hardware configuration, metrics, and troubleshooting. For easily programming, LabVIEW also supplies various VIs (Virtual Instruments), for instance, signal generators, noise filters, array and numeric calculators, and graph displayers, and so on. In addition, we can create the VIs ourselves to assign the program into blocks and accelerate the data processing. Furthermore, LabVIEW can process the signal in parallel so that the data analysis speed can be effectively enhanced. Especiallt, the DAQmx VIs are used to program the NI products in LabVIEW.

The block diagram and front panel shown in Figure 3.11 and 3.12 are utilized to drive the DAQ. DAQ offers the modulations signals to the laser and records the detected signal from the PD. As shown in Figure 3.11, the program is a cycling model controlled by a while loop (the gray box). The first row in Figure 3.11 is used as output model. One output channel (Dev1/ao0) of the DAQ device is selected, and then the analog modulated signal is sent to the Write and Start Task VIs. The task is continuing until the program is stopped or some errors happen. The STOP section is marked as a dotted box in Figure 3.11. The second row is the input model, the detected signal will be wrote from the selected input channel (Dev1/ai0) of the device, and sent to the Timing and Start Task VIs. The signal is finally read in the Read VI in the loop. As illustrated in Figure 3.12, the sample model is set as continuous samples to make the program running all the time. The sample rates in the output and input models are the same (300,000) so that the detected signal can be sent to the further processing in time. The detected signal will go into the signal processing for further calculation, which should be put in the While Loop. The signal processing will be introduced in the next section.

The signal control part is designed as mentioned above. A low-frequency ramp signal with frequency of 10 Hz and amplitude of 1.2 V adding with a high-frequency sinusoidal signal with frequency of 6.0 kHz and amplitude of 60 mV is deployed as the tuning signal to modulate the laser wavelength. The ramp signal will scan the laser in a wide wavelength range, and the sine signal is used to modulate and produce the harmonic signals. The input model records the detected signal and transforms the signal to the analog signal (DAC, Digital-to-Analog Converter).

3.4.2 Digital LIA and RAM measurement

The flow chart of the signal processing which included the harmonic detection and concentration measurement is shown in Figure 3.13. The block diagram LabVIEW program can also be seen in Figure 3.18. The VIs of the digital LIA (lock-in amplifier), RAM and concentration measurement are the man-made virtual instruments for the developed system.

In order to extract the useful harmonic signals from the absorption signal, a digital LIA is developed to produce the zeroth to fifth harmonics. In the digital LIA, the reference signals are generated in the sine pattern VIs in LabVIEW. The frequencies of the reference signals are assigned according to the orders of the harmonic signals. For example, when the frequency of the modulated sine signal is 6.0 kHz, the reference signal frequency is 0 for the zeroth harmonic, 6.0 kHz for the first harmonic, and 12.0 kHz for

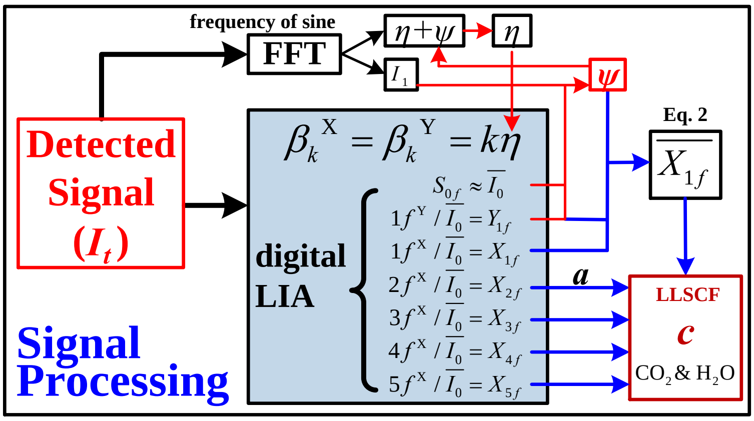

Figure 3.13: Signal processing of harmonic detection and gas concentration measurement. The red arrows are the process to determine ψ_1 in an iterative procedure. The shade part is the digital lock-in amplifier (LIA).

the second harmonic, and so on. The amplitudes of the reference signals are set as unit 1. The sample rate of the reference signals is the same as the detected signal (300,000). The assignments of the reference signal phases (β_k^{X} and β_k^{Y}) will be discussed in the next step.

The detected signal (I_t) recorded from the PD is multiplied by the different orders reference signals, and the results are sent into a Butterworth low-pass filter, in which the noises and useless signals can be removed and the highly precise harmonic signals are captured. Since the frequency of the sinusoidal signal is 6.0 kHz, the cut-off frequencies in the filters are set 500 Hz to ensure the useless noises are all moved away and the useful harmonics are kept in the output harmonic signals. Unlike some commercial lock-in amplifiers that only one harmonic can be produced at one operation and the cut-off frequency can only be set at several grades, the developed digital LIA in our system is more flexible in practical applications. For example, multiple harmonics can be produced synchronously and the cut-off frequency can be set at any values.

As the detected signal (I_t, black line) displayed in Figure 3.14, the red dash-dotted line through the black curve is the central light intensity ($\overline{I_0}$). In WMS, the $\overline{I_0}$ cannot be obtained directly from the detected signal. When setting the frequency of the reference signal to 0, the zeroth harmonic (S_{0f}) can be captured in the developed LIA. According to the approximation presented in Section 2.2.5, the zeroth harmonic (S_{0f}) can be treated as: $S_{0f} \approx \overline{I_0}$ when the absorbance is weak (absorbance$\ll$10%). Moreover, in our system, the S_{0f} is averaged from the 10 sequential scans (10 Hz ramp signal) to improve SNR, and then the acquired S_{0f} is used as the $\overline{I_0}$ to normalize the other harmonics.

Subsequently, a Fast Fourier Transform (FFT) subroutine is established to measure the first order sinusoidal modulation intensity (I_1) and the first order light intensity phase ($\eta + \psi_1$) of the instantaneous emitted laser intensity (I_0, also I_t) when the extracted frequency is set the same as sine signal (6 kHz). The curve of the I_1 , displaying

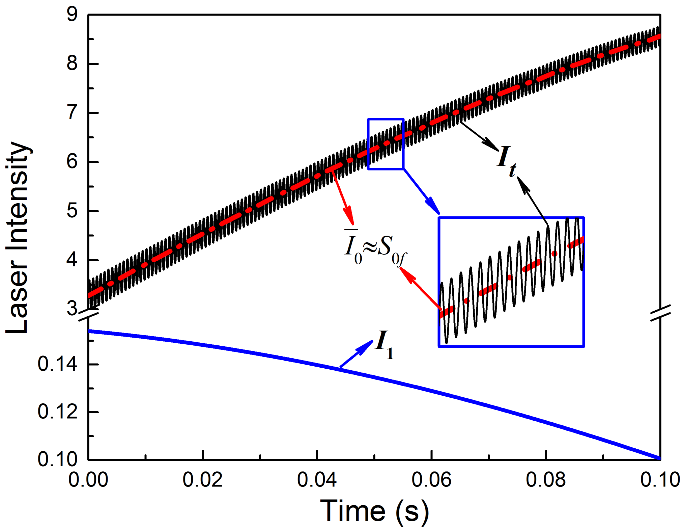

Figure 3.14: The detected signal via the photodetector (I_t) and its central light intensity ($\overline{I_0}$, red dotted line). The S_{0f} can be served as $S_{0f} \approx \overline{I_0}$ when the absorbance is weak. The modulation intensity (I_1) is obtained from an FFT subroutine.

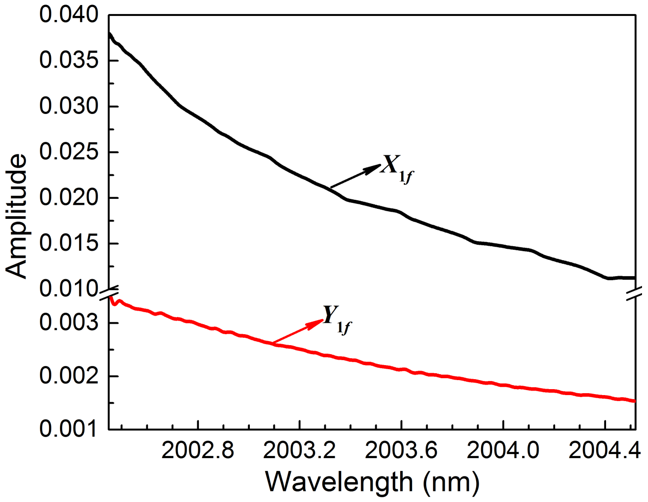

Figure 3.15: The normalized X and Y components of first harmonic in a scanning cycle, where the X_{1f} includes the RAM signal.

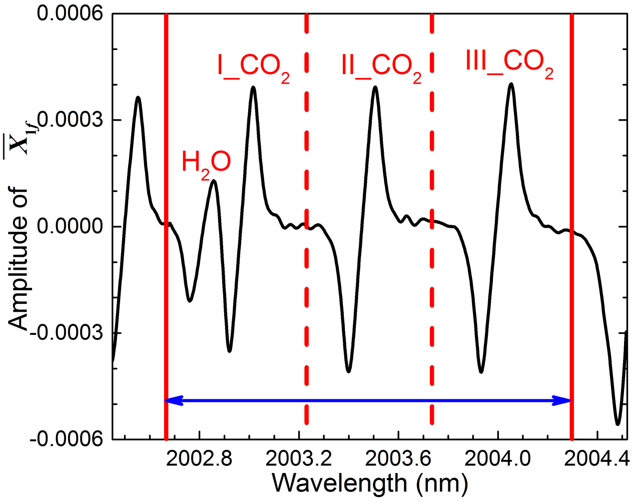

Figure 3.16: The first harmonic which the RAM signal has been eliminated.

as blue line in Figure 3.14, is retrieved from a third-order polynomial function on the light intensity. The detected signal is separated in ten segments to calculate the segment light intensities, and then the extracted intensities are used to polynomial fit the I_1 curve. From Figure 3.15, we can learn that in long tuning range, the modulation current to wavelength is a nonlinear relationship. And the first order sinusoidal modulation intensity I_1 decreases as the tuning current increases. Note that in the narrow scanning applications when only one absorption line is used, the varying in the I_1 is always neglected and the value of I_1 is considered as a constant.

Figure 3.15 exhibits the original curves of the normalized X_{1f} and Y_{1f}. Based on the discussion in Chapter 2, to assign the harmonic signal into one axis, an iterative procedure is created to determine the phase shift (ψ_1) as follows: a very first $\psi_{11} = 0°$ is used to subtract ψ_{11} in the phase ($\eta + \psi_1$) and get η_1. Then, the phase of the reference signal is set as $\beta_1^Y = \eta_1$ to receive Y_{1f}. Afterwards, according to $\overline{I_0}$, I_1 and Y_{1f}, a new ψ_{12} is obtained. The process is reiterated until ψ_1 is constant. In our system, when the sine frequency is 6.0 kHz, $\psi_1 = 6.7°$. Thereby, when given $\overline{I_0}$, I_1, ψ_1, and η, the X_{kf} and Y_{kf} are obtained by β_k^X=β_k^Y=$k\eta$ according to the formula derivations in Section 2.2.2. The concentration-dependent $\overline{X_{1f}}$ is acquired according to Eq. 2.36. The curve of the $\overline{X_{1f}}$ is illustrated in Figure 3.16. Compared the black line in Figure 3.15 and the curves in Figure 3.16, which included and excluded the RAM, the RAM in the original first harmonic is a distinct non-linear offset with gradient that submerges the harmonic signal. The RAM is complicated and difficult to determine in the wide tuning VCSEL. Consequently, we can conclude that it is important for VCSEL to eliminate RAM in the wide tuning range for the first harmonic detection. Furthermore, the second order of the sinusoidal modulation laser intensity is much smaller than the first one (less than 1.0% of I_1) so that the RAM effect of the second can be eliminated using a slope and an offset as mentioned in Chapter 2. The higher order modulation intensities (I_k) can be neglected since they are even smaller (as shown in Figure 2.6).

3.4.3 Concentration measurement

The third section is the LLSCF concentration measurement, in which an external mathematics-based Matlab script is introduced in the system for computing the gas concentration. At first, the peak positions of each absorption lines (the absorption line centers are 2002.829 nm (H_2O), 2002.998 nm (CO_2), 2003.503 nm (CO_2), and 2004.019 nm (CO_2), respectively) in the normalized second harmonic (X_{2f} (Figure 3.17)) are picked as the absorption line centers. Due to the nonlinear tuning characteristic of the laser and according to Eq. 2.13, the instantaneous wavenumber (v) can also be expressed by the tuning current (i), the expression uses the second-order polynomial function:

$$v(i) = c_2(i - i_0)^2 + c_1(i - i_0) + c_0, \tag{3.2}$$

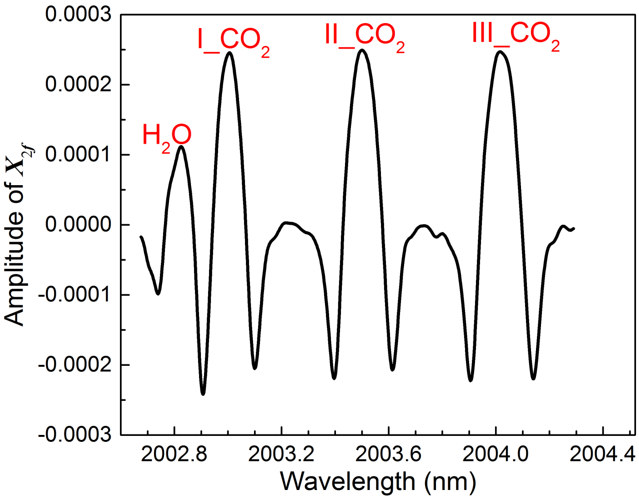

Figure 3.17: The peak positions of each absorption line in the second harmonic are served as the absorption line centers, then the laser wavelength and the modulation depth are inferred.

where i is transferred from the tuning voltage (ramp signal) and the voltage-to-current is determined by the laser controller (5 mA/V in the system); i_0 is the fixed current which can be set as the current at the line centers. The coefficients (c_2, c_1, and c_0) can be inferred from the measured line centers according to Eq. 3.2. After the wavenumber (v) being calibrated, the modulation depth in the scanning range can be calculated by:

$$a = \frac{dv(i)}{di} I_1 \varsigma(\omega) = [2c_2(i - i_0) + c_1] I_1 \varsigma(\omega), \tag{3.3}$$

where $\varsigma(\omega)$ is the frequency dependency of the current-to-wavenumber tuning coefficient, the value is set as 0.96 in the system. More information about the $\varsigma(\omega)$ can be seen in the References [52, 85].

Table 3.5: Combinations of multi-harmonic detections of CO_2 and H_2O concentrations

Output	**CO_2**	**H_2O**	**Absorption lines (CO_2, H_2O)**
1	1st harmonic	1st harmonic	(3,1)
2	2nd harmonic	2nd harmonic	(3,1)
3	3rd harmonic	3rd harmonic	(3,1)
4	1st-5th harmonic	1st-5th harmonic	(3,1)
5	1st-4th harmonic	1st-4th harmonic	(3,1)
6	2nd-5th harmonic	2nd-5th harmonic	(3,1)
7	1st-3rd harmonic	1st-3rd harmonic	(3,1)
8	2nd-4th harmonic	2nd-4th harmonic	(3,1)
9	3rd-5th harmonic	3rd-5th harmonic	(3,1)
10	1st-2nd harmonic	1st-2nd harmonic	(3,1)
11	2nd-3rd harmonic	2nd-3rd harmonic	(3,1)
12	3rd-4th harmonic	3rd-4th harmonic	(3,1)
13	1st harmonic	-	(2,0)
14	2nd harmonic	-	(2,0)
15	1st harmonic	-	(1,0)
16	2nd harmonic	-	(1,0)

After that, the determined modulation depth a is used to calculate the modulation index by $m = a/\gamma$. Then, the calibrated wavenumber v, modulation depth a and the absorption databases are utilized for computing the line profiles ($\varphi(v)$) and the k-th order Fourier component of the spectral line shape (H_k) according to the formulas in Section 2.2. Subsequently, the multiple harmonic signals with different scanning ranges are extracted to infer the gas concentrations based on the LLSCF algorithm as shown in Eq. 2.41. The LabVIEW block diagram of the measurement system is presented in Figure 3.18. The harmonic detection (digital LIA and RAM measurement) and the LLSCF concentration measurement are arranged in a while-loop so that it is running continuously. The computed concentrations of CO_2 and H_2O are stored in the designated output documents. In the output file, the combinations of multi-harmonic detections of CO_2 and H_2O concentrations are listed in Table 3.5.

The multi-harmonic CO_2 and H_2O concentration measurement is shown as a LabVIEW data processing interface in Figure 3.19. It is a real-time measurement with time resolution of 0.1 s. The top two graphs in the interface are the displayed concentrations

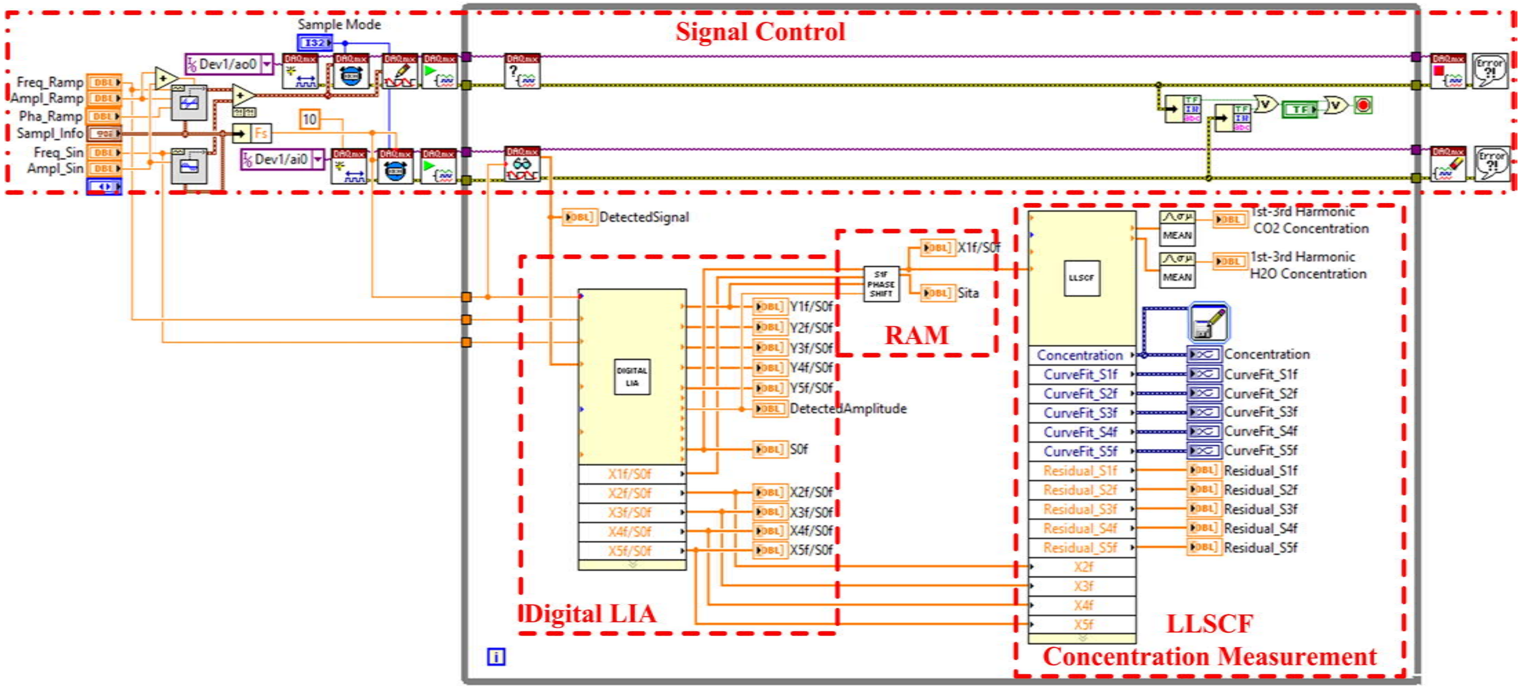

Figure 3.18: LabVIEW block diagram of the whole measurement system, which includes the signal control, the harmonic detection (digitial LIA and the RAM measurement), and the LLSCF concentration measurement. The system is arranged in a while-loop so that it is running continuously. The measured concentrations are synchronously recorded in a specified file. The curve-fitting results and concentrations are displayed in Figure 3.18.

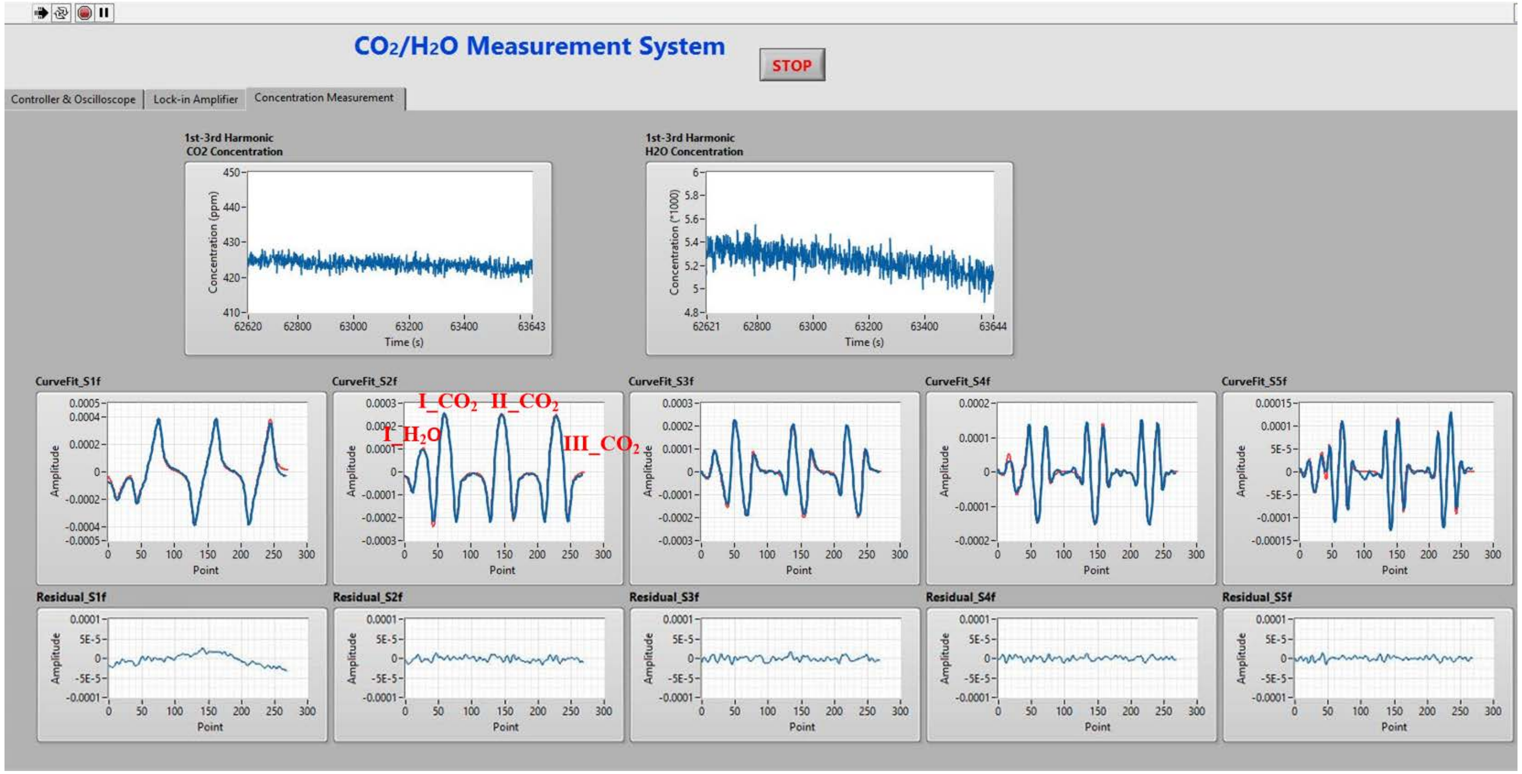

Figure 3.19: LabVIEW interface of concentration measurements (The top two graphs are the concentrations of CO_2 and H_2O; the middle five graphs are the experimental harmonics (blue lines) and the LLSCF results (red lines) from the first to fifth harmonics; the bottoms are the residuals between the experimental and the LLSCF results. The residual amplitudes are less than one-tenth of their relative harmonics, indicating the high reliability of the LLSCF algorithm. The notations of each absorption lines are marked in the second harmonics.

of CO_2 and H_2O; the middle five graphs are the experimental harmonics (blue lines) and the LLSCF results (red lines) from the first to fifth harmonics; the bottoms are the residuals between the experimental and the LLSCF results of the harmonic signals. The residual amplitudes are less than one-tenth of their relative harmonics (in an order of 1×10^{-5}), indicating the high reliability of the LLSCF algorithm. The notations of each absorption lines are also marked in the second harmonic curve.

In summary, throughout the signal processing, the essential intermediate parameters, such as the central light intensity ($\overline{I_0}$), the modulation light intensity (I_1), the wavenumber (v), the modulation depth (a), and the phases (η, ψ_1) are autonomously inferred in the absence of the standard optical components (for example etalon, beam splitter) or the additional absorption-free laser path. The software programming helps to simplify the measurement setup and operation. The entire procedure takes about 0.5s which enables the real-time measurement to continue all the time. As Eq. 2.41 demonstrates, the gas concentrations are obtained without the standard reference gas. Therefore, this system is an autonomous calibration system. It is more practical to be widely applied for the long-term in-situ trace gas measurements. The absorbance of about 2‰ for the GHG sensing ensures that the assumption of $S_{0f} \approx \overline{I_0}$ is valid in the system. Furthermore, since the central light intensity ($\overline{I_0}$) is on-the-fly measured in every scanning cycle, the fluctuations of the light intensity can be instantaneously eliminated during the measurement. This system thus can be utilized even in vibration situations where the laser path is difficult to fix.

3.5 Conclusion

In this chapter, the experimental setup and signal processing of the TDLAS-WMS measurement are introduced. The object of this chapter is to develop a high-sensitivity, high-precision, easily operated and automatically self-calibrated measurement system.

At the very first, the experimental setup and the primary experimental components are presented. And then, the absorption line parameters from the HITRAN database are extracted and the absorbance of the target gas absorption lines is simulated. The results indicate that the selected absorption lines meet the requirement of weak absorbance and can be applied for gas sensing based on the formula derivations in the previous chapter.

The signal processing of the measurement system is programmed in the LabVIEW software. In the programming, some achievements are obtained as follows:

- ◇ **Signal generating and recording**: a DAQ is utilized to produce the tuning and modulating signals, and then the absorption signal is acquired and sent to further analyzing. This step enables the system to generate the modulation signals and record the absorption signals synchronously.

- ◇ **Digital lock-in amplifier (LIA)**: the digital LIA is built up according to the theory demonstrated in Section 2.2.2. In the digital LIA, not only the multi-harmonics are produced, but also the reference signal phases are assigned as $\beta_k^X = \beta_k^Y = k\eta$ so that the concentration-dependent harmonic signal can be separated from the concentration-independent RAM signal. Thus, the entire concentration-dependent harmonic can be easily achieved at one axis, instead of using the scalar the two axes. The settings in the developed LIA are much more flexible than some of the commercial LIAs.

- **Harmonic normalization**: the zeroth harmonic is served as the central light intensities to normalize the other harmonics. In this way, the light intensity in the harmonics is removed, so the measurement gets rid of the concentration calibration in applications.
- **RAM determination**: A FFT subroutine is established to detect the sine modulation intensity and phase shifts, and then, the RAM signal in the first harmonic is determined and the highest SNR first harmonic is acquired.
- **Calibrations of wavelength**: in the long scanning range, the peak values in the second harmonic curve are used for calculate the relationship between the tuning current and the wavelength, so that the laser wavelength and the modulation depth are determined.
- **Concentration measurement**: all the intermediate properties are input or computed in the system, the gas concentration is deduced finally. The calculation process is running in a Matlab script. It is a self-calibrated system that the concentration can be obtained without calibration by the additional standard reference gases.

As described above, the developed measurement system makes best use of the information in the detected signal and the harmonics, many critical properties are deduced during the signal analysis. Hence, the system has many characteristics, such as self-calibrated, easy operated, real-time sensing, and can be applied for the long-term continuous measurement.

4 Performance of Measurements

In TDLAS-WMS, the sinusoidal signal is added to modulate the laser emitting wavelength, the harmonic signals produced via lock-in amplifier (LIA) can effectively remove the laser noises, thus, WMS can improve the sensitivity, precision and SNR in the harsh environments and in the trace gases measurements. People usually use the second harmonic for gas sensing because it has small background (RAM) signal but high SNR among all harmonics. However, each harmonic contains the useful gas information, only single harmonic employed in the gas monitoring would not get the optimal measurement results. Moreover, although the first harmonic contains the strong RAM effect, it has the highest SNR when compared with the other harmonics. It should have better performance when the RAM is eliminated.

The theory and experimental setup of the TDLAS-WMS have been discussed in the previous chapters. The RAM effect in the first harmonic has been eliminated in the signal processing. And the harmonics have been employed for gas detections. In this chapter, the performance of the first harmonic detection and the multi-harmonic detection will be presented in detail. The following questions will be demonstrated in the current chapter:

- ◇ How to evaluate the precision of the measurement?
- ◇ Can extending the scanning range enhance the measurement precision?
- ◇ How is the precision of the first harmonic detection when compared with the second and the third harmonic detections?
- ◇ How is the performance of the multi-harmonic detection when compared with the sole harmonic detection?
- ◇ With up to how many harmonics can obtain the best precision and the detection limitation in the multi-harmonic detection?
- ◇ How is the optimum integrating time for the multi-harmonic detection?
- ◇ How to verify the accuracy of the measurement system?

Furthermore, some measurement results which operated in 2017 will also be presented in the chapter (The results have been published in Lan et al. 2019 [86, 90]).

4.1 First harmonic Detection

As the simulations shown in Section 2.2.8, the first harmonic has the highest amplitude when the harmonic are modulated at the same modulation depths (modulation indices). However, due to the existence of the strong RAM, the first harmonic is very different from the other harmonics, especially in applications. As the black line shown in Figure 3.15, the first harmonic curve is submerged by the RAM. The initial first harmonic curve displays as a non-linear offset with a gradient particularly in the wide tuning situations. Chapter 3 has described the procedure to determine the RAM using the separated X and Y axes in the lock-in amplifier (which is so called the phasor decomposition method). And the RAM effect is eliminated and the pure concentration-dependent harmonic signal is then acquired. In this section, we will use the acquired first harmonic for gas detection. Moreover, to verify the importance of the RAM elimination in the first harmonic, the initial first harmonic will also be utilized for gas sensing.

4.1.1 Different scanning ranges

To assess the significance of the RAM elimination in the first harmonic, the CO_2 concentration measurements with different scanning ranges of the first harmonic are carried out in a stable environment. The curve fitting of one isolated absorption line (II_CO_2), two absorption lines (II_CO_2 and III_CO_2) and three absorption lines (I_CO_2, II_CO_2 and III_CO_2, the wavelength range is marked in Figure 3.16) are employed in the experiment.

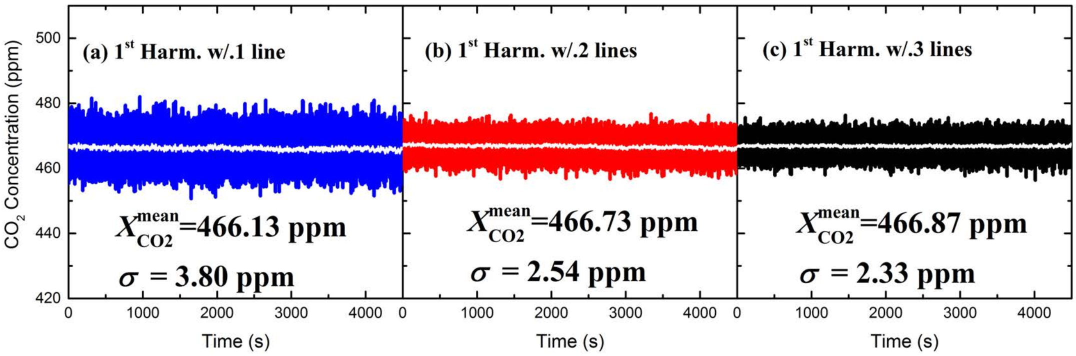

Figure 4.1: Concentration measurement based on the first harmonic with different scanning ranges (blue line: isolated absorption line; red line: two absorption lines; Black: three CO_2 absorption lines with one H_2O absorption line). The white lines at the center denote the average concentration with 10 s integrating time.

Generally, Gaussian noise exists everywhere in the measurement system. It is the statistical noise having a probability density function. The noise is mainly caused by the random factors such as the thermal effects. To verify the system's performance, the measurements are implemented in a stable climate chamber with the surrounding conditions of temperature: 296 ± 0.5 K and pressure: 0.95 ± 0.01 atm, and CO_2 and H_2O concentrations of 466.8±0.5 ppm and 5.05 ± 0.02‰, respectively. Figure 4.1 illustrates the concentration measurement results which are calculated from the first harmonic curve fitting with different scanning ranges. The time resolution of the measurement is 0.1 s. It is clear that the three absorption lines curve-fitting result has the lowest Gaussian noise while the isolated absorption line outcome has the largest Gaussian noise. It is because more absorption lines mean that more useful information is used in the calculation, the fluctuations in the signal will be suppressed so that the noise will become smaller. Therefore, it is easily concluded that extending the scanning range can reduce the measurement noise in the system.

4.1.2 Polynomial fitting

Simultaneously, the original first harmonic which contains the RAM signal is utilized for gas concentration measurement. The calculation uses the different (first, second, third and fourth) order polynomial fittings on the original first harmonic to obtain the concentrations and the results are exhibited in Figure 4.2. As can be seen, the first and second order polynomial fittings have the wrong concentrations (240 ppm and 305 ppm, respectively) while the third and fourth order polynomial fittings can obtain the similar results as the concentrations inferred from the RAM eliminated first harmonic signal. Moreover, since the fitting is calculated via three absorption lines, the Gaussian noises in the measurements results are almost the same. This can illustrate that the wide tuning wavelength can help to reduce the noise and enhance the measurement precision of the system.

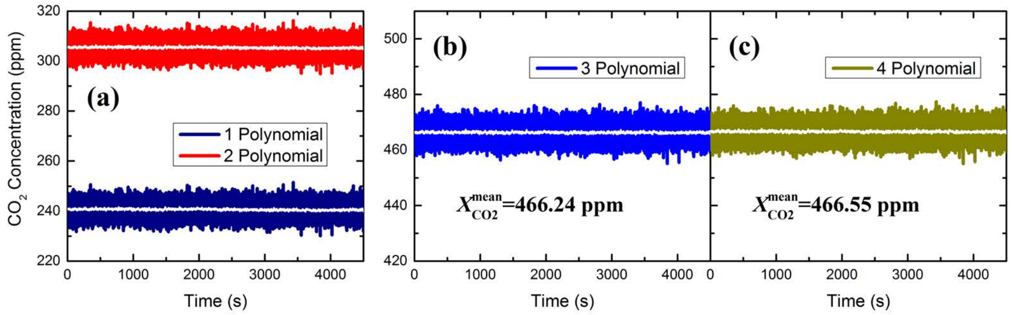

Figure 4.2: Polynomial fitting results of the original first harmonic which includes the RAM signal, the results indicate that polynomial fitting with higher than third order can infer the exact concentration.

The results demonstrate that using the third or higher order polynomial fitting, the initial first harmonic which contained the RAM signal can also acquire the same measurement results as Figure 4.1. The polynomial in the algorithm presents the RAM signal, so that the RAM can be fitted by a third or higher polynomial. The result is similar to that concluded by the previous study in [76]. However, to further improve the measurement, multi-harmonic detection will be introduced in the detection, while the polynomial fitting cannot be used in the multi-harmonic detection because the RAMs in each harmonics are different. Therefore, it is better to eliminate the RAM effect before the concentration calculation. And the aforementioned elimination process in the first harmonic is valid and can ensure the accuracy of the measurement.

On the other hand, the second and third orders light intensities are much smaller than the first order light intensity. The FFT analysis of the laser light intensity has been indicated in Figure 2.6. From the plot, we can learn that the first order light intensity is much larger (more than 100 times) than the other intensities. Thus, the RAM signal, which is produced by the correspondingly order light intensity, in the second, third or the other higher harmonic can be neglected in the LLSCF algorithm.

4.1.3 Different harmonics

The CO_2 and H_2O concentration measurements basing on the first, second and third harmonics are shown in Figures 4.3 and 4.4. The curve-fitting results of the first, second and third harmonics with three CO_2 and one H_2O absorption lines are exhibited in Figure 4.3. The SNRs of the different harmonics are denoted in their graphs. The blue lines at the bottom of the figure are the residuals between the experimental and curve-fitting results, the small amplitudes of the residuals indicate the high accuracy of the LLSCF algorithm.

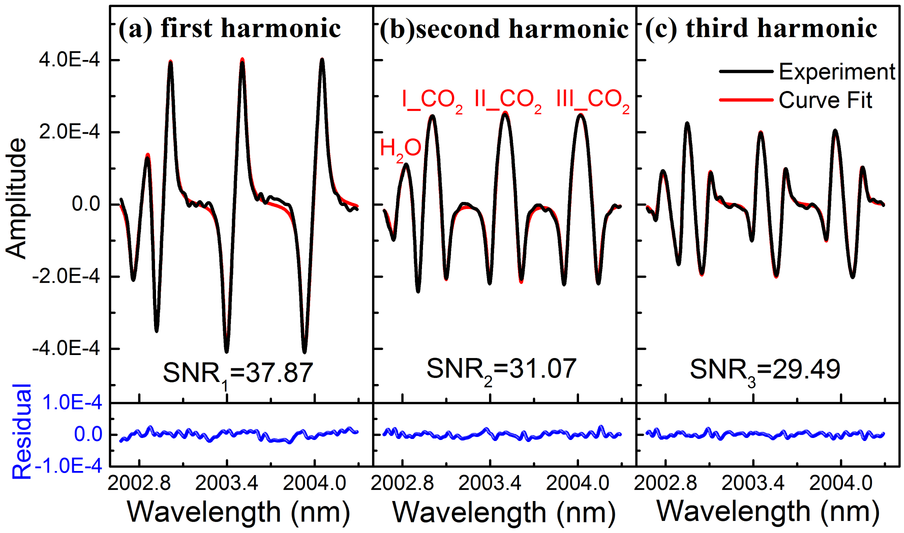

Figure 4.3: Curve fitting results of first, second and third harmonics with three CO_2 absorption lines and one H_2O absorption line; the blue lines are the residuals between the experimental and curve-fitting results.

The concentrations of the first, second and third harmonic detections with three CO_2 absorption lines and one H_2O absorption line are demonstrated in Figure 4.4. The Gaussian noises in these figures increase as the harmonic order increases, where the Gaussian noise in the first harmonic is about 17.5 ppm for CO_2 detection, while it is about 25 ppm for the second harmonic detection and nearly 40 ppm for the third harmonic detection. For the H_2O measurement, the Gaussian noise is 1.0 ‰ for the first harmonic, 1.5 ‰ for the second harmonic and 2.0 ‰ for the third harmonic, respectively. Moreover, the standard deviations displayed in the graphs are explicitly demonstrated the prevailing performance of the first harmonic detection.

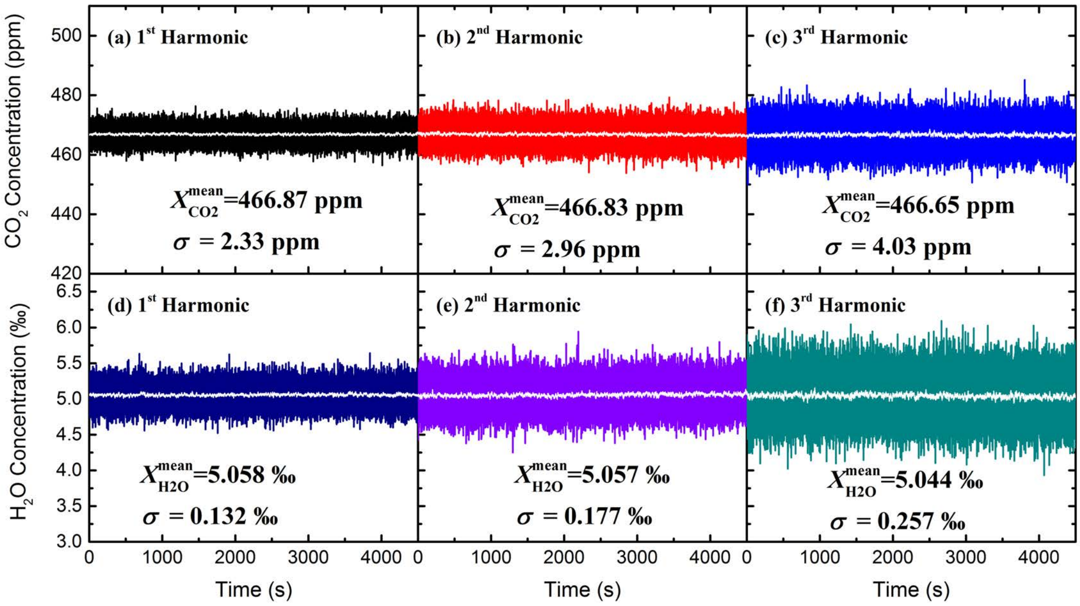

Figure 4.4: CO_2 and H_2O concentration measurements based on different harmonic (First row: first harmonic; Second row: second harmonic; Third row: third harmonic). The white lines at the center denote the average concentration with 10s integrated time. The mean values and standard deviations are denoted in the figures.

4.2 Multi-harmonic Detection

Since all harmonics contain the useful information about the gas parameters, the multi-harmonics are selected for the gas detection to improve the precision. The combinations of the multi-harmonics are listed in Table 3.5, in which CO_2 and H_2O concentrations are measured simultaneously. Under the aforementioned atmospheric conditions (temperature: 296 K, pressure: 0.95 atm) with 30 cm path length, the multi-harmonic measurement results are displayed in the following sections.

4.2.1 CO_2 measurement

Some measurement results of multi-harmonic detection in the stable environment are indicated in this section. The CO_2 and H_2O concentrations are synchronously acquired in the operation. Figure 4.5 is the CO_2 measurement with combinations of the

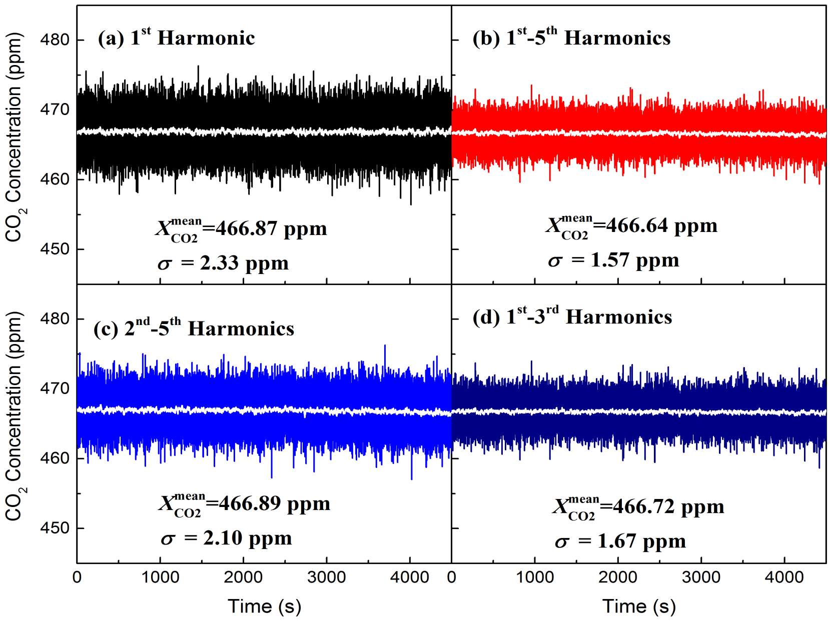

Figure 4.5: CO_2 concentration measurements in a stable chamber, the mean values and standard deviations of the measurement are denoted in the pictures. The white lines in the middle are the averaged values with 10s averaged time.

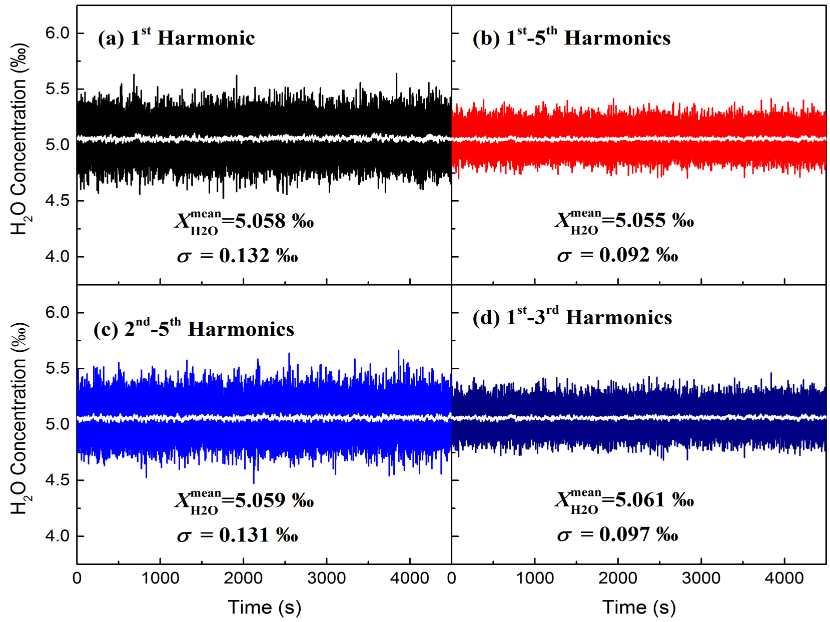

Figure 4.6: H_2O concentration measurements with different multi-harmonic combinations, the measurement rate is 0.1s and the white lines in the middle are the averaged values with 10s averaged time. The mean values and standard deviations of the whole period are also denoted in the pictures.

first harmonic detection, the first-to-fifth harmonic detection, the second-to-fifth harmonic detection and the first-to-third harmonic detection; the white lines in the middle of the data are the mean values averaged in 10 seconds from the original results. The mean concentrations and standard deviations of the whole period are also displayed in the figures. As can be seen from the plots, the first harmonic detection has the largest Gaussian noise when compared with the other combinations. That is, the multi-harmonic detections have better noise performances than the sole first harmonic detection. The more the harmonics are contained in the detections, the better noise level of the measurement. For example, the first harmonic detection has the largest standard deviation of 2.33 ppm, while the first-to-third harmonics detection has the standard deviation of 1.67 ppm and the first-to-fifth harmonics detection has the lowest standard deviation of 1.57 ppm. Moreover, the combinations which included the first harmonic have lower standard deviations than that without the first harmonic. For instance, the standard deviation of the second-to-fifth harmonics detection is 2.10 ppm, which is higher than that of the first-to-third harmonics detection (1.67 ppm).

4.2.2 H_2O measurement

Figure 4.6 is the H_2O concentration measurement with different multi-harmonic combinations. Similar to Figure 4.5, the white lines are the data averaged in 10s from the measured data, and the mean values and standard deviations exhibited in the figures are the data calculated from the whole measurement period. As indicated in the plots, the H_2O measurements have the similar results as that of the above CO_2 concentration measurements. That is, the first harmonic detection has the largest Gaussian noise level. Moreover, the multi-harmonic detections with the first harmonic have better noise performance than that without the second harmonic.

The aforementioned CO_2 and H_2O measurement results indicated that the multi-harmonic detection enables to obtain a better noise level of the gas measurement because more useful signals are utilized in the gas concentration calculation. What's more, since the first harmonic has the highest amplitude and highest SNR among all the other harmonics, the multi-harmonic combinations which contain the first harmonic can enhance the noise performance in the measurements.

4.3 Precision

4.3.1 Allan Deviation

Allan Deviation is one of the most popular methods of measuring frequency stability of the measurement system in the time domain. This method can be used to determine the intrinsic noise in a system as a function of the integrating time. It is a way of identifying and quantifying the different noise terms that exist in the inertial sensor data [94, 95]. The Allan Variance analysis of a time domain signal consists of computing its square root as a function of different integrating time and then analyzing the characteristic regions and double logarithmic scale slope of the Allan Deviation (σ_{Allan}) curves to identify the different noise modes. As the log-log plots shown in Figures 4.7, 4.8 and 4.9, the white noise ($S(f) = f^0$) is dominant when the slope is -0.5 and the Brownian noise ($S(f) = f^{-2}$) is dominant when the slope is +0.5. When the Allan Deviation (σ_{Allan}) is minimum ($\sigma^{\text{min}}_{\text{Allan}}$), the optimum integrating time (τ_{opt}) and the detection limit are determined.

4.3.2 Precision of the sole harmonic detection

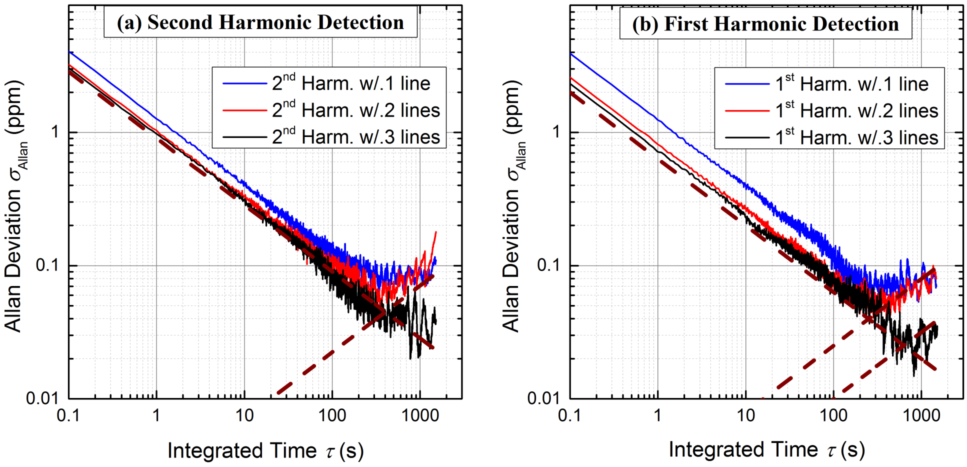

Figure 4.7: Allan Deviations of the first and second harmonic detections with different scanning ranges based on the integrating time. The dashed wine-red lines represent a slope of -0.5 and a slope of +0.5, which correspond to power densities $S(f) = f^0$ (white noise) and $S(f) = f^{-2}$ (Brownian noise), respectively. The notes "w." in the legends denote "with".

Figure 4.7 exhibits the Allan Variance analysis of the CO_2 measurement results using the first and second harmonic detections with different scanning wavelength ranges. The plots indicate that when extending the scanning range, the measurement precision will be improved. It is because the wide scanning range imports more absorption information for the calculation. For the second harmonic detection in Figure 4.7(a), compared with the isolated absorption line detecting result, the two other combinations have lower deviations during the whole integrated time. For the multiple absorption lines measurement, the two and three absorption lines have nearly the same accuracy within 100 s integrated time, where the Allan deviations are 1.04 ppm and 0.97 ppm, respectively, with 1s integrating time, 0.32 ppm with 10s averaging time and 0.12 ppm with 1 minute integrating time. The performance of the first harmonic detection in Figure 4.7(b) is similar to that of the second harmonic detection: broadening the scanning range can enhance the measurement precision. For example, at the averaging time of 10 seconds, the Allan Deviations of the first harmonic detection with one absorption line, two absorption lines and three absorption lines are 0.40 ppm, 0.27 ppm and 0.23 ppm, respectively. These consequences demonstrate that the more absorption lines utilized in the measurement, the more accurate results will be acquired.

Moreover, as can be seen in the Figure 4.3, the first harmonic curve has the highest amplitudes among all the other harmonics, so it is easy to conclude that the first harmonic detection has a better precision than that of the other harmonic detections. And the situation can also be found in Figure 4.7. For instance, the first harmonic detection with the widest scanning can reach its detection limit to 0.027 ppm with 800 seconds averaging time, while the second harmonic detection with the same tuning range only has the lowest deviation of 0.05 ppm with 400 seconds integrating time. The details of the Allan Deviation are listed in Table 4.1.

According to the aforementioned discussion, in the wide tuning range, the RAM signal in the first harmonic is distinct and the harmonic signal is submerged in the original harmonic signal. The original harmonic signal cannot be used for gas detection as shown in Figure 4.2, unless the polynomial fitting is applied for calculation. However, after eliminating the RAM signal, the first harmonic detection with different scanning ranges can obtain the accurate results and has better noise performance that the second harmonic detection. Thus, the determination of the RAM signal is important for the first harmonic detection. Moreover, multi-line scanning has wide applications in industry since several species can be monitored simultaneously.

4.3.3 Precision of the multi-harmonic detection

Figure 4.8(a) displays the Allan Deviations of the first, second and third harmonics detection with three CO_2 absorption lines, where the measurement precision decreases as the harmonic order increases. For example, at 1 s averaged time, the third harmonic has the largest deviation (about 1.27 ppm) and the first harmonic has the smallest deviation of only 0.72 ppm. The third harmonic reaches the optimal deviation of 0.09 ppm with 200 s integrating time, whereas the second achieves at 0.05 ppm with 400 s integrating time, and the first harmonic arrives at 0.027 ppm with 800s averaging time. Most of the time, the first harmonic detection has the shortest averaging time to obtain the same deviation. For instance, to acquire a deviation of 0.01 ppm, the integrating time of the first harmonic detection is 1 minute, while it would take about 1.2 minute and 3 minutes for the second harmonic detection and third harmonic detection, respectively.

Figure 4.8(b) is the Allan Deviation of the multi-harmonic detection. It is easy to learn from the plots that the multi-harmonic detections can effectively improve the measurement precision when compared with the single harmonic detection. For example, with the integrating time of 10 seconds, the second harmonic detection with three absorption lines reaches at a precision of 0.30 ppm, while the second-to-fifth harmonics detection achieves the precision of 0.20 ppm. The more harmonics included in the multi-harmonic detection, the higher measurement precision will be obtained. As the values listed in the Table 4.1, the second-to-third harmonics detection gets the precision of 0.77 ppm with 1 second averaging time, while the second-to-fifth harmonics detection obtains 0.67 ppm with the same averaging time. Moreover, we can see that there are three plots clusters in Figure 4.8(b): one is the plots without the first and second harmonics, one is the plots without the first harmonic, and the last one is the multi-harmonic combinations contain the first harmonic. The precisions of the three clusters are arranged from low to high. For instance, the cluster without the first and second harmonics can only achieve the best precision of 0.31 ppm with 10 seconds integrating time, while the cluster without the first harmonic can get 0.20 ppm and the cluster contains the first harmonic will reach to 0.16 ppm with the same averaging time. It means that in the multi-harmonic detection, the low order harmonics, which have higher amplitudes and SNRs than the high orders, can help enhance the noise performance in the gas concentration measurement.

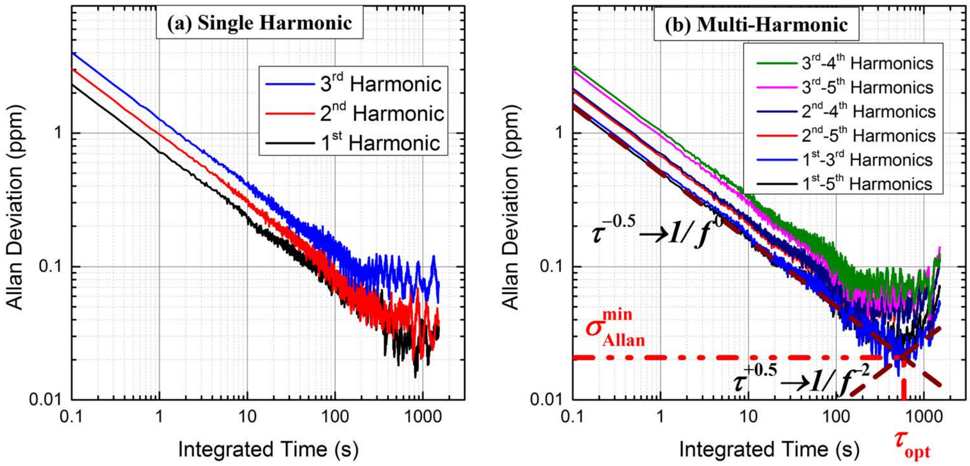

Figure 4.8: Allan Deviation for CO_2 concentration measurement of different harmonics with three CO_2 absorption lines and one H_2O absorption line. The legends in the plots are listed from top to down.

However, it doesn't always mean that the more harmonics can receive the better precision. We can find that the plots of the first-to-third harmonics detection and the first-to-fifth harmonics detection are almost coincident among the entire integrating time. They both obtain the highest precision of 0.02 ppm at 10 minutes corresponding to the absorbance of an order of 1×10^{-8}. That is because the three absorption lines have supported sufficient data for concentration calculation, the first-to-third harmonics have already gained the highest precision in measurements. More harmonics than this optimal value can no longer improve the precision in the applications of up to three absorption lines scanning. Overall, as the above descriptions and the data indicated in Table 4.1, when utilizing the first harmonic in the multi-harmonic detection, the precision of the CO_2 concentration measurement can be improved about 2–3 times.

As demonstrated in Figure 4.9, although there is only one absorption line in the H_2O concentration measurements, the performances of the H_2O concentration measurements in the multi-harmonic detection are similar to that of the CO_2 concentration measurements. At first, in the range dominated by the white noise, the third harmonic detection has lower precision than the second and first harmonic detections. For instance, the first harmonic achieves 10.8 ppm (about 0.011‰) of the deviation with 1min integrating time, while the second and first harmonic detections only obtain 7.20 ppm (about 7×10^{-3}‰) and 6.08 ppm (around 6×10^{-3}‰) with the same integrating time, respectively. Secondly, the multi-harmonic detection can enhance the measurement precision and acquire a smaller detection limitation than the single harmonic detection. With 10 seconds integrating time, the second harmonic detection achieves the precision of 0.017‰, while the second-to-third harmonics detection is 0.014‰ and the first-to-fifth harmonics detection is 0.010‰, respectively. Thirdly, there are also three different clusters in the multi-harmonic detection plots: the lowest precision is the combinations without the second and first harmonics; the combinations with the second harmonic but without the first harmonic locates in the middle, while the multi-harmonic groups which contain the first harmonic have the highest precision. In terms of the detection limitations, the lowest deviation is 1.0 ppm with 10 minutes integrating time for the first-to-third harmonics and the fir-to-fifth harmonics detections, while the lowest deviation of the second harmonic detection is 3.9 ppm with 400s averaged. Therefore, the precision of the multi-harmonic detection combined with the first harmonic is about 3 times better than that of the second harmonic detection (as illustrated in Table 4.1). Finally, in the H_2O measurements, the multi-harmonic with the first three harmonics is also sufficient to obtain the highest precision and more harmonics than this number will no longer heighten the measurement performance.

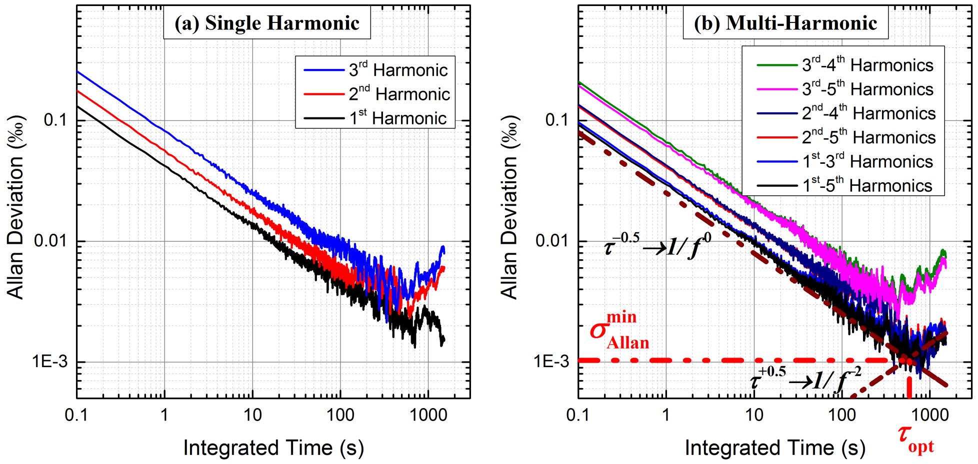

Figure 4.9: Allan Deviation for H_2O concentration measurement of different harmonics with three CO_2 absorption lines and one H_2O absorption line. The legends in the plots are listed from top to down.

Table 4.1: Overview and comparisons of the Allan Deviation analysis for CO_2 and H_2O concentration measurements

Species	Harmonics	Absorption Lines	σ_{Allan}@1s	σ_{Allan}@10s	σ_{Allan}@1min	$\sigma_{\text{Allan}}^{\text{min}}@\tau_{\text{opt}}$(Absorbance)
CO_2	1st harm.	1	1.24ppm	0.39ppm	0.16ppm	0.07ppm@300s(2.83×10^{-7})
	1st harm.	2	0.81ppm	0.27ppm	0.11ppm	0.06ppm@300s(2.42×10^{-7})
	1st harm.	3	0.72ppm	0.23ppm	0.10ppm	0.027ppm@800s(1.21×10^{-7})
	2nd harm.	1	1.27ppm	0.40ppm	0.16ppm	0.08ppm@500s(3.23×10^{-7})
	2nd harm.	2	1.04ppm	0.33ppm	0.13ppm	0.06ppm@400s(2.42×10^{-7})
	2nd harm.	3	0.97ppm	0.30ppm	0.12ppm	0.05ppm@400s(2.02×10^{-7})
	3rd harm.	3	1.27ppm	0.42ppm	0.18ppm	0.09ppm@200s(3.64×10^{-7})
	3rd-4th harm.	3	1.04ppm	0.35ppm	0.15ppm	0.07ppm@300s(2.83×10^{-7})
	3rd-5th harm.	3	0.96ppm	0.31ppm	0.14ppm	0.06ppm@300s(2.42×10^{-7})
	2nd-3rd harm.	3	0.77ppm	0.23ppm	0.10ppm	0.05ppm@500s(2.02×10^{-7})
	2nd-4th harm.	3	0.70ppm	0.22ppm	0.10ppm	0.04ppm@300s(1.82×10^{-7})
	2nd-5th harm.	3	0.67ppm	0.20ppm	0.09ppm	0.04ppm@300s(1.82×10^{-7})
	1st-2nd harm.	3	0.57ppm	0.18ppm	0.08ppm	0.02ppm@600s(8.09×10^{-8})
	1st-3rd harm.	3	0.52ppm	0.17ppm	0.07ppm	0.02ppm@600s(8.09×10^{-8})
	1st-5th harm.	3	0.49ppm	0.16ppm	0.07ppm	0.02ppm@600s(8.09×10^{-8})
H_2O	1st harm.	1	0.042‰	0.014‰	6.08ppm	1.7ppm@600s(2.69×10^{-7})
	2nd harm.	1	0.057‰	0.017‰	7.20ppm	3.9ppm@400s(5.93×10^{-7})
	3rd harm.	1	0.082‰	0.025‰	10.5ppm	4.7ppm@200s(7.15×10^{-7})
	3rd-4th harm.	1	0.066‰	0.022‰	7.87ppm	4.0ppm@400s(6.08×10^{-7})
	3rd-5th harm.	1	0.061‰	0.021‰	7.87ppm	4.0ppm@400s(6.08×10^{-7})
	2nd-3rd harm.	1	0.046‰	0.014‰	5.76ppm	2.0ppm@500s(3.04×10^{-7})
	2nd-4th harm.	1	0.043‰	0.013‰	5.42ppm	1.5ppm@800s(2.28×10^{-7})
	2nd-5th harm.	1	0.041‰	0.013‰	5.42ppm	1.5ppm@800s(2.28×10^{-7})
	1st-2nd harm.	1	0.034‰	0.012‰	4.35ppm	1.5ppm@500s(2.28×10^{-7})
	1st-3rd harm.	1	0.031‰	0.010‰	4.26ppm	1.0ppm@600s(1.52×10^{-7})
	1st-5th harm.	1	0.029‰	0.010‰	4.26ppm	1.0ppm@600s(1.52×10^{-7})

To have a quicker look at the Allan Deviation Analysis, the overview of the Allan Deviation for the CO_2 and H_2O measurements with different scanning ranges and different multi-harmonic combinations are listed in Table 4.1. The detection limitations ($\sigma_{\mathrm{Allan}}^{\mathrm{min}}$) and its corresponding optimum integrating time (τ_{opt}) and optical absorbance are included in the last row of the table.

According to the aforementioned discussions, it can summarize that the wide wavelength scanning and multi-harmonic heighten the precision because more useful absorption information is utilized in the concentration measurements. Widening the scanning range can not only measure various gas species simultaneously, but also can obtain higher precision. The higher the harmonic order, the lower the precision. That is, when the RAM signal has been eliminated, the first harmonic detection has the highest precision when compared with the second and third harmonic measurements. In the harmonics, the first harmonic has the best noise level among the other harmonics. As shown in Figure 4.3, the SNR of the first harmonic is 37.87 which is higher than the second harmonic (31.07) and the third harmonic (29.49). In the multi-harmonic detection, the series which includes the first harmonic has lower σ_{Allan} than that excludes the first harmonic. And the precision of the multi-harmonic detection can be improved for about 2–3 times when compared with the sole second-harmonic detection. More harmonics can obtain higher precision, but the first-to-third harmonics are sufficient to achieve the highest precision when three absorption lines are employed for detecting, more than the first three harmonics do not further enhance the measurement precision. The experimental results also indicate the high stability of the measurement system.

4.4 Comparison with NDIR

The above-mentioned experimental results have verified the high precision of the self-calibrated multi-harmonic measurement system. In this section, the comparison experiments are implemented to validate the accuracy of the measurement system, where the commercial NDIR sensor (Li-Cor 840A CO_2/H_2O gas analyzer) is served as a calibration standard instrument. The NDIR sensor uses a continuous broadband infrared lamp as the light source, and the light passes through the measured gas and is recorded by a photodetector, in front of which there is a light filter that can eliminate the useless wavelengths. The gas concentration is deduced based on the Beer–Lambert law. The measurement range of CO_2 is 0 ppm–20 000 ppm with less than 1 ppm signal noise at 370 ppm. And the H_2O measurement range is 0‰–60‰ with less than 0.01‰ noise level at 10‰. The measurement recording rate of the NDIR sensor is 1 s. This instrument has high accuracy over the whole measurement range because of its automatic temperature and pressure compensations. However, due to the frequency instability of the optical filter which is controlled by the piezo, the NDIR sensor must be calibrated periodically according to the application and utilization frequency.

Measurements are carried out to validate the accuracy of the TDLAS-WMS system. The gas inlet tube of the NDIR sensor is set close to the optical path of TDLAS-WMS system, thus, the gas concentrations measured in both systems are the same. When

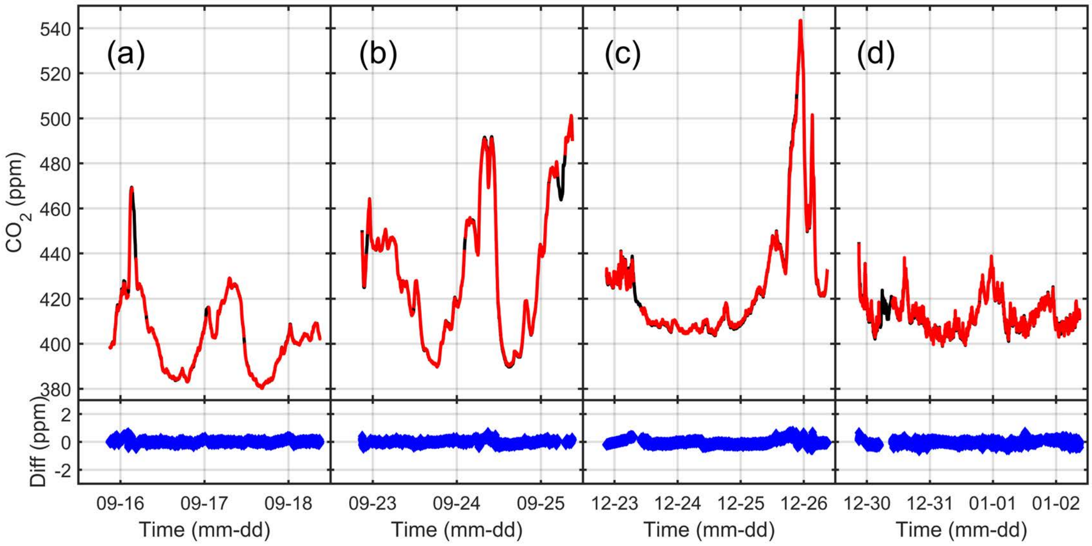

Figure 4.10: CO$_2$ measurements on two weekends (holidays) in September and December of 2017, the data is averaged in 1 minute. The black curves are the results obtained from the NDIR sensor, while the red curves are from the TDLAS-WMS sensor. The bottom figures are the differences between the NDIR and TDLAS-WMS sensors.

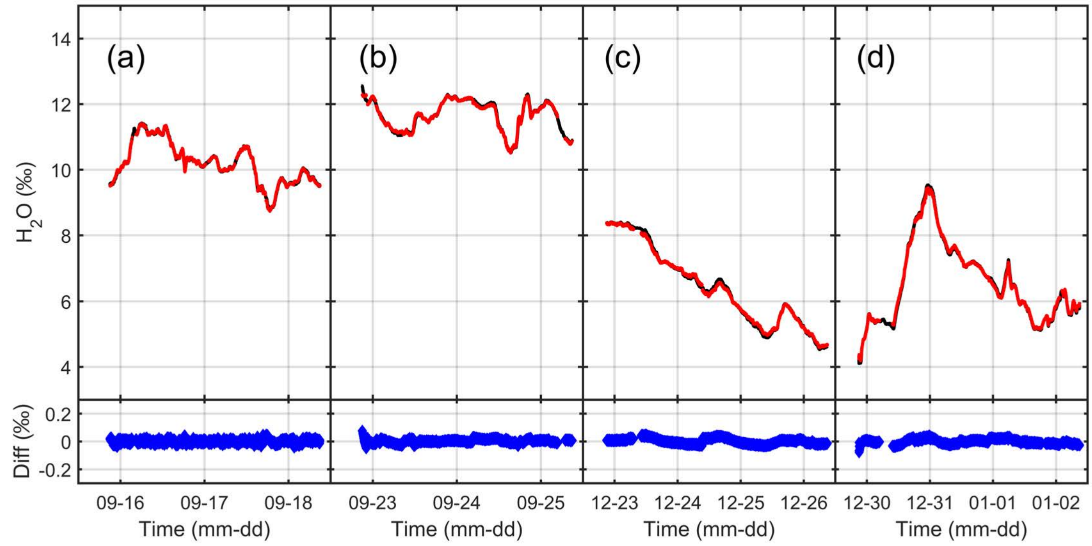

Figure 4.11: H$_2$O measurements on two weekends (holidays) in September and December of 2017, the data is averaged for 1 minute. The black curves are the results obtained from the NDIR sensor, while the red curves are from the TDLAS-WMS sensor. The bottom figures are the differences between the NDIR and TDLAS-WMS sensors.

starting the measurements, these two sensors work simultaneously and independently to acquire the concentrations of CO_2 and H_2O. Figure 4.10 and 4.11 indicate the experimental results of CO_2 and H_2O concentrations based on NDIR and TDLAS which were implemented in the Munich city center on four weekends (holidays) in September and December of 2017. For the TDLAS measurement, the outcomes are retrieved from the first-to-third harmonics detection with 1-min average for which the Allan Deviations (σ_{Allan}) are 0.07 ppm for CO_2 concentration and 4.26 ppm (4.26×10^{-3}‰) for H_2O concentration, respectively, as shown in Figures 4.8, 4.9 and Table 4.1.

As the experimental results indicated in Figure 4.10, we can learn that no matter in September or in December, both the NDIR and TDLAS measurement systems have the same CO_2 variation trends during the four different periods. The bottom graphs are the concentration residuals between these two systems, where the differences are within 1 ppm, indicating that the TDLAS system has the same level accuracy as the NDIR sensor in measuring CO_2 concentration. The CO_2 concentration in September has distinct cycles in the whole days, that is, the concentration decrease in the day and increases at night. However, in December, the diurnal cycles are not so obvious. Moreover, there was a peak value up to more than 540 ppm during the midnight of 26th of December, which was caused by a mobile-heating car set at nearby according to our recording. In the discussions of the following section, we don't take the data of this night into consideration.

Figure 4.11 exhibits the H_2O concentration measured simultaneously with the CO_2 concentration in those periods. As demonstrated in the figures, these two systems have the same H_2O results with residuals within 0.2‰, indicating the same high consistency for measuring H_2O concentration as that of CO_2 concentration. Furthermore, the H_2O concentration in September is higher than that in December. That is because in winter, the atmospheric is much drier than in autumn.

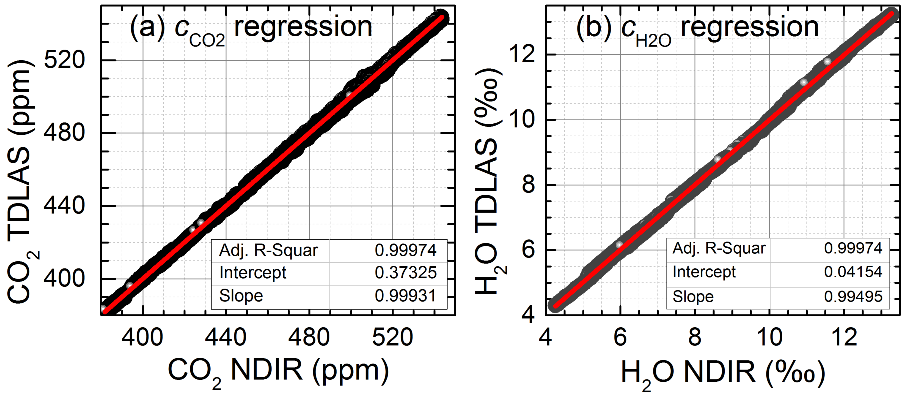

Figure 4.12: Linear regressions of CO_2 and H_2O measurements between the NDIR and the TDLAS systems.

The above comparison results between the NDIR and TDLAS sensors are represented as the linear regressions in Figure 4.12, where the regression ranges are 380 ppm – 540 ppm for CO_2 concentration and 4‰–13.5‰ for H_2O concentration. The R squares, the intercepts, and the slopes of the linear regressions are approximately 0.999, 0, and 1, respectively, demonstrating that the TDLAS sensor has high accuracy in synchronously measuring the CO_2 and H_2O concentrations; and the developed TDALS system has high consistency with the commercial NDIR instrument. It is worth mentioning that the harmonic signals of CO_2 and H_2O near 2003 nm are overlapped with each other, as shown in Figure 3.9. The experimental results show that the developed multi-harmonic measurement system based on the LLSCF algorithm can overcome the spectrum's overlapping and yield a highly accurate measurement of gas concentration.

4.5 Analysis of Data in 2017

To better understand the influences on the ground-based CO_2 variations, especially in urban areas, the aforementioned experimental results in the four different time periods are utilized for comparison and analysis. The system is located on the second floor of a laboratory at Technical University of Munich (TUM), Munich. The windows of the room are open to ensure the same CO_2 concentrations indoor and outdoor. The measurements are carried out without interference. The heating system is operated in winter to make the room to be drier than the outer environment, thus we do not analyze the H_2O concentration in this section. Only two days' data (from 6:00am of the second day to 6:00am of the fourth day) are selected for analysis in this section. The weather conditions and anthropogenic activities are displayed in the graphs. The gray parts in the figures represent the night time. The situations of the measurements are as follows: the black curve in Figure 4.13(a) is the TDLAS experimental data measured from September 16 to 18, 2017, with sunrises and sunsets at 06:53 and 19:21 (UTC+2), respectively. The red line in Figure 4.13(b) was measured from September 23 to 25, 2017. In general, the sunshine duration was nearly 12 h on these days, from 07:03 to 19:07 (UTC + 2). The solid line in Figure 4.13(c) was measured from December 23 to 25, 2017. The blue curve in Figure 4.13(d) was run from the last day of 2017 to the second day of 2018. The sun rose at 08:04 and set at 16:29 (UTC+1) with the shortest daytime of the entire year.

Some interesting findings can be seen in the experiments. Firstly, a noticeable tendency during the day and night, that is, the CO_2 concentration in the urban area decreases in the day and increases at night, is observed in September in Figure 4.13(a) and (b). The large fluctuations are caused by the synergies of the planetary boundary layer (PBL) and the vegetation photosynthesis and respiration (VPR) which are still very active in autumn [96–98]. In Figure 4.13(a), the maximum CO_2 concentration occurs at around 10:00 in the morning at about 430 ppm while the lowest point happens at around 17:00 in the afternoon at nearly 380 ppm. The weather was partly cloudy during the measured days. The trend of CO_2 concentration is reasonable because the PBL is shallow at night and deep during the day due to solar heating of the ground surface, leading to the CO_2 concentration increasing at night and decreasing in the day. Moreover, the vegetation photosynthesis uptakes CO_2 near the surface, making the CO_2

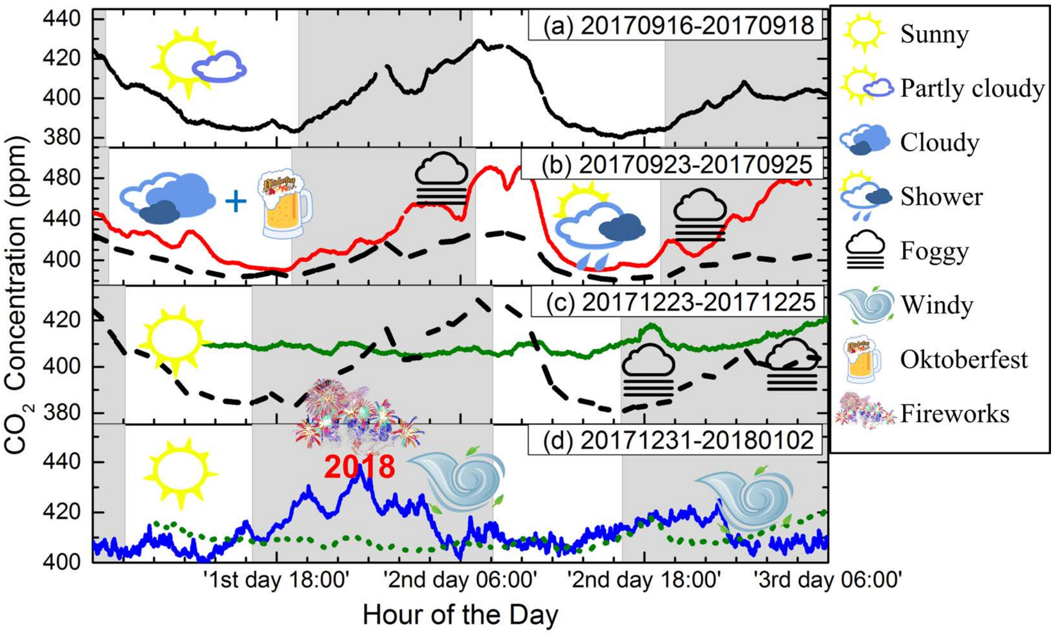

Figure 4.13: Analysis of CO_2 measurements on two weekends in September and December of 2017. The gray parts in the graphs represent the night time. (a) Measured from September 16–18, 2017. (b) Obtained from September 23–25, 2017. (c) Outcomes from December 23–25, 2017. The black-dashed lines in (b) and (c) represent the experimental results of (a). (d) Acquired from December 31, 2017 through January 2, 2018, where the green-dotted line is the data in (c). As displayed in (d), the peak value occurred at the beginning of the second day because the fireworks are lit to celebrate the coming of 2018.

concentration decrease below the average concentration (around 406 ppm) in the daytime, and the increment of CO_2 concentration at night is partly caused by the biosphere respiration. In Figure 4.13 (b), the peak and bottom values also happen at around 10:00 am and 17:00 pm, which are similar to Figure 4.13(a). However, during the night, the maximum value can reach to more than 430 ppm due to the shallow PBL, the CO_2 accumulation from vegetation respiration, the weather conditions, and the anthropogenic activities, which will be discussed in the following. The integrative effects of the PBL and the VPR result in the distinctive variations of CO_2 concentration throughout the days.

Figure 4.13(c) and (d) shows the CO_2 concentration obtained in winter with the shortest sunshine duration and the lowest temperature of the entire year. We can learn that there is no discernible variation or substantial increment and decrement during the days and nights. Compared with the curve in Figure 4.13(a) fluctuating between 380 and 430 ppm, the variation ranges shown in Figure 4.13(c) and (d) are much narrower, only vary from 405 to 420 ppm. In winter, the temperature in the atmosphere is about 0 °C and the shortest daytime is 8.4 h, and the PBL is thin to several hundred meters and does not change a lot between day and night because the solar heating is weak. The animals and plants are mostly in hibernation, with little photosynthesis and little respiration, which means no much CO_2 uptake or release from the biosphere. Therefore, the major contributor to the CO_2 concentration in the downtown area is the human activities. The CO_2 is gathered in a limited space causing higher concentration and smaller variation during the whole days than that of the autumn data. The minimum concentration in Figure 4.13(c) and (d) is above 400 ppm which approximates to the atmospheric average value.

Thirdly, the weather conditions have great impacts on the CO_2 concentration in the city center. When the meteorology is unfavorable to air diffusion, such as fog, rain, or cloudy days without wind, the CO_2 concentration in urban areas will increase quickly. For example, the red line has the peak values of more than 460 ppm which is mainly attributed to the rain and fog as demonstrated in Figure 4.13(b). The line in Figure 4.13(c), which increases to 420 ppm in the last minutes, is caused by the fog. On the contrary, when the meteorological term contributes to gas diffusion, the CO_2 concentration will noticeably decline. There were strong winds at around 04:00 of the 1st and midnight of the 2nd in January as shown in 4.13(d), and the CO_2 concentration dropped measurably from 420 to 405 ppm.

Finally, the human activities also play an important role in the CO_2 concentration variations. Considering the curves in Figure 4.13(b), where the dashed line is the experimental results of Figure 4.13(a), it is obvious that the red line has higher values than the dashed line among the whole measurement. This is because the well-known solemn celebration of the folk festival, called Oktoberfest, is held during this period every year in Munich [99, 100]. The celebration attracts millions of international tourists gathering in this city to celebrate the annual unprecedented days at Theresienwiese, which is only 2.6 km away from the monitoring site. The high concentration of the red line is partly caused by the surging tourists. For another example in Figure 4.13(d) during the New Year's Eve, many fireworks were ignited by the citizens to celebrate the arrival of 2018, which led to a CO_2 peak at midnight of the New Year [101]. After the fireworks died down, the concentration decreased from 440 to 420 ppm in 30 min, implying the significant effect of the anthropogenic activities. Moreover, the peak values in Figure 4.13(c), which were resulted from fossil fuel combustion, were also caused by anthropogenic activities.

The above-mentioned measurements have illustrated the factors that can affect the ground-based CO_2 concentration as follows: the PBL, the VPR, the seasons and weather conditions, and, most importantly, the anthropogenic activities. Thus, to better study the CO_2 concentration distribution in the urban areas, a real-time measurement instrument with high precision, accuracy, sensitivity, and stability is urgently needed, and the experimental results have demonstrated that the multi-harmonic measurement system is a potential sensor in the applications.

4.6 Conclusion

In this chapter, the precision and accuracy of the sole-harmonic detection and the multi-harmonic detection are discussed. The results are represented as below.

At first, the revised first harmonic signal which has eliminated the RAM is utilized for gas monitoring. Compared with the narrow scanning range, the first harmonic with a wide wavelength range which contains multiple absorption lines can obtain a lower noise level measurement concentration. That is to say, broadening the wavelength helps to reduce the noises. However, due to the RAM effect, the original first harmonic is deformed and cannot be applied directly for gas sensing.

Then, the initial first harmonic is employed in gas detection according to the polynomial fitting algorithm. The different orders of polynomial fittings on the original first harmonic have validated that the laser light intensity can be fitted by the third and/or higher order polynomial functions. It can acquire the similar gas concentrations as that when the RAM is eliminated in the first harmonic. It concludes that it is significant to remove the RAM signal in the first harmonic. And the RAM signal in the first harmonic is more complex than that in the other harmonics.

Allan Deviation is introduced to compute the measurements precision. According to the Allan plots of the different harmonics at different scanning ranges, we can find that widening the tuning range can enhance the precision. The lower order harmonic has a higher precision, that is, the first harmonic detection obtains the best precision among the sole-harmonic detection. The multi-harmonic detections have lower deviations than the sole-harmonic detections. The combinations of multi-harmonic detection which include the first harmonic have higher precision than those exclude the first harmonic. More harmonics used in the detection can achieve better deviations; however, the first-to-third harmonics detection with up to three absorption lines obtain the lowest deviation, more than this number of harmonics will no longer increase the measurement precision. The lowest deviation of the multi-harmonic is 0.02 ppm for CO_2 and 1.0 ppm for H_2O with 10 minutes integrating time. All in all, the multi-harmonic detection can enhance the measurement precision about 2–3 times when compared with the conventional second harmonic detection.

Subsequently, the accuracy of the TDLAS-WMS measurement system is verified by comparing with the commercial NDIR sensor (Li-Cor 840A CO_2/H_2O gas analyzer). The CO_2 and H_2O concentrations were measured simultaneously and separately. The results revealed that the developed system has high accuracy in gas sensing and has high consistency with the commercial NDIR. Furthermore, the experiments indicated that TDLAS-WMS system overcomes the spectrum's overlapping problem.

Moreover, he experimental results measured in the weekends or holidays in 2017 are used to study the influence factors on the ground-based CO_2 concentration. It summarized that the daily tendency of the ground-based CO_2 concentration was influenced by numerous factors, such as the PBL, the VPR, the seasons and weather conditions, and the anthropogenic activities.

However, the ground-based in-situ measurement is easily affected by the local emissions and the nearby interference. The weather and seasonal conditions also have great impacts on the diurnal cycles. Thus, the single-day measurements are not representative for understanding the CO_2 concentration variations in urban areas. The long-term measurement results will be discussed in the next chapters.

5 Continuous Measurement in Munich

The above chapters have already discussed about the multi-harmonic detection and have verified the precision and accuracy of the measurement system. Moreover, some measurement results in 2017 have been studied the influences on the CO_2 concentration variations in urban areas.

In this chapter, the developed measurement system is employed for the whole year CO_2 concentration observation from February 2018 to January 2019 in Munich city center. The objectives of the chapter is to study the variation of CO_2 concentration throughout the year and the impacts of different factors which would affect the ground-based CO_2 concentration in urban areas. The following contents will be presented in this chapter (Some of the content has been published in Lan et al. 2020 [102]):

- ◇ The CO_2 emission inventory in European cities and the measurement site in Munich will be presented in the first section.
- ◇ The observed H_2O concentration in June 2018 is extracted to compare to the absolute H_2O concentration measured at the nearby weather station. The comparison verifies that the observed data in our system is the same as the sensors at the weather station.
- ◇ Some external meteorological and biogenic data are imported to support the analysis of the CO_2 concentration variations in urban areas. The external data includes the ambient temperature, wind speed and wind direction, PBL height, and SIF (Solar-Induced Fluorescence) data.
- ◇ Afterwards, the diurnal, weekly, monthly, and seasonal cycles of the CO_2 concentration will be discussed. The variation patterns will be interpreted by combining with the meteorological data.
- ◇ Finally, the wind speed and direction information is utilized to analyze the influence of the wind on the observed CO_2 concentration. The polar plot and annulus methods are employed for the analyses in the last section.

5.1 Measurement Site

At the beginning of the chapter, the CO_2 emission inventory is imported to study the carbon emissions in the European main cities. ODIAC (Open-source Data Inventory for Anthropogenic CO_2) is a global high-resolution monthly emission dataset for fossil fuel carbon dioxide (CO_2) emissions from fossil fuel combustion, cement production and

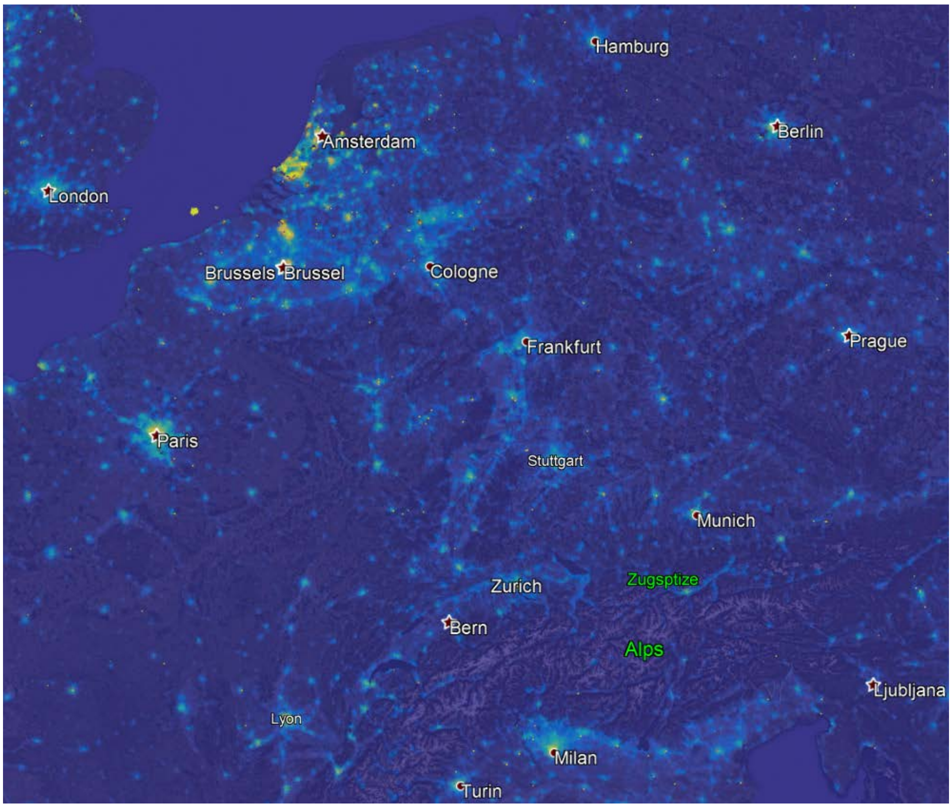

Figure 5.1: Carbon dioxide emission map in Europe based on ODIAC inventory (January 2017).

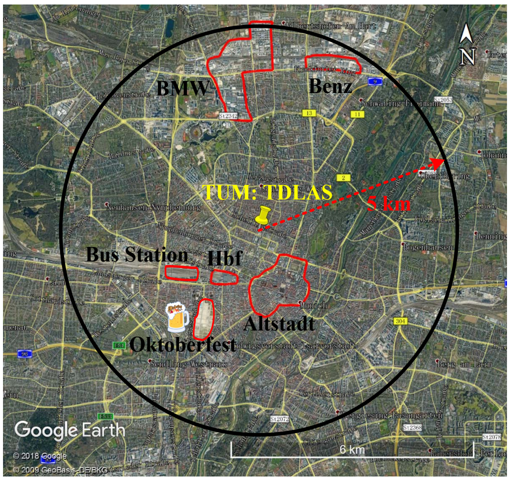

Figure 5.2: Detailed locations of the TDLAS-WMS measurement site in Munich. The Central Train Station (Hbf), Bus Station, Old Town (Altstadt), Oktoberfest, and main factories (BMW & Benz) are within a circle with a radius of 5 km around the measurement site. Map provided by @ Google Earth and @ GeoBasis DE/BKG.

gas flaring. It is developed by Greenhouse Gas Observing SATellite project, National Institute for Environmental Studies (NIES), Japan. The ODIAC data are obtained by several data servers, such as Center for Global Environmental Research at NIES, Japan. The ODIAC emission inventory includes the (CO_2) emission data from 2000 to 2016 with two different data formats: GeoTIFF (1km×1km) and netCDF (1° in latitude and 1° in longitude). The 1km×1km ODIAC emission files only include emissions over land regions. Emissions from international aviation and marine bunker emissions are NOT included [103, 104].

The CO_2 inventory of Center and West Europe in January 2017 is indicated in Figure 5.1. The bright parts in the Google Earth plot are the places with high emission sources [105]. From the plot, we can learn that the primary emissions are from the megacities such as Paris, Brussels, and Amsterdam, and industrial areas like Ruhr (near Cologne in the map). However, these megacities are very far away Munich. For example, Ruhr is about 500 km, Paris, Brussels, and Amsterdam are even further. The other cities, such as, Frankfurt, Zurich, Stuttgart and Nuremberg are with the distances of about 300 km, 240 km, 190 km and 150 km, respectively, from Munich. In the south part of the emission map, the only dense emission city is Milan, Italy, which locates on the south side of the Alps. The polluted air is hard to go pass the Alps that the south pollutant source can be ignored. Therefore, the local pollutant emissions in Munich can be served as the primary sources.

Munich, the capital city of Bavaria, is located at the south of Germany and north site of the Alps mountain range. It is an ideal city for studying the local pollutant emission since it is relatively isolated from the other huge emission cities. Munich locates at the northern side of the Alps with less than 100 km distance. The city and its metropolitan regions are home to around 6 million residents [106]. As the Munich map shown in the Google Earth in Figure 5.2, the measurement site locates at the main campus of Technical University of Munich (TUM, 48.151° N, 11.568° E). The site is in the north part of the city center, where the Central Train Station (Hauptbahnhof, Hbf), the Bus Station, the Old Town (Altstadt) and main shopping malls are within a radius of about 5 km. Moreover, some manufacturing factories, such as BMW (Bayerische Motoren Werke) and Mercedes-Benz, are north from the measurement site at a distance of approximate 3–5 km. The system is set in a room at the second floor with windows open and without human interference which to ensure that the air in the room is the same as the outdoor. There is no high emission source surrounding the site. The reliability of the measurement will be discussed in the following section.

5.2 Comparison with H_2O Measurements from a Weather Station

During the whole year campaign, the absolute CO_2 and H_2O concentrations are measured synchronously. To validate the credibility of our measurements, the obtained H_2O concentration in June 2018 is compared to the data acquired from a weather station in LMU (Ludwig Maximilian University of Munich) which is about 1 km away from our site. In the station, they use the temperature /humidity sensors, Fischer TF Sensor 401,

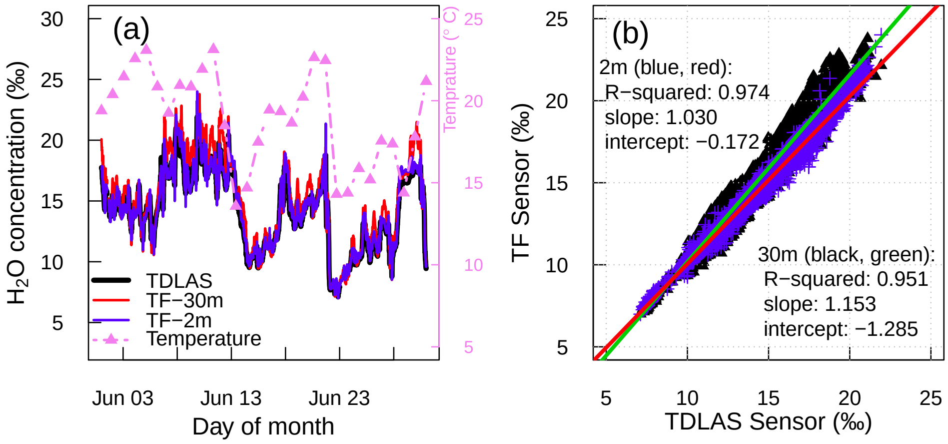

Figure 5.3: Our absolute H_2O measurements compared with weather station measurements (Fischer TF sensor). (unit: ‰, parts per thousand) (a) Our measurement data in June vs. those of the TF sensors at 2 m and 30 m a.g.l.. The temperature is averaged in every day. (b) Linear regression between TF sensor measurements at different levels and TDLAS results. It shows that the TDLAS measurement has better consistency with the TF sensor at 2 m.

which are installed at heights of 2 m and 30 m above ground level (a.g.l.) to measure temperature and humidity in every minute. For humidity measurement, the TF sensor employs the dry-bulb and wet-bulb psychrometric to determine the relative-humidity. The results we obtain from the sensor are the dry-bulb temperature (t_D in [°C], atmospheric temperature), wet-bulb temperature (t_w in [°C]) and atmospheric pressure (P in [mbar], also called humid temperature). The wet-bulb temperature is measured by the psychrometer when a quasi-equilibrium is reached between the heat lost through evaporation and the heat gained from the ambient air. The saturation vapor pressure (E_S in [mbar]) at temperature t ([°C]) can be calculated from from the formula made by Tetens [107, 108]:

$$E_S(t) = 6.1078 \cdot \exp\left(\frac{17.269t}{237.3+t}\right). \tag{5.1}$$

Then, the absolute water vapor pressure is inferred by:

$$E(t_D) = E_S(t_w) - 6.6 \times 10^{-4} P \cdot (1 + 1.15 \times 10^{-3} t_w) \cdot (t_D - t_w), \tag{5.2}$$

where $E_S(t_w)$ [mbar] is the saturation vapor pressure at wet-bulb temperature. Eq. 5.1 and 5.2 are all approximate formulas. Finally, the absolute water vapor (H_2O) concentration can be determined by:

$$C_{H_2O} = E(t_D)/P. \tag{5.3}$$

The comparison results of the absolute H_2O concentration are exhibited in Figure 5.3, which the data are averaged within 10 minutes. Figure 5.3 (a) is the H_2O concentration results measured by TDLAS system, TF sensors at 2 m and 30 m heights a.g.l., respectively. It can be learned from the curves that TDLAS measurement system has the similar fluctuation tendency with the TF sensors. The pink points are the ambient temperature and marked on the right axis. The humidity in the air varies with the variety of the atmospheric temperature. Moreover, since the TDLAS measurement site is also set near the ground (about 5 m), the TDLAS measurement result goes closer to the TF sensor at 2 m height a.g.l.. The phenomena can be seen distinct in Figure 5.3 (b), which are the linear regressions of the sensors. The blue points and the red line are the results between TDLAS and the TF sensor at 2 m a.g.l.. They have a better consistency than that with TF sensor at 30 m a.g.l.. The correlation coefficients, the slope and the intercept of the linear regression at 2 m demonstrate the high consistency and high credibility of our measurement. The comparative results reveal that the air in the measurement room is the almost the same the the air outside and our measurement results are valid for studying the CO_2 variations in urban areas.

5.3 Supporting Data for Analysis

As the discussion in Section 4.5, the ground-based CO_2 concentrations are easily affected by numerous factors, not only the meteorological conditions and the biogenic activities, but also the anthropogenic activities. In this section, some external dataset, including atmospheric temperature, wind data, PBL heights, and SIF data, are imported for supporting the analysis of CO_2 concentration in urban areas.

5.3.1 Ambient temperature

The ambient temperature is obtained from the TF sensor at 2 m a.g.l. in the weather station. Figure 5.4 is the diurnal variations of ambient temperature averaged for each month. It can be seen that the diurnal patterns are more obvious in the warm months (temperature $>$ 10°C) from April to October than the other months. In warm month, the ambient temperature increases in the daytime, and reaches to the highest at about 15:00 in the afternoon. After that, the temperature decreases until the next day morning. February 2018 is almost the coldest month during the measurement period. That is, the temperature is almost below 0°C in this month. In spring (MAM), the temperature is gradually increasing. The temperature in March is still below 10°C. However, in April, the lowest temperature exceeds 10°C. The highest temperatures in April and May are more than 20°C.

In summer (JJA), the temperature stays at the highest level with the lowest temperature above 15°C in the early morning and the highest temperature about 25–30°C in the afternoon. Then, the temperature decreases during the autumn months (SON). It reduced below 10°C in November. In winter (DJF), the temperature is almost below 5°C all day long. The diurnal temperature variations are pretty small with a difference of less than 5°C among the winter months.

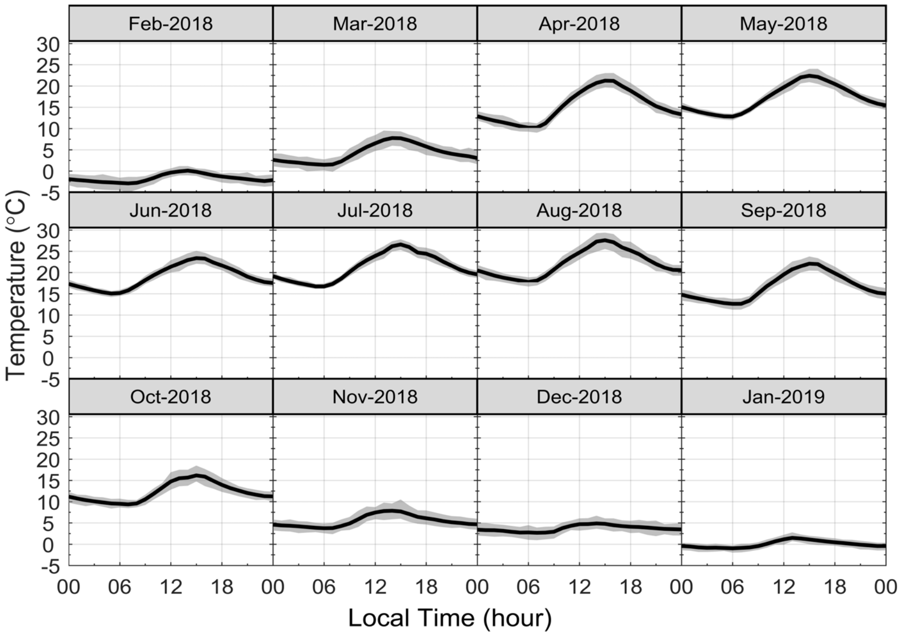

Figure 5.4: Ambient temperature averaged in every month, the gray parts are the 95% confidence intervals in every month.

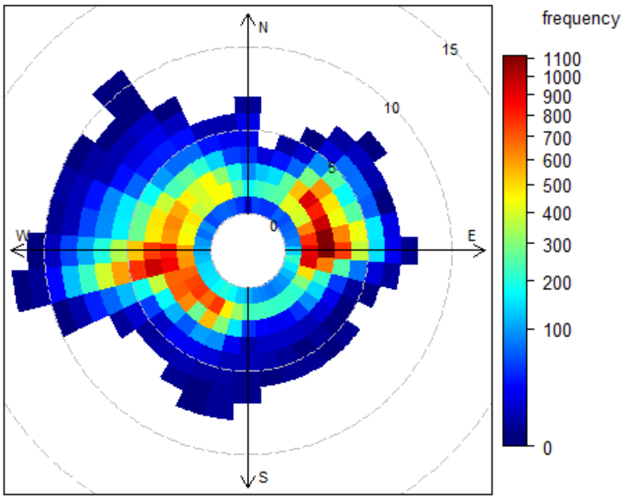

Figure 5.5: Use of polarFreq function to plot the wind speed and wind direction during the measurement period (from February 2018 to January 2019). The grid cell reveals the total hours when the wind comes from the relative wind speed and wind direction, and the number are demonstrated as the color bar on the right. The wind speed values are marked as the dashed lines in the plots. The wind from the north direction is defined to be 0° and the degree increase clockwise.

5.3.2 Wind data

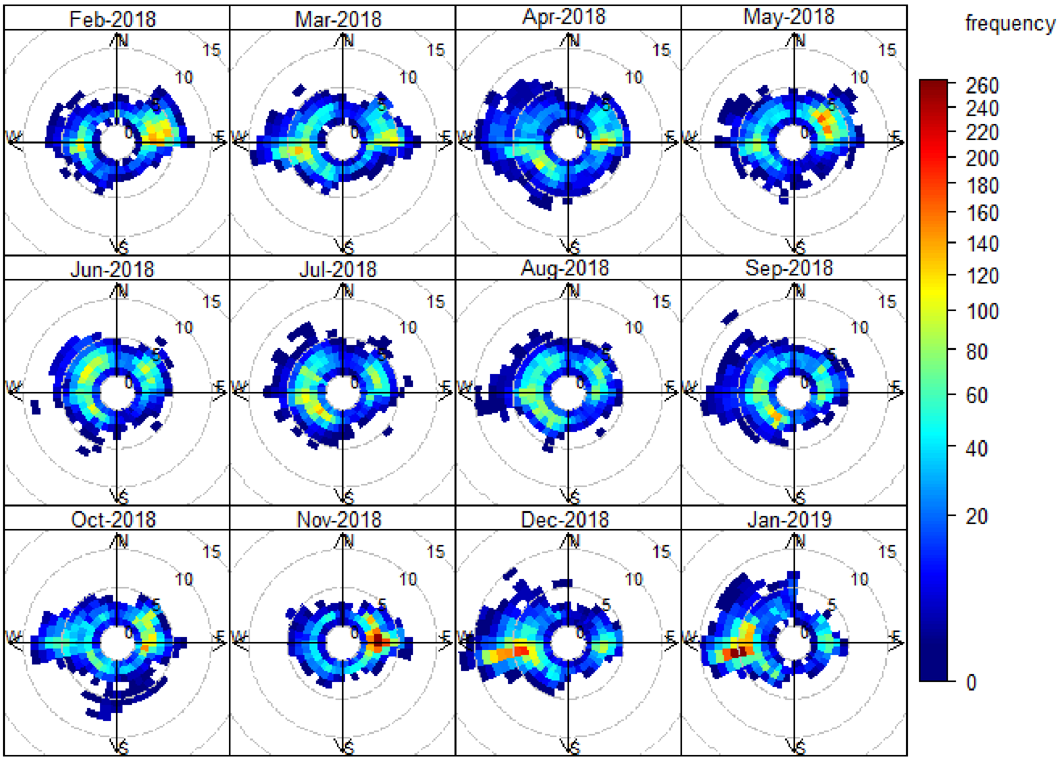

Figure 5.6: Use of polarFreq function to plot the wind speed and wind direction in each month during the measurement period.

The wind speed and wind direction are also acquired from the weather station. Using the polarFreq function in the Openair package [109], the wind speed and wind direction are shown in Figures 5.5 and 5.6. Figure 5.5 is the wind data for a whole year during the study period, while Figure 5.6 presents the wind data monthly. In the plots, the orientations mean the wind from these directions, and the radius implies the wind speed. The wind directions are divided in an interval of 10°. Each grid cell gives the total number of hours the wind is from the corresponding wind speed and direction. The number of hours is coded as a color bar shown to the right side. The nonlinear color bar helps to display the entire distribution; and the dashed circular gray lines in the plots are the wind speed scales with a unit of [m/s]. Figure 5.5 shows that the most frequent wind directions are from the northeast and southwest with wind speeds of 2–5 m/s. Defining the north direction degree to be 0° or 360°, the east: 90°, the south: 180°, and the west: 270°, the wind blows from the eastern part (0–180°) is always in low speed, while high wind speeds (more than 8 m/s) mostly come from the west and northwest directions (250–320°). Moreover, we can see that there are few occurrences when the wind comes from the direction of 10° with speed belows 4 m/s.

Figure 5.6 is the monthly polarFreq plots of the wind speed and wind direction. In spring (MAM), the wind primarily comes from the east and west. The wind directions in April distribute more uniform than the other months, some winds are from the northwest with a speed up to 10 m/s. The wind is mostly in low speeds in the summertime (JJA) with wind speed less than 6 m/s. Only few occurrences are up to 10 m/s in August. In the fall season (SON), some fast winds are from the west and south in September and October. While in November, the wind is in a very low speed; the wind primarily comes from east with wind speed of 2–4 m/s. In the wintertime (DJF), the wind is mostly from west in December and January. The wind speed can sometimes even exceed 10 m/s in December. However, the wind is often from the east side in February 2018.

5.3.3 PBL height

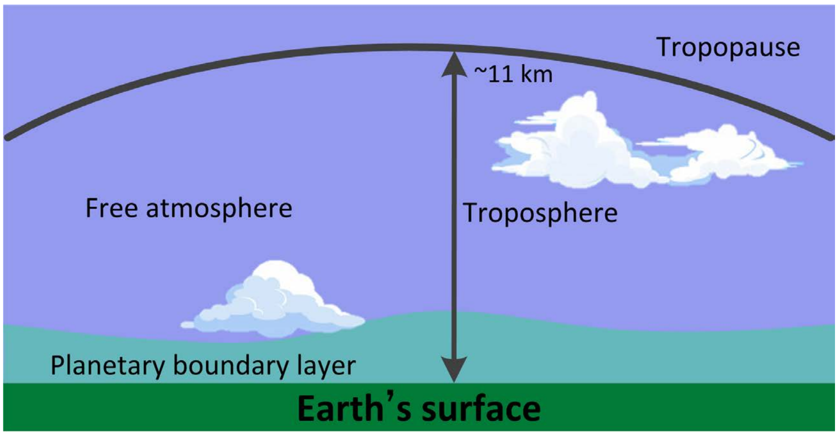

Figure 5.7: Structure of Troposphere.

Owing to the significant impact on the CO_2 concentration at ground-based, the planetary boundary layer (PBL) heights during the study phase are discussed in the section. The atmosphere is composed by several layers whose differentiation is based on the temperature profile. The layer called troposphere is the lowest layer and contains about 80% of the total air mass. Most of the atmospheric changes and influences happen there in this layer. The troposphere has got a negative temperature gradient. The temperature decreases almost linearly with the altitude, which the rate of decrease with the height is about 9.7 K/km in the dry air model. The troposphere is limited by an upper boundary which is called tropopause. The temperature at the tropopause has already decreased to an average of only 217 K [96, 110, 111]. As it is shown in Figure 5.7, we can see that the troposphere is divided into two sections: the planetary boundary layer (PBL), which is the lower section, and the free atmosphere, which is the upper section.

The behavior of the PBL is directly influenced by its contact with the planetary surface. The air within the layer is well-mixed and the top of the layer can prevent the surface air from mixing with the air in the free atmosphere. As it responds to changes in Earth's surface temperature and solar radiation, the PBL responds to these changes in an hour or less, and therefore the boundary layer height typically changes throughout the course of the day. The PBL extends from the surface to heights ranging from the earth's surface up to more than 1000 m. As the Earth's temperature decreases during the night and the surface cools, the PBL sinks during this time [112, 113].

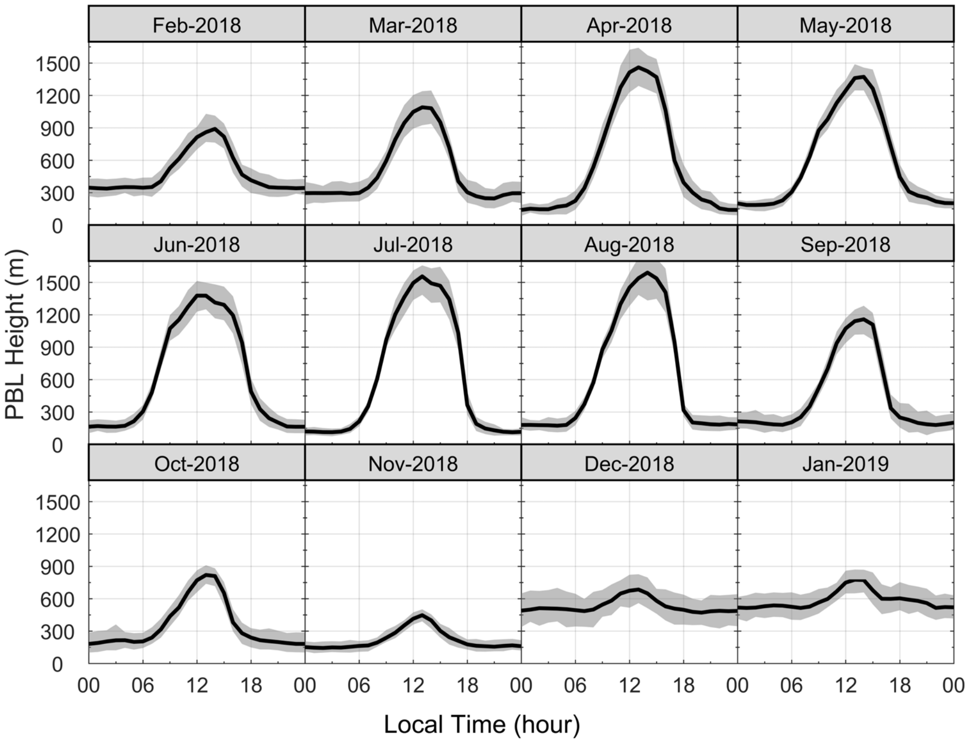

Figure 5.8: PBL height in different months, the value is acquired hourly from the backward trajectory calculation and averaged in every month. The gray shades denote the 95% confidence intervals of the PBL heights.

The PBL heights at the measurement site are extracted from the meteorology data in the air mass backward trajectory calculation in the HySPLIT model (Chapter 6). The PBL heights are the distance between the earth's surface and the mixed layer. As displayed in Figure 5.8, the diurnal PBL in the warm months (March to September), has huge variations. In the daytime when the ground is heated by the sunshine, the mixed layer can increase to more than 1200 m. Especially in the summer months (JJA), the heights in the day reach to more than 1500 m. At night when the sun goes down, the earth surface cools down and the mixed layer shallows. The PBL height in the evening can be as low as 150 m or even less. In October and November, the PBL heights in the daytime decrease sharply. The maximum height in October at noon is nearly 900 m, while the value decreases to only about 450 m in November. And the PBL stays at shallow levels at night during these two months. Compared to the other seasons, the PBL in winter is much stable. The heights do not have big changes, staying at about 300 m to 450 m most of the time. Due to the short-lived sunshine, the mixed layer depths can arrive at about 900 m in the daytime for a few hours. Given that February 2018 is the coldest month the baseline of the PBL height in this month is only 300 m, which is the shallowest level in the wintertime.

5.3.4 SIF data

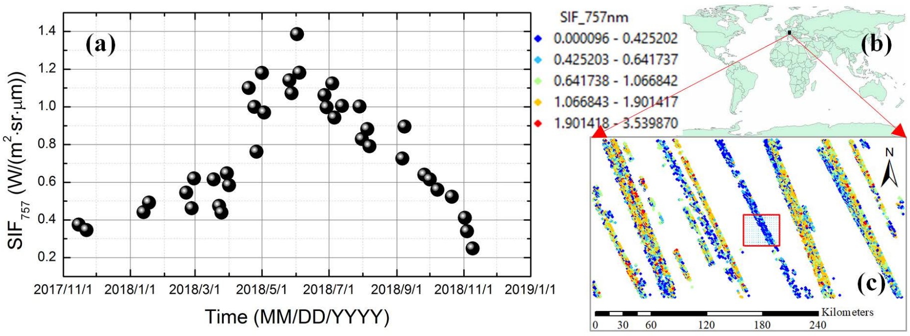

Figure 5.9: (a) SIF (Solar-Induced Fluorescence) variability in Munich and its surroundings from November 2017 to November 2018. The SIF data is obtained from the OCO-2 satellite (available at: `https://co2.jpl.nasa.gov/build/?dataset=OCO2L2Stdv8&product=FULL`, accessed on: 28 August 2019). (b) & (c) the OCO-2 tracks during the study period. (c) is the enlarged view of the black block in (b) which is the spatial domain (10–13°E, 47.5–49°N) for calculating the daily mean SIF. The red rectangular in (c) denotes the domain of Munich.

As the discussions in the previous chapter, the CO_2 sinks and sources from the biosphere also take important roles on the CO_2 diurnal variations, especially in the growing and falling seasons. Therefore, it is essential to focus on the plant photosynthesis in Munich and its surroundings. The satellite-based solar-induced fluorescence (SIF) measurement is nowadays a possible way to directly evaluate the photosynthesis strength [114, 115]. In the mechanism of photosynthesis, there are three different pathways when the light energy absorbed by the leaf chlorophyll molecules: the short wavelength with 400 nm to 700 nm is used to drive photosynthesis; the long wavelength at 660 nm to 800 nm is dissipated into heat (non-photochemistry quenching) or is re-emitted from the leaf which only accounts a small proportion and is named the so-called SIF. The SIF is an electromagnetic signal emitted by chlorophyll molecules during photosynthesis activity. Since SIF indicate plants' photosynthetic light use efficiency, it is more physiologically-based to detect the global photosynthetic activity compared to the traditionally used vegetation indices, for example, the normalized difference vegetation index and enhanced vegetation index. Thus, the SIF data can provide a better way to estimate the photosynthesis strength [116–119].

The SIF data of Munich and its surroundings (47–49.3° N, 10–13° E) in 2018 measured from the OCO-2 (Orbiting Carbon Observatory-2) satellite is shown in Figure 5.9. The data is downloaded from the webpage of the Jet Propulsion Laboratory of California Institute of Technology, United States [120]. The SIF values can be retrieved from the O_2 A-band spectrum at 757 nm and 771 nm with line width (HWHM) of about 0.021 nm. Since the transmission at 757 nm (44%) is more than twice that at 771 nm (slightly less than 20%) [116, 121], we use the SIF values retrieved at 757 nm for analysis. The temporal resolution of the SIF data is 16 days and the data is only valid until 10 November 2018. In the data processing, the negative data have been neglected and the remained data are averaged in every day. As displayed in Figure 5.9, the SIF values are valid from November 2017 to November 2018 but no data in December 2017. In the cold months (October to the next year April), the SIF is in low value, indicating the weak photosynthesis in these months. In the growing season (late spring to summer), the SIF data increases sharply from 0.5 to 1.2 $W/m^2/sr/\mu m$. In summer months, the SIF value stays at high level. And then it gradually decreases in the falling season to approximately 0.4 $W/m^2/sr/\mu m$, signifying that the photosynthesis becomes feeble.

5.4 Entire Year Measurement

5.4.1 Measurement results

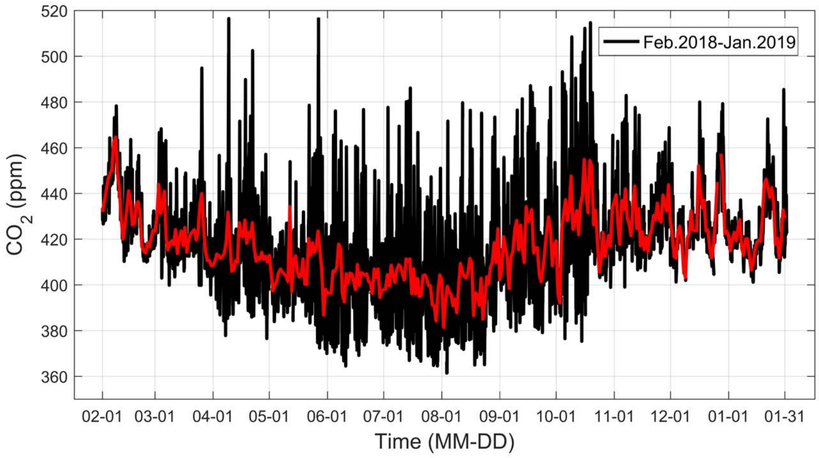

Figure 5.10: CO_2 concentrations measured from 1 February 2018 to 31 January 2019 at Munich city center, the data is averaged in 10 minutes. The red line is the daily averaged data.

The continuous multi-harmonic detection of atmospheric CO_2 and H_2O concentrations was carried out in Munich city center from 1 February 2018 to 31 January 2019.

The whole year CO_2 concentrations are retrieved from the first-to-third harmonics detection and demonstrated in Figure 5.10, where the black line is the data averaged in 10 minutes and the red line is daily averaged, respectively. The results indicate that in the middle of the year (warm months, April to October), the CO_2 concentration has larger variations than that measured in the other months. Moreover, the daily average concentration (red line) discloses that the CO_2 concentrations in urban areas decrease in the growing season (late spring to summer) and increase from autumn to winter [122]. The pattern is similar to the results shown in Figure 1.1.

5.4.2 Diurnal cycles by month and season

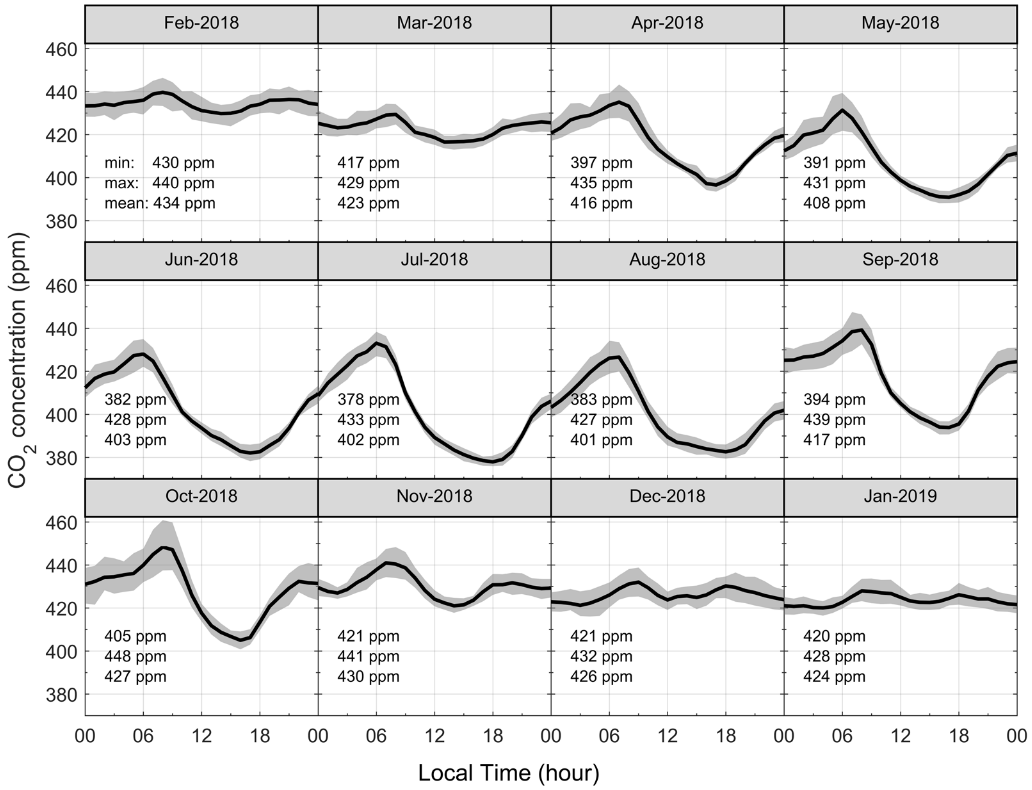

Figure 5.11: Diurnal variations of CO_2 concentration based on measurement from 1 February 2018 to the end of January 2019 at Munich city center averaged for each month. The gray shaded areas denote 95% confidence interval of the mean value. The minimum, maximum and mean values in a month are given in each subplot. Note that the January data is measured in 2019.

Figure 5.11 is the monthly-averaged CO_2 concentration curves with 95% confidence interval, where the data have significant diurnal, monthly, and seasonal variations. The minimum, maximum and mean values of the averaged curves are marked in each subplot. Based on the ambient temperature (Figure 5.4), February 2018 is almost the coldest month during the study period, the frozen climate shallows the PBL height (Figure 5.8) that the concentration in this month almost stayed at the highest level among the entire year. The details of this month will be discussed together with the other winter months in the follows.

When spring (MAM) comes, the ambient temperature increases (Figure 5.4), the daytime becomes longer and the tree leaves sprout, the photosynthesis gradually enhances in this season (Figure 5.9). Therefore, the mean concentration decreases and the CO_2 daily cycles gradually become distinct, that is the CO_2 concentration decreases in the daytime and reaches the minimum in the afternoon, and then the concentration increases at night and arrives at its maximum in the next morning. However, in the first month of spring, as the atmospheric temperature is still under 10°C, the plants are still in hibernation in Germany. The CO_2 concentration in March maintains the similar pattern as that in wintertime: it has unclear diurnal cycle but the mean concentration decreases to about 423 ppm, which is much lower than that in February (434 ppm). After March, the average temperatures in April and May rise to more than 10°C. Benefiting from the photosynthesis enhancement and PBL height increment, the diurnal cycles of the CO_2 concentration are distinct with about 40 ppm amplitudes. The highest concentration in April happens at about 7:00 LT in the morning with 435 ppm and the lowest at 16:00 LT in the afternoon with 397 ppm. The highest concentration in April occurs one hour earlier than in March (8:00). The time shift partly reflects the time switch from wintertime (UTC+1 (Coordinated Universal Time)) to summertime (UTC+2) in Europe, which occurs at the last Sunday in March. The maximum and minimum concentrations in May are around 431 ppm and 391 ppm, respectively, reducing nearly 5 ppm. Moreover, it can be found that the peak concentration in May occurs one hour earlier (6:00 am) than that in April. The time shift between these two months is likely caused by the photosynthesis enhancement. Corresponding to the SIF data in Section 5.3.4, the SIF value sharply increases so that the photosynthesis in May is stronger than that in April.

The diurnal cycles in summer (JJA) have the most distinct patterns with the largest amplitudes, which are caused by several combined effects. As the shining of the sun lasts for the longest on the earth surface in summer, the biosphere becomes most active. In the daytime, the vegetation photosynthesis consumes lots of CO_2 and decreases the CO_2 concentration. As a more "physical" factor, the heat on the ground from the sun results in an increment of PBL height and a decrement of CO_2 concentration. At night, the photosynthesis stops while vegetation respiration increases CO_2 concentration in the atmosphere. Opposite to the daytime, the temperature decreases and the PBL becomes shallow, further augmenting the tendency for an increasing CO_2 concentration. Our observation in summer is consistent with the other measurements in European cities, such as Basel, Switzerland [123, 124], London, UK [125], and Valladolid, Spain [126], their diurnal cycles also had large amplitudes (more than 30 ppm) with low concentrations in the afternoon. The curves in these three months are similar with small differences. The July data has the largest amplitude (even in the whole year) with the highest concentration of 433 ppm and the lowest concentration of 378 ppm. The highest and lowest concentrations in June and August are a little lower than 430 ppm or larger than 380 ppm, respectively. Moreover, in the afternoons of July and August, the low CO_2 concentration periods are longer than in June. Especially in August, the concentration is nearly stable from 12:00 LT to 18:00 LT. X. Zhao et al. have simulated 9-day CO_2 sinks and sources in summertime in Berlin using the WRF-VPRM model and found that the VPR is dominated in the diurnal CO_2 cycle [127]. The simulation results can support our interpretation of the observed summer data. Taking temperature (Fig. 5.4) and SIF data (Fig. 5.9) into consideration, in August, temperature in the afternoon is the highest (27.6°C, 23.4°C for June and 26.6°C for July) while the SIF data is the lowest (0.8 $W/m^2/sr/\mu m$, 1.2 $W/m^2/sr/\mu m$ for June and 1.0 $W/m^2/sr/\mu m$ for July) among the summer months. The heatwave and the pronounced drought in summer 2018 especially in August might have decreased the photosynthesis and made the CO_2 stable above 380 ppm in the afternoon [128].

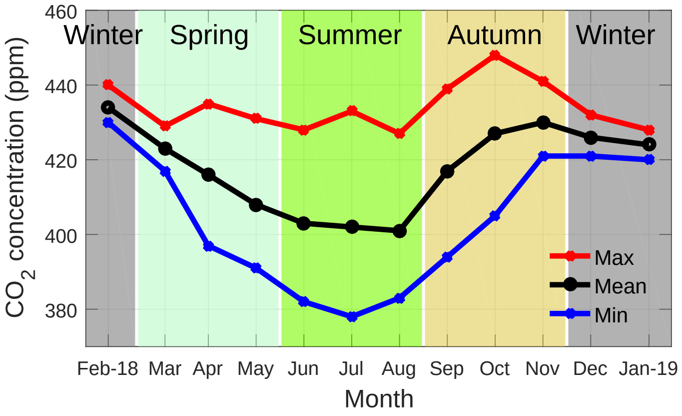

Figure 5.12: Summary of CO_2 concentration variations on the monthly plots.

In autumn (SON), the CO_2 variations follow the vegetation decay process: the CO_2 concentration increases and the variations become less distinct. The diurnal differences change from 45 ppm to 20 ppm during September to November. Moreover, the afternoon period of low CO_2 concentration becomes shorter relative to summer and the rise of CO_2 in the late afternoon is steeper and begins earlier. For example, the lowest concentration in September increases to 394 ppm at 17:00 LT while the lowest points happen at 16:00 LT with 405 ppm in October and about 14:00 LT with 421 ppm in November, respectively. From Figure 5.12, we can find that the maximum values in autumn are almost the highest among the entire year. The observation results are similar to the measurements in Chicago 2011 [97]. The October curve has the highest peak value over the year with 448 ppm. This is the time of leaf colouring, thus photosynthesis is gradually stopped (see Figure 5.9, SIF reduces from 0.7 to 0.5 $W/m^2/sr/\mu m$ from September to October). However, the dry leaves and dry grass will start to decompose delivering more CO_2. In November, since leaves fall out and the temperature reduces below 10 °C, the photosynthesis almost breaks off (see Figure 5.9, SIF below 0.5 $W/m^2/sr/\mu m$) and the PBL drops, thus, the diurnal cycle has a small amplitude with a peak concentration of 430 ppm.

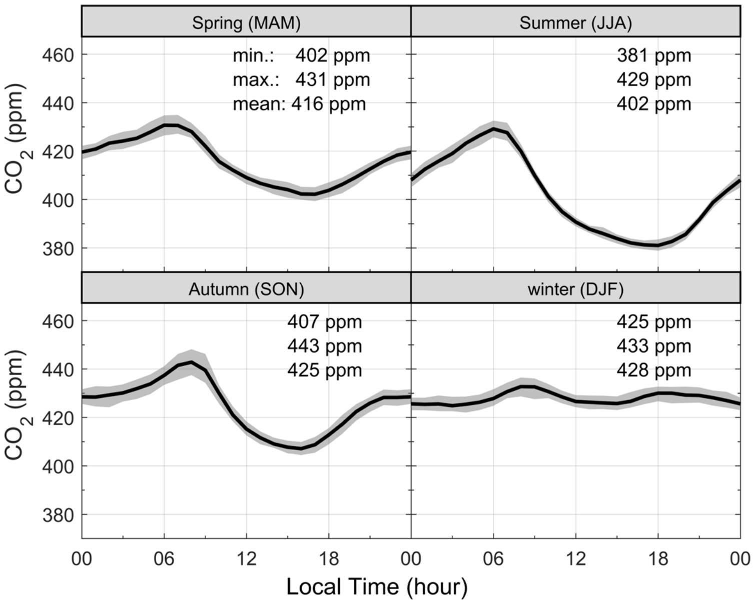

Figure 5.13: Diurnal variations of CO_2 concentration for each season with 95% confidence interval of the mean. The minimum, maximum and mean values in a month are denoted in each subplot.

Compared to the other seasons, it can be learned from the plots that there are no distinct diurnal cycles and the mean concentrations remain at the highest values in winter (DJF). The concentration differences are only 10 ppm, 11 ppm and 8 ppm in February 2018, December 2018 and January 2019, respectively. That is mainly because the sunshine is the shortest and the VPR are feeble in winter, so that there is little uptake or release of CO_2 from biosphere. On the other hand, as shown in Figure 5.4, the temperature in wintertime (below 5 °C) is lower than that in the other seasons. The carbon emission for the resident heating in urban areas would increase in the frozen situation. Furthermore, the low ambient temperature also leads to the shallow PBL with little variations (Figure 5.8), which results in the pollutant gas accumulated in the low altitude. In terms of every month data, the mean concentration in February is slightly higher (more than 8 ppm) than the values in January and December. The reason can be found from the ambient temperature (Figure 5.4) and the PBL height (Figure 5.8) episodes of this month. For these reasons, the emissions from the anthropogenic activities are the primary sources of the CO_2 variations in winter (as discussed in Section 4.5). Moreover, there are two discernible raises (around 10 ppm) in the morning (from about 6:00 am to 9:00 am) and in the afternoon (from about 16:00 pm and 19:00 pm) on the wintertime plots, which are likely caused by the the rush-hour traffic in urban areas. The diurnal cycles with two peaks in wintertime of Munich are similar to some other urban sites, such as Basel [124], London [125], and Chicago, US [97]. However, the diurnal ranges in London and Chicago (∼20 ppm) were larger than that in Basel and Munich (∼10 ppm), for London and Chicago are megacities with denser population and larger CO_2 emissions. It can be concluded that when the biogenic activities (VPR) are weak and the meteorological conditions are relative stable, the anthropogenic activities are noticeable in the CO_2 observation. Therefore, the winter CO_2 is desirable for studying the anthropogenic activities in urban areas.

The seasonal cycles are also illustrated in Figure 5.13. Similar to the above discussions, the diurnal variations in spring and autumn are smaller than that in summer. And the winter curve is the most gradual line with the peak values at the rush-hour times. Moreover, we can find that the highest and lowest CO_2 concentrations occur at various times in spring, summer and autumn. The peak position in spring happens at about 7:00 am, while it goes ahead to 6:00 am in summer and then delays to 8:00 am in autumn. The spring curve locates its lowest point at 17:00 pm, whereas the lowest concentration in summer is addressed at 18:00 pm and it goes back as early as 16:00 pm in autumn. This is most likely because of the longest sunshine duration and the highest ambient temperature in summer so that the local VPR activities and the PBL height variability dominate the CO_2 variations in summer. On the other hand, the anthropogenic CO_2 emissions are visible in winter. The analysis of the VPR and PBL effects, as well as the anthropogenic activities in summer and winter will be presented in the next chapter.

5.4.3 Variations with week days

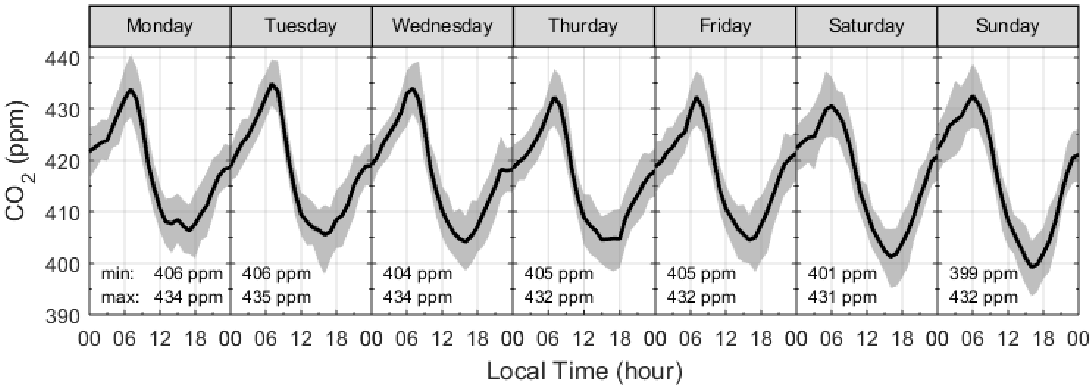

Figure 5.14: Diurnal variations of CO_2 concentration for each day of the week based on an average of our measurement from February 2018 to January 2019 at Munich city center. The gray shaded areas are 95% confidence interval of the mean. The maximum and minimum values of the curves are denoted in each panel.

The whole year observed CO_2 concentrations are averaged by days of the week and shown in Figure 5.14. It can be seen from the graphs that the diurnal variations are obvious in every day of the week: CO_2 concentration decreases in the daytime and reaches its lowest value in the afternoon, after that the concentration increases and arrives at the peak value in the next morning. The weekly patterns illustrate that the whole-year diurnal cycles are dominated by the VPR and PBL effects.

However, the workday cycles are a little different from the weekend curves. At first, the weekends' minimum concentrations have lower values than that on workdays. That is, the lowest concentrations on Saturday and Sunday are 401 ppm and 399 ppm, respectively; while the concentrations on workdays are more than 404 ppm. On workdays, people commute in the city by private cars or public transports. Traffic flows increase the CO_2 concentration in urban areas. Moreover, the highest values occur on the weekends' mornings are about one hour earlier than that on the workdays. On the workdays, the highest concentrations locate at 7:00 LT while they are 6:00 LT on weekends. The difference is probably caused by the heavy rush-hour traffic on the workday which usually peaks well after 7:00 in Munich [129, 130]. The variations for week days are quite similar to some of the previous studies in European and US cities, for example, Lietzke et al. in Basel [124], Sparks et al. in London [125], Moore et al. in Chicago [97], and Rice et al. in Portland [131], they found that CO_2 concentrations on workdays were slightly higher with later peak values compared to weekend and the results correlated with traffic volume. From the workday and weekend variations, we can confirm that the daily anthropogenic activities augment the CO_2 concentration in the city center [132]. Unlike the plots in the previous Chapter 4 that the data only captured on weekends or holidays in 2017, the CO_2 concentrations measured on both workdays and weekends may also be utilized for studying the anthropogenic activities in urban areas.

The aforementioned analyses are focused on the temporal variables of the measured CO_2 concentration. From the monthly analysis, it can be concluded that the ground-based CO_2 concentration is strongly affected by the atmospheric and biogenic factors: VPR and PBL height, particularly in the warm months and the anthropogenic activities effects are almost submerged by VPR and PBL effects during this period. The human activities can be observed clearly only in the wintertime. The weekly analysis can discover a small difference between the workdays and weekends, which is likely caused by the rush-hour traffics. However, the diurnal cycles in the weekly plots are still mainly affected by the VPR and PBL behaviors. It is difficult to analyze the anthropogenic activities when the observed results are obtained from only one measurement site.

5.4.4 Measurement in New Year's Eve

One of the shortcomings of the ground-based in-situ CO_2 measurements is that the concentration is sensitive to several factors, such as the emissions from its surrounding environments, the meteorological and weather conditions. To better understand the CO_2 concentration variations in urban areas, a special case measured during the New Year's Eve is presented in the section.

As the discussions in the previous chapter, during the New Year's Eve of 2018, the ignitions of fireworks in the city center can be noticeably observed at our measurement site. As the black curve demonstrated in Figure 5.15(a, 2017-2018), the peak is distinct a few minutes before midnight and continued until the fireworks died down. However,

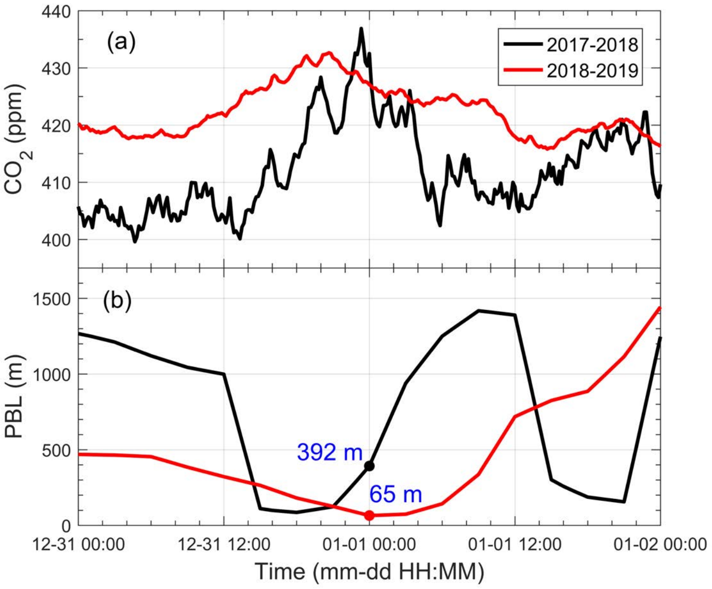

Figure 5.15: (a) CO_2 concentrations measured in the New Year's Eve of 2018 and 2019, respectively, where the concentration data are averaged in 10 minutes. (b) PBL heights during the studied periods are presented for supporting the analysis.

as the results exhibited in Figure 5.15(a, 2018-2019), the data in 2019 New Year's Eve is relatively flat without any peaks during the midnight. And the concentration was about 15 ppm higher than the data measured one year before.

Generally, the fireworks can shoot to the air of tens meter or more than one hundred metes height and then exploded. Taking the PBL heights into consideration, PBL height of 2017-2018 (Figure 5.15(b)) increased after 22:00 on 31st December 2017 and reached about 400 m at midnight. During this period, tonnes of fireworks were set off and the combustion products remained in the mix-layer. Thus, the ground-based CO_2 concentration would increase sharply. After the New Year's Eve, the CO_2 concentration decreased not only because the firework plays stopped, but also because the PBL height continued to increase to a pretty high level, the clean air at high altitude was mixed with the air at the low level and diluted the pollutant. The red curves of 2018-2019 tell us the different story. Although there were still thousands of fireworks ignited to celebrate the new coming of 2019, the measured CO_2 concentration in this period has little variations. Even the concentration tends a small decrement at midnight. In terms of PBL height, we can find that the PBL stayed in a very low altitude from the afternoon of 31st December 2018 to the morning of 1st January 2019 (less than 100 m). The lowest height was happening right at the midnight and was almost hit on the ground. The most fireworks lighted in the sky were higher than the PBL height, So that the pollutant gases would not be mixed with the air under the mixed layer. It results in the measured medium on the ground-based is much cleaner than the air above the mixed-layer (PBL).

Moreover, it can be learned from the curves that the mixed-layer has great influence on the ground-based CO_2 concentration. The tendency of the PBL height is opposite to the variations of CO_2 concentration. When PBL becomes shallow, CO_2 concentration increases. And the opposite effect is also evident: PBL increases as CO_2 concentration decreases. Compared to the curves in these two time periods, PBL in 2018–2019 is mostly lower than 2017–2018, the concentration measured in 2018–2019 is hence correspondingly higher than in 2017–2018.

In summary, according to the aforementioned analyses and discussions, CO_2 variations in urban areas are the results of numerous factors, such as PBL height, ambient temperature, meteorological conditions, VPR, time periods (seasons and months), and anthropogenic activities, and so on. It is pretty complex to distinguish all the factors and focus on analyzing the anthropogenic influence when there is only one measurement site in the study. Among all these influences, the biogenic activities (VPR) and the PBL height are dominant in the warms months; and the anthropogenic activities contribute only a small part in the diurnal cycles. In the wintertime when VPR dies down and PBL height stays relative stable, the anthropogenic activities become noticeable, and it would be a suitable time to study the human activities.

5.5 Analysis with Wind Data

In urban areas, wind speed and wind direction take important roles in pollutant transportation and distribution. In this section, the whole year CO_2 data are analyzed combining with the wind speed and wind direction (described in Section 5.3.2).

5.5.1 Analysis with wind speed

The polarPlot function in Operair package is applied in the analysis, where the polarPlot supplies a bivariate polar plot to depict the relationships between the gas concentration and the wind speed and direction. For the polarPlot figure, the wind speed, wind direction and CO_2 concentration are taken parts into the wind speed-direction bins and the mean CO_2 concentration is computed in each bin. Then the bins would be made as a continuous surface using the smoothing techniques. The polar plot of the measurement results is displayed in Figure 5.16. Similar to the polarFreq function, the orientations in the figure represent the wind coming from these directions, and the radius implies the wind speed values. The wind speed is denoted as a unit of [m/s] in the graph. The color bar indicates the range of CO_2 concentration in the polar map.

Figure 5.16 is the whole year polar plot, the red or bright parts indicate that the high concentrations would come from the corresponding wind speeds and directions. It can be learned that most of the time low wind speed (less than about 3 m/s) results in the high gas concentration. It is because when the air is stationary, the emissions are trapped in the city. Thus, the local emissions are the major pollutant in Munich city center [133]. The outer rings often shows the low concentrations, for the high wind speed blows away the pollutants in the city and brings fresh air from rural areas to dilute the

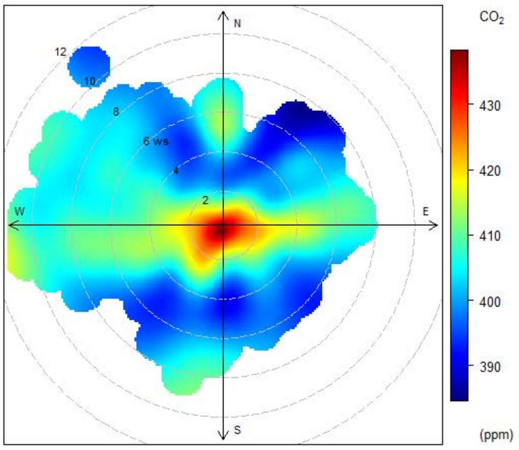

Figure 5.16: The polar plot of the CO_2 data measured from February 2018 to January 2019. The wind speed values are marked as the dashed lines in the plots.

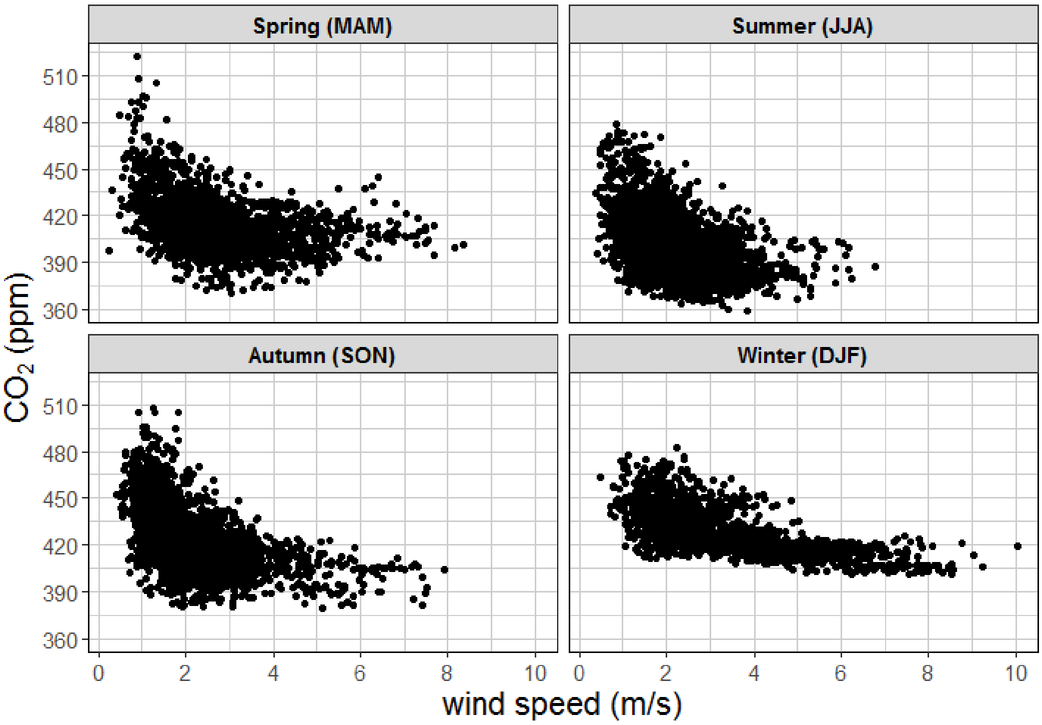

Figure 5.17: CO_2 concentration versus wind speed for different seasons

air at downtown. However, high wind speed sometimes on contrary results in a high concentration since the air recirculates in the streets or between the high buildings. It is the so-called street canyon effect [134, 135]. As shown in Figure 5.16, the wind from the west with more than 8 m/s elevates the CO_2 concentration.

Separating the plot into each season, CO_2 concentration versus wind speeds are shown in Figure 5.16. It is clear that the CO_2 concentration variability is the highest when the wind speeds are low, and the variability becomes smaller or less variable at high wind speeds. In different seasons, winter has the highest concentrations and the most occasions that the wind blows at fast (speed more than 6 m/s and even up to 10 m/s). High wind speed always results in low gas concentration in winter. On the other side, wind speeds of more than 6 m/s sometimes lead to elevate the CO_2 concentration in spring, as shown in Figure 5.16. In F. Massen's study, they used the CO_2 concentration at high wind speed to determine the CO_2 background concentration [136]. However, the street canyon effect would make the method invalid. And high wind speeds may blow the polluted air from the remote cities to the measurement site. Therefore, Massen's method cannot be used to infer the background concentration in our study.

5.5.2 Analysis with wind direction

Wind direction is also a critical factor for the CO_2 concentration. The polarAnnulus function is a method to describe the pollutant gases only using the wind direction. As the plots shown below, the polar annulus method is able to support a way of imaging the time trend variations, for instance, the weekly, seasonal and hourly tendency. Unlike the polarPlot function, it is a method to consider the temporal aspects of the pollutants. The polar annulus displays the temporal trend as an annulus, rather than a circle, so that the values close to the site point can be presented in more accurately [109].

The polar annulus plot of one-year CO_2 concentration depends on the daily hour is shown in Figure 5.18. The inner ring is the data starting at the midnight (00:00) while the outer ring is the concentration ending at 23:00. It shows that the annulus has a noticeable diurnal variation, that is, the high concentration occurs mainly in the morning before about 10:00 am (inner ring). In the afternoon after 16:00, the concentration is gradually enhanced, especially when the wind blows from the south direction with degree from 90° to 270°. The air from the north part is fresher than the air from the south. The situations are similar to the diurnal cycles described in the previous Section 5.4.3. Due to the domination by VPR and PBL effects, the average CO_2 concentration decreases in the day and increase at night, and then, the peak concentrations happen in the next morning. Therefore, the dark-red annulus in the early morning is likely caused by the biogenic respiration and the shallow PBL.

In a word, the wind speed and wind direction can reveal that the wind has impacts on the CO_2 variations. For most cases, low wind speed would lead to the high pollutant concentrations while high wind speed would result in the concentration decrements.

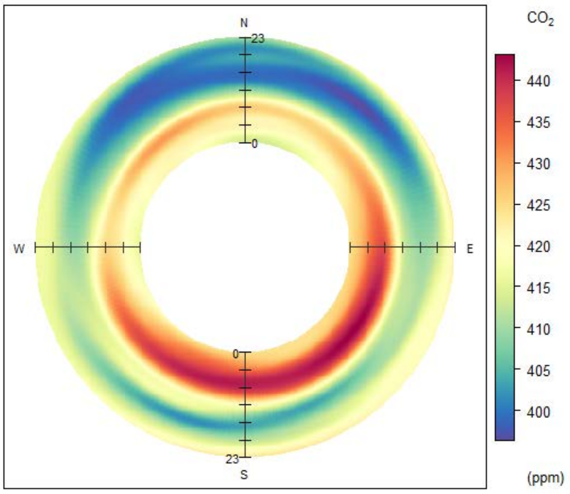

Figure 5.18: The polar annulus plot combined with the observed CO_2 in the entire study phase depends on the daily hour variables (from February 2018 to January 2019).

The highest CO_2 concentration occurs at wind speed of less than 3 m/s so that the local emissions are the primary pollutant sources in Munich in the study period. Wind direction plot helps to preliminarily determine the pollutant sources. High CO_2 concentration almost occur at the south directions in the early morning or at night. However, since the transport pathways are variable all the time before the air masses arrive at the measurement site, the wind speed and wind direction analysis cannot accurately infer the emission sources and their locations. Further model analysis, for example, simulation of the air mass transportation pathways, can be used to study the potential CO_2 emission sources in urban areas.

5.6 Conclusion

In this chapter, the continuous CO_2 concentration observations are carried out in Munich city center for a whole year. The objectives of this chapter are to learn the weekly, monthly and seasonal patterns of the CO_2 variations in urban areas and the numerous factors which can affect the variations. Some achievements have been obtained as follows:

The carbon dioxide emission inventory from the ODIAC database is utilized to study the main emission sources in Europe. The inventory map indicates that the megacities such as Paris, Brussels, and Amsterdam, are distant from Munich that their emissions have small impacts on our observed results. The local CO_2 emissions is considered as the primary sources to affect the measured results. The brief introduction of Munich is presented in the section.

The reliability of the observation has been verified by comparing with the H_2O concentration measurement at the nearby weather station. The concentrations and the linear regression between our developed sensor and the Fischer TF Sensor 401 at 2 m height a.g.l. indicate the high credibility of our observation.

The CO_2 concentration is analyzed combined with various external data, such the ambient temperature, wind speed and wind direction, PBL heights, and SIF data from OCO-2 satellite during the study period. The monthly variation patterns of the data are demonstrated. Generally, the warm months (from April to October) have higher ambient temperature, upper PBL, and stronger photosynthesis index (SIF) than the cold months.

The analysis of the CO_2 variation is based on the above meteorological and biogenic data. The discussions of CO_2 variations are based on averaging by week days, months and seasons. From the monthly analyses, we can see that the CO_2 concentration gradually decreases from spring to summer, but it increase in autumn and reaches the highest value in winter. Due to the strong effects of VPR and PBL, the diurnal variations have the distinct patterns of decreasing in the daytime and increasing at night in the warm months. While there is no obvious diurnal pattern in winter because VPR dies down and PBL become much stable. Therefore, the winter CO_2 is dominanted by the anthropogenic activities, and it is a suitable season for studying the anthropogenic activities in urban areas.

The weekly analysis shows that the averaged concentrations on Saturday and Sunday are a little lower than those on workdays. Due to the weekend breaks, there are no rush-hour traffic jams in the city center, so that the diurnal cycles have lower concentration and earlier peak values in the morning when compared to the workdays. The weekend data can be considered as compared concentrations when we want to analyze the traffic intensities or even the anthropogenic activities during the workdays. However, the diurnal cycles in the weekly plots are still dominated by VPR and PBL behaviors. It is difficult to study the anthropogenic activities when observed at only one measurement site. The case at the New Year's Eve indicates that CO_2 concentration is strongly affected by not only the human activities but also the meteorological conditions (PBL). All of the impacts should be taken into consideration for CO_2 analysis.

The relationships between CO_2 and wind speed and direction are demonstrated using the polarPot and polarAnnulus functions in the Openair package in R-statistical software. The results reveal that the high CO_2 concentration is mainly caused by the low wind speed. The VPR and PBL effects take the dominate roles in CO_2 variations. The temporal and orientation sources of the emissions can be preliminarily determined in the annulus plots.

In all, the ground-based CO_2 concentration is a result of combination effects from numerous factors, especially in the warm months when the meteorological conditions are variable and the biosphere is active. To better understand the CO_2 variations in urban areas, some simulation models are needed for further analysis. In next chapter, HySPLIT model will be displayed for simulating the air mass backward trajectories and predicting the potential CO_2 emission sources in Munich.

6 Trajectory Model Analysis

The previous chapter has demonstrated that the ground-based CO_2 concentration is a complex combination result of meteorological, biogenic, and anthropogenic activities. In this chapter, to better understand CO_2 variations in urban areas, the HySPLIT (Hybrid Single Particle Lagrangian Integrated Trajectory) model is utilized to calculate air mass backward trajectories and then to analyze the probable CO_2 emission sources in Munich.

At first, the definitions of HySPLIT model, PSCF (Potential Source Contribution Function) and CWT (Concentration Weighted Trajectory) methods will be introduced in the first two section. And then, the analyses of winter and summer CO_2 will be presented. The objectives of this chapter are as follows:

Since winter CO_2 concentration is less affected by the meteorological and biogenic activities, the winter CO_2 will be used to predict the potential carbon emission sources and to analyze the anthropogenic activities in the Munich city center.

Because meteorological and biogenic activities have great impacts on the CO_2 diurnal variations in summer, the CO_2 concentration emitted from anthropogenic activities are submerged in the strong natural effects. In order to analyze the anthropogenic activities in summer, some data sources and approaches are applied to determine CO_2 concentrations from natural factors (background concentration):

- ◇ CO_2 concentrations measured from the high mountain (Zugspitze Schneefernerhaus, ZSF)
- ◇ CO_2 concentrations measured at a rural area in a tall tower (Hohenpeißenberg, HPB)
- ◇ CO_2 concentrations measured on weekends (WKND)
- ◇ CO_2 concentrations determined from the hourly lowest concentration (HLC) method

These data sources/approaches to determine the background concentration in summertime will be introduced, and then, they will be employed in the PSCF and CWT plots to estimate the potential emission sources in Munich. The comparisons among those methods will be discussed in the last part of the chapter.

6.1 HySPLIT Model

The backward trajectory can track the air trace and supply information on the air parcel origins. The HySPLIT (Hybrid Single Particle Lagrangian Integrated Trajectory) model is one of the most widely applied atmospheric transport and dispersion models in the environmental modeling [137–142]. It helps to establish locations of emission sources from the receptor site (measurement site). Combined with the measured gas concentration at the time when the air parcel arrives at the measurement site, the air mass backward trajectories depict the air movement and gas distribution on the calculated paths.

The newest version, the HySPLIT-4 model, is a complete system for calculating the simple air particle trajectories or the complex transport, dispersion, chemical transformation, and disposition simulations. HySPLIT is developed by the National Oceanic and Atmospheric Administration (NOAA) Air Resources Laboratory (ARL). The model calculation method used in the HySPLIT model is a hybrid between the Langrangian and Eulerian approach. It employs a moving reference frame for the advection and diffusion calculation as the air parcels trajectories (Langrangian approach) and a fixed three-dimensional grid as a reference frame to compute the pollutant gas concentrations. In these two methods, the Langrangian approach is suitable when single-point source emissions restrict computation to a few grid points while the latter method is applied in the complex emission scenarios when all grid-points are required.

Over the last two decades, many updates that reflect the most current advances in the transport, dispersion and deposition computations have been comprised into the HySPLIT-4 model. The brief process of the trajectory calculation based on the HySPLIT model will be introduced as below. At first, the time interpolation of the meteorological fields is directly incorporated into the advection algorithm. Then, the three-dimensional velocity vectors V are linearly interpolated in both space and time. The particle's advection is computed from the average of the velocity vectors for the initial position $P(t)$ and the first guess position $P'(t + \Delta t)$. The relationship of the parameters is as follows:

$$P'(t + \Delta t) = P(t) + V(P, t)\Delta t, \tag{6.1}$$

where Δt is the integration time step and it can variegate in the simulation. The final position ($P(t + \Delta t)$) which is defined as the trajectory that the air parcel will follow, is given as:

$$P(t + \Delta t) = P(t) + 0.5[V(P, t) + V(P', t + \Delta t)]\Delta t, \tag{6.2}$$

The above two equations are the basic for the calculation of trajectories in HySPLIT. The calculation is affected by the advection distance, as it requires that the advection distance of every time step should be less than 0.75 of the meteorological grid spacing. Only the advection component is required in the trajectories computing. The turbulent dispersion is unnecessary in this process because it is always applied in depicting the atmospheric transport and mixing processes for 3D particles and puffs.

The input meteorological data is the ERA5 dataset from ECMWF (European Centre for Medium-Range Weather Forecasts) (available via: `https://www.esrl.noaa.gov/gmd/ccgg/trends/full.html`). Many of atmospheric variables are available through this dataset, such as temperatures, winds, and precipitation to soil moisture and so on. The ERA5 reanalysis provides hourly estimates of climate variables with a high horizontal resolution of 31 km on 137 vertical levels from the surface up to 80 km. This dataset can be obtained from the ECMWF and converted into the ARL format, which is the required format for the input files so that they can be used in HySPLIT.

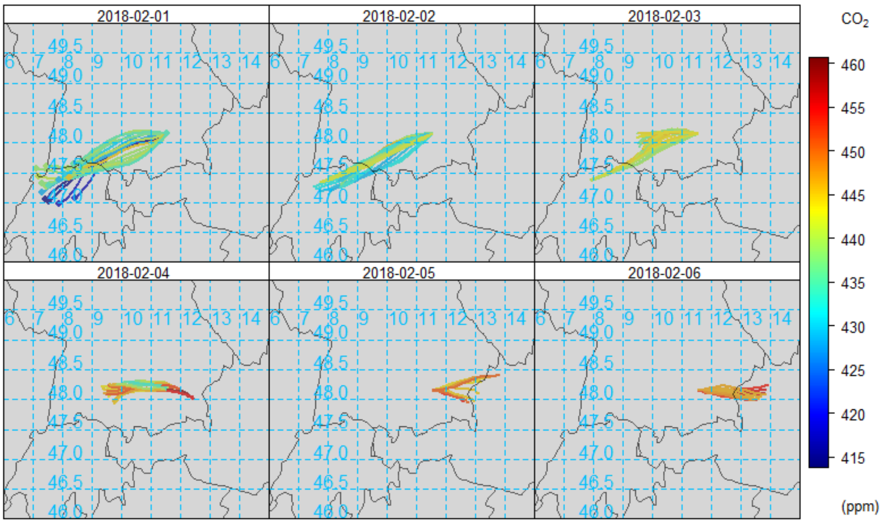

Figure 6.1: Twelve-hour backward air trajectories combined with the measured CO_2 concentration from 1st to 6th February 2018.

In the study, the backward trajectory calculations are processed in the cluster system at the Leibniz Supercomputing Center (Leibniz-Rechenzentrum, LRZ). Twelve-hour backward trajectories ending at the measurement site (receptor) (48.151° N, 11.568° E) with 100 m above ground level (a.g.l.) are calculated in hourly resolution for arrival time during the entire study period. We also calculated the trajectories at different arrival heights (50, 150, 200, 300, 400, 500 m a.g.l.) and find that the transport pathways under 300 m a.g.l. are quite similar. As examples, Figure 6.1 and 6.2 show the trajectories from 1st to 6th of February 2018, which processed with the observed CO_2 concentrations, and the trajectories during the New Year's Eves in 2018 and 2019, which incorporated with the trajectory heights, respectively. The HySPLIT trajectory calculation can also provide the option to create the trajectory in a KML file, which can be read in the Google Earth or further processed in the Matlab (we do not plot the results here). Afterwards, the observed CO_2 concentrations, the wind speed and wind direction, and the calculated backward trajectories are merged and processed by the Openair package in RStudio [109]. The Openair package is a tool in the R-statistical software to statistically analyze and understand the air pollution data. It is developed by the Openair Project which is led by the Environmental Research Group at King's College London.

The twelve-hour air mass backward trajectories from 1st to 6th February 2018 combined with the observed CO_2 concentrations at the corresponding time periods are displayed in Figure 6.1. The trajectories are demonstrated hourly and separated in every day. The convergence points of the trajectories in the maps are the measurement site. And the color bar indicates the concentration ranges as indicated in the trajectory maps. From the maps, we can see that the long traveling trajectories cause the low concentrations. It is because the long trajectories imply that the air parcels move fast and the wind blows in a high speed. The fresh air from the remote places, especially from the rural areas, cleans the air in the city center. There are, however, some processes that the long trajectories result in high concentration. For example, in 4th February, some air parcels from the west made the concentration be about 450 ppm. Meanwhile, the short trajectories always have high concentrations since the meteorology conditions are not conducive to the air dilution and the pollutants converge inside the city center. Furthermore, we can learn that the air mass is primary from the east and west directions during these six days.

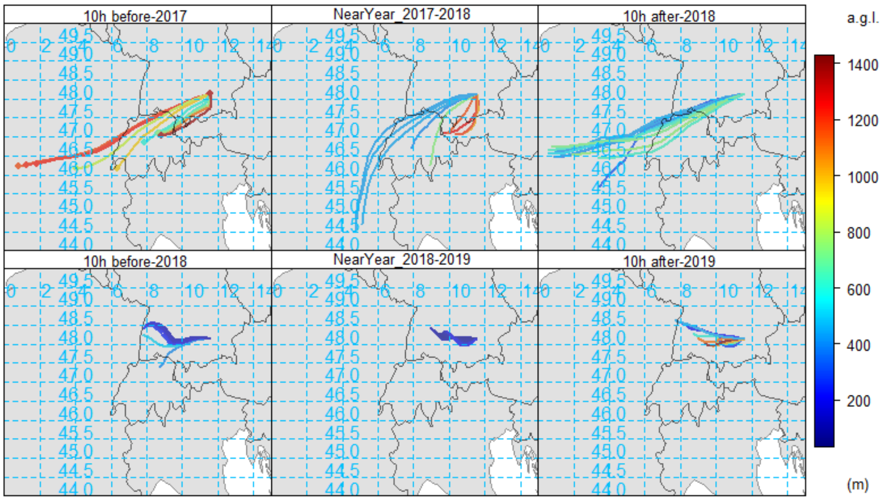

Figure 6.2: Twelve-hour HySPLIT backward trajectories of air masses reaching at the measurement during the New Year's Eve in 2018 and 2019. The three plots are the trajectories before (00:00 to 19:00 31st December), during (from 20:00 31st December to 04:00 1st January), and after the New Year's Eve (05:00-23:00 1st January). The color of the trajectories shows the respective air mass height (a.g.l., m).

The air parcel transport pathways can also be analyzed with the heights of trajectories [143]. Figure 6.2 displays the flow patterns combined with the heights of trajectories at the measurement site during the New Year's Eves of 2018 and 2019. The backwards trajectories are shown in three separated plots, which includes the event time from 20:00 31st December to 04:00 1st January (middle panel), before the Eve duration (00:00 to 19:00 31st December, left panel) and after the Eve duration (05:00-23:00 1st January, right panel). The plots indicate that the transport pathways in the New Year's Eve of

2017-2018 are much longer and higher than that of 2018-2019, suggesting that the air parcels in 2017-2018 moved faster than in 2018-2019. According to the discussion in Section 5.4.4, high wind speed in 2017-2018 mixed the air in the city and elevated the observed CO_2 concentration at the measurement site. On the other hand, the air parcels traveled at a low speed and almost hit on the ground in the New Year's Eve of 2019, as shown in the second row of Figure 6.2. The air in the city center was static and could not mix with the air at higher altitude. When the fireworks ignited, the pollutant remained in the sky and our sensor could not observe it. Therefore, the observed CO_2 concentration in 2019 New Year's Eve is higher but more stable than in 2018 New Year's Eve (Figure 5.15).

6.2 PSCF and CWT

In trajectory analysis, the clustering method provides the mean trajectories, which the similar paths are grouped together and the major air mass transport pathways which elevate the pollution concentration at the receptor can be determined. In our study, six mean-clusters are calculated from all backward trajectories by using the angle-based matrix method. Another ways to understand the origins of observed concentrations are PSCF (potential source contribution function) and CWT (concentration weighted trajectory) methods.

6.2.1 PSCF method

PSCF gives probable spatial distributions of emission sources using backward trajectories. PSCF is a conditional probability function, calculated as follows:

$$PSCF_{ij} = m_{ij}/n_{ij}, \tag{6.3}$$

where n_{ij} is the total number of trajectories that pass through the cell (i, j) and m_{ij} is the number of trajectories resulting in gas concentration that greater than a specific threshold (75th percentile of CO_2 concentration in this study). In our calculation, a further weighting factor has been considered in the PSCF value for grid cells which lack sufficient data. The PSCF plots depict the probability that the high pollutant concentrations or sources from the upwind areas result in the high measured concentrations at the downwind receptor site. The higher the probability presented on the map, the more potential source would come from the region.

The PSCF method cannot distinguish whether the gas concentration for a grid cell is only slightly higher or much higher than the threshold. The use of a higher threshold concentration can, in our experience, limit the consequences of this shortcoming and help to distinguish moderate and major sources. Moreover, this method has a good angular resolution but poor radial resolution since the trajectories converge to its receptor. Therefore, the trajectory length should not be too long. For the Munich case, we use the six-hour backward trajectories for computing the PSCF values [144–148].

6.2.2 CWT method

CWT, also called concentration-field (CF), computes concentration fields to identify the pollutant source areas. In the CWT calculation, the mean concentration ($\overline{C_{ij}}$) of a grid cell (i, j) is determined by using the following averaging formula:

$$\ln(\overline{C_{ij}}) = \frac{1}{\sum_{k=1}^{N} \tau_{ijk}} \sum_{k=1}^{N} \ln(c_k)\tau_{ijk}, \tag{6.4}$$

where k is the index of the trajectory, N is the total number of trajectories, c_k is the gas concentration measured upon the arrival of trajectory k at the receptor, and τ_{ijk} is the residence time of trajectory k in grid cell (i, j). The computed concentrations are then assigned to all grid cells and the pollutant gas would be assumed to come from the "hot spots". In the same plot, the high $\overline{C_{ij}}$ indicates that the air going across the cell (i, j) would lead to high concentration at the measurement site [149–154].

6.3 Analysis of Winter Data

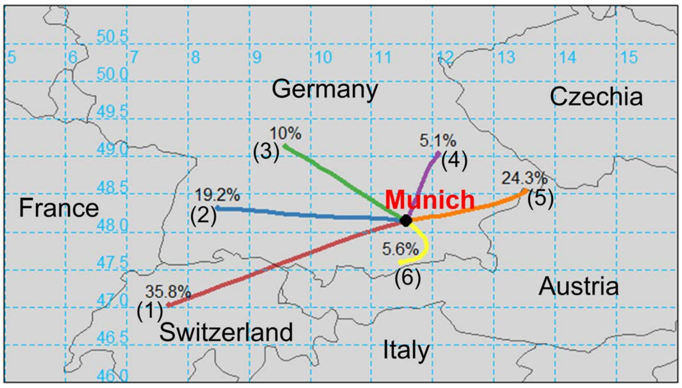

Figure 6.3: Clustering of the wintertime (February and December 2018, and January 2019) trajectories arriving at the measurement site.

In urban areas, the air pollution is related to the emission sources as well as the atmospheric dispersion and transport conditions. As the discussions in the previous chapter, the ground-based CO_2 concentration is sensitive to PBL heights and VPR activities in the warm months. While in the winter months, VPR dies down and PBL becomes relatively stable with small variations (as shown in Figure 5.8), the CO_2 concentration in urban areas is closely linked to the anthropogenic activities. Therefore, the wintertime (DJF) is a good period for analyzing the anthropogenic activities. The 12-hour backward trajectories ending at the measurement site (receptor) (48.151° N, 11.568° E) with 100 m a.g.l. are calculated and presented in this section.

The six transport path clusters calculated from the clustering algorithm and the 12-h backward trajectories are displayed in Figure 6.3. All of the backward trajectories are

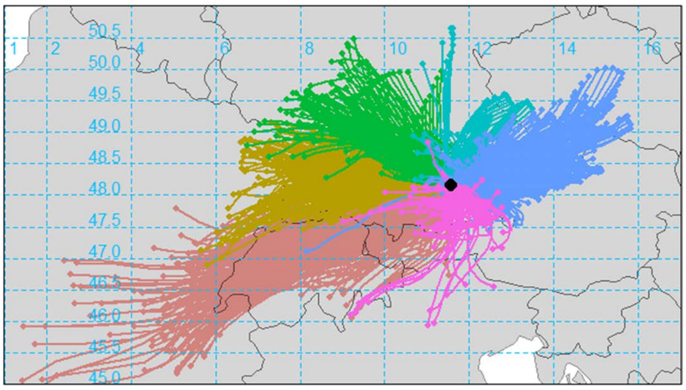

Figure 6.4: All backward trajectories in winter, which have been grouped by the clusters.

presented in Figure 6.4 according to the cluster calculation. It can be seen that the air parcels arrived at the measurement site are mainly from the east (Cluster 5 with 24.3%) and west (Cluster 1 with 35.8% and Cluster 2 with 19.2%), accounting for about 80% in total. There are little occurrences that the air masses from the north (Cluster 3 with 10% and Cluster 4 with 5.1%) and south (Cluster 6 with 5.6%) during these three months. The length of the trajectory cluster correlative with the travelling speed of the air mass. That is, the longer the trajectory cluster is, the faster the air parcels transport. Here, the trajectories from the west direction (Cluster 1 and Cluster 2) travel at the highest speed, while the trajectories in Cluster 4 and Cluster 6 move the most slowly among all the clusters, and the trajectories at other directions (Cluster 3 and Cluster 5) travel at intermediate speeds.

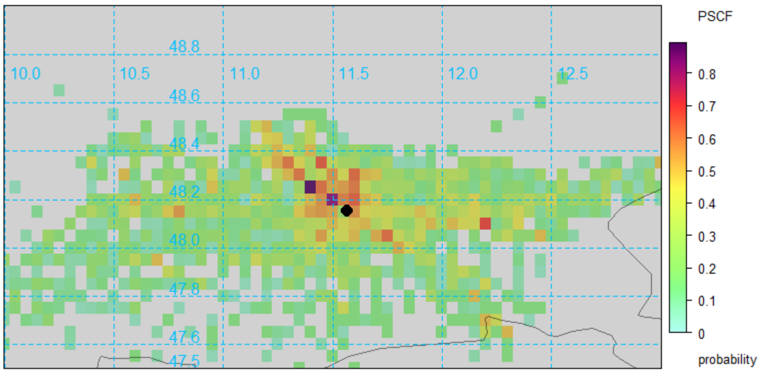

Figure 6.5: PSCF plots of CO_2 concentration measured in wintertime with 75th percentile of CO_2 and with six-hour backward trajectory (CO_2 concentration: 437 ppm).

To determine the potential emission sources in Munich, PSCF and CWT plots for CO_2 concentrations in winter are calculated from six-hour backward trajectories. The trajectories are sampled on $0.05° \times 0.05°$ grid cells and the resulting PSCF and CWT plots are shown in Figures 6.5 and 6.6, where the black circle in the map is the position

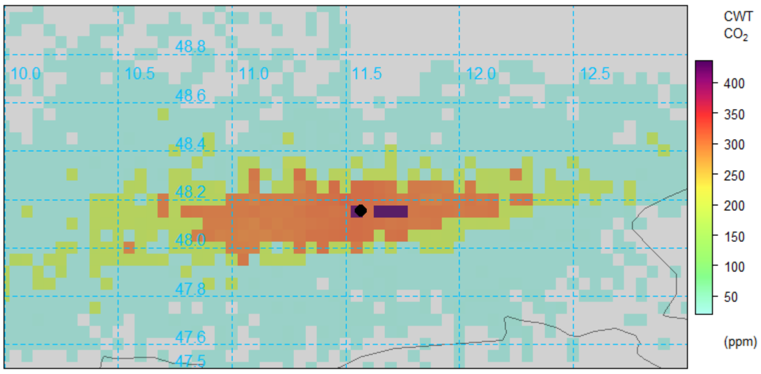

Figure 6.6: CWT plots of CO_2 concentration measured in wintertime with six-hour backward trajectory.

of the measurement site, respectively. The cells are colored according to the calculated PSCF probabilities and weighted concentrations, with the dark-red parts illustrating a high probability of the source locations and strong emission sources affecting at the measurement site. Figure 6.5 displays the PSCF result using the 75th percentile of all the concentration as the criterion. The map indicates that the CO_2 emissions are highly probable around the measurement site, especially from north (northwest and northeast) and southeast. The north direction (northwest and northeast) has the highest probability of air pollutant emission and corresponds to the trajectory Cluster 3 and Cluster 4 in Fig. 6.3. The air parcels in Cluster 3 may be polluted by the emission from manufacturing factories. The air parcels in Cluster 4 move at low speed, so that the pollutant prones to be accumulated inside the city, leading to high concentration at the receptor. Similar to Cluster 4, the wind from the southeast (Cluster 6) also travels slowly, such that high concentrations can arrive from this direction. All in all, air parcels from these directions will elevate CO_2 concentrations at the measurement site. On contrary, the west direction has the lowest probability of air pollution. Taking the trajectory clusters into consideration, the clusters in this orientation (Cluster 1 and 2) have long transport paths (air travels at high speed). The fresh air from rural areas cleans the polluted air in the city center. Moreover, the Cluster 1 goes across the Alps, indicating fresh air being transported from high altitude regions. Therefore, the air from these directions will not increase the CO_2 concentration at the measurement site.

The CWT plot of the wintertime measurement is exhibited in Figure 6.6 with the same longitude and latitude ranges as the PSCF plot in Figure 6.5. From the CWT map, we can learn that high trajectory weighted concentrations are mostly found near the measurement site, indicating that the local emissions are the main pollutant in Munich. However, the CWT mapping results are not really fully consistent with the PSCF plot. As shown in Figure 6.6, high weighted concentration areas are mainly distributed on the east and west of the measurement site. The corresponding trajectory clusters on these directions are the Cluster 1, Cluster 2 and Cluster 5, respectively, which are not the same as for the PSCF plot. The reason for the phenomenon may be understood

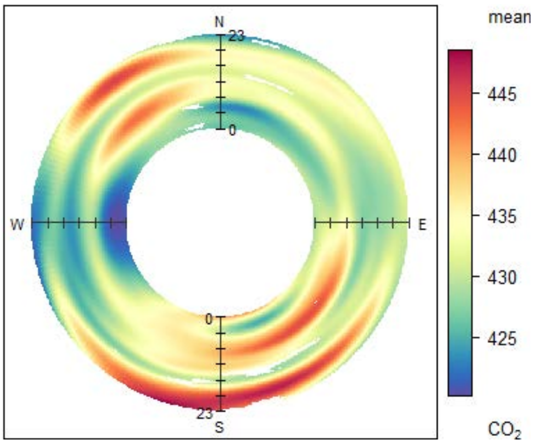

Figure 6.7: Analysis of the observed CO_2 concentration with wind direction according to the daily hours (in ten-minute interval).

by taking into account the basic of the PSCF and CWT methods (Eqs. 6.3 and 6.4). As expressed in the formulas, a PSCF contribution in a grid cell is accounted for when the gas concentration is greater than a specific threshold concentration (e.g. 75th percentile of all CO_2 concentrations). The high probability (> 0.7) in the northwest in Figure 6.5 reflects that the air parcels from this direction are always correspond to high concentrations which exceed the criterion, while the Cluster 3 in this direction contains only 10% of the trajectories as shown in Figure 6.3. The CWT method is an algorithm reflecting all of the observed concentrations, not only the high concentrations but also the low ones. All the air parcel trajectories going through a grid cell will contribute to the total CWT concentration in the cell. When the trajectories in one direction constitute a huge proportion by number and not by concentration, the computed weighted concentration in this direction can still become large in the integration process. Therefore, due to the air parcels often coming from the west (Cluster 1 and Cluster 2 with 55%) and east (Cluster 5 with approximately 24%) directions, the computed weighted concentrations of these two directions become huge. Liu et al. calculated the PSCF and CWT maps with uneven distributed trajectories and obtained the consistent results [147]. It is because the pollutant emission sources located in the directions with highly frequent trajectories in their study. As an example, a large and heavy industrial area was at the west of the measurement site with trajectories accounting for more than 40%. Moreover, the polar annulus of the observed CO_2 concentration and the wind directions in wintertime are shown in Figure 6.7. It can be found that the high CO_2 concentration mainly occurs on the northwest and south, which has better consistent with the PSCF plot when compared to CWT. The annulus plot indicates that the high concentration is caused at the time of by rush-hour, implying the anthropogenic activities dominate in winter.

Combined the trajectory cluster, PSCF and CWT methods, and polar annulus with the wind direction, we can learn that the pollutant emission sources mainly lie around the city center, especially from the southeast and north directions. The industrial factories in the north region very likely are an emission source relevant to the measurement site. Low wind speed, e.g. from the southeast, may result in high CO_2 concentration measured at our site. Compared to CWT, the PSCF method is more useful in predicting strong emission sources, since it uses a high observed concentration as calculation criterion. The CWT method can forecast that local emissions are the primary pollutant sources. However, merely the high frequency of trajectories from the east and west will lead to "exaggerated" concentrations in these directions. Therefore, the CWT method should only carefully be used for predicting emission sources when the trajectories are unevenly distributed. If the emission sources are inconsistent with the highly frequent trajectories, the CWT will yield an incorrect prediction result.

6.4 Background Concentration

As the discussions in Chapter 5, the natural factors, such as VPR and PBL heights have great impact on CO_2 concentration diurnal variations in summer. To better understand the anthropogenic activities in this season, the eliminations of the background CO_2 concentration and the VPR effects are significant. In this section, some data sources are imported as the background concentration for studying anthropogenic carbon emission in urban areas.

6.4.1 Measurement data from ZSF

The high mountain measurements are the good choices to observe the background atmospheric concentration because the high elevations are less affected by the local or regional emissions. As Figure 1.1 shown in the Introduction, the measurement at Mauna Loa, Hawaii is the longest continuous detection starting from 1958. A measurement station, namely the Environmental Research Station Schneefernerhaus (ZSF, 47.417° N, 10.973° E), is part of the Global Atmosphere Watch (GAW) program in Germany. It is situated at an altitude of 2656 m a.s.l. (above sea level) at near summit of the Mount Zugspitze which is the highest mountain in Germany and located about 90 km southwest of Munich. The ZSF station is most of the time above the PBL and thus exposed to free and presumably clean lower tropospheric air masses [155, 156].

The CO_2 data measured at ZSF is recorded with a cavity ring down spectrometer (CRDS, Picarro EnviroSense 3000i). The calibration process for the CRDS is carried out every 12 hours with three different standard concentrations. And the measurement is rechecked every 2 months according to the station reference standards [132, 143, 148, 156]. In the study, the data measured at ZSF is served as the clean atmospheric air mass concentration. The ZSF CO_2 concentration measured in 2018 is shown in Figure 6.8. We can see that the curves in every month are much flatter than that measured at ground-based (Figure 5.13). The diurnal cycles are stable at above 400 ppm with less than 7 ppm variations among all months. Only small diurnal variations are visible in the warm months from April to September.

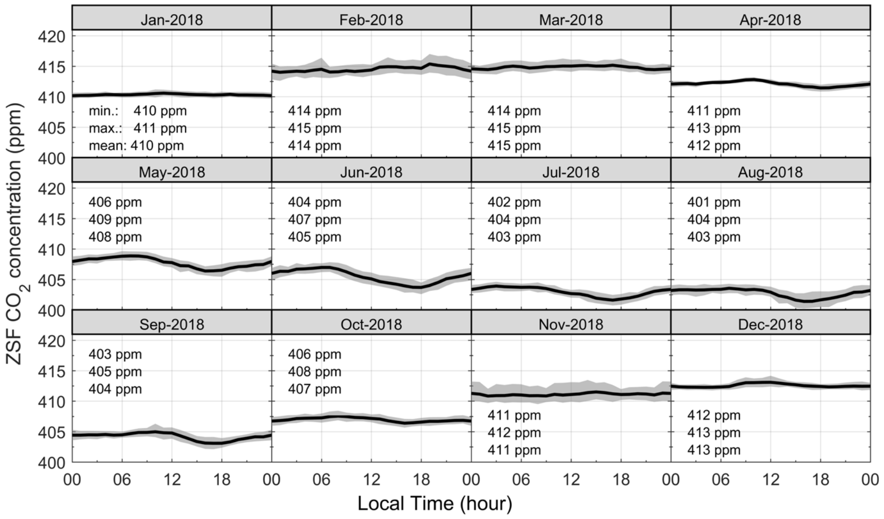

Figure 6.8: CO_2 concentration measured at ZSF station and averaged over every month (from January to December in 2018). The gray parts denote the 95% confidence intervals of the mean.

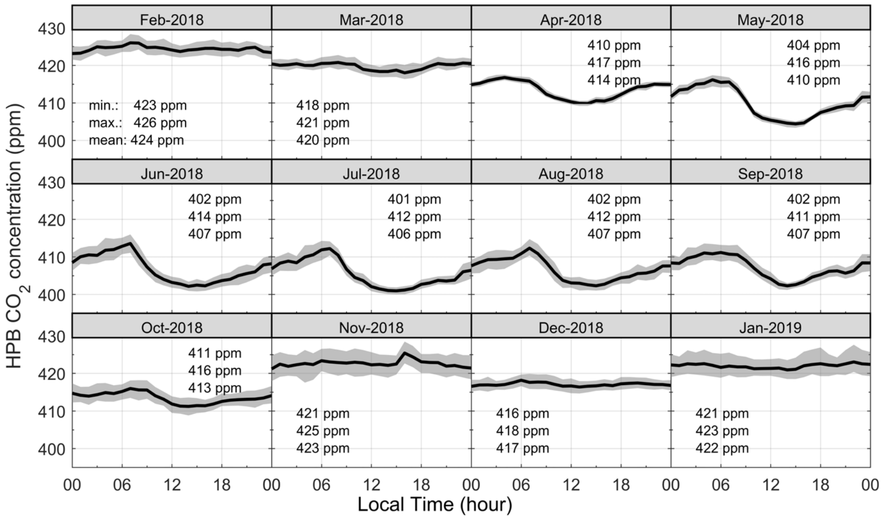

Figure 6.9: CO_2 concentration measured at HPB station and averaged over every month (from February 2018 to January 2019). The data before May 2018 is the official release data. Since June 2018, the data is obtained from the NRT release. The gray parts denote their 95% confidence intervals of the mean.

6.4.2 Measurement data from HPB

The tall tower measurement at the Hohenpeißenberg (HPB, 47.8011° N, 11.0246° E) is served as the rural area detection. The measurement site is set at 50 m height level at a tall tower at HPB (the altitude is 934 m a.s.l.). HPB is located in the northern foothills of the Alps and approximately 60 km southwest of Munich. There are two different data streams: one is the ICOS (Integrated Carbon Observation System) official release and the other is the Near Real Time (NRT) release. The official release data goes until the end of May 2018. The NRT data comes out only one day delay of the real time. The measurements are implemented continuously with one-hour interval. The detection sensor is the cavity ring down spectrometer (CRDS, instrument Id 382) in the ICOS Data system. At least three standard gases are used in the calibration process [43, 44]. The CO_2 concentration during the study period is illustrated in Figure 6.9, as well as the mean, minimum and maximum values in each month.

From Figure 6.9, we can see that CO_2 concentrations at HPB have more distinct diurnal, monthly and seasonal patterns than the data observed at ZSF. The CO_2 curves are nearly constant in the wintertime, but have obvious diurnal cycles in the warm months from April to October. In these months, the concentrations reduce in the daytime after about 8 o'clock in the morning, and increase at around 15 o'clock in the afternoon. However, the amplitudes of the diurnal cycles are much smaller than the CO_2 concentration observed at the ground-based as shown in Figure 5.11. For example, in July, the peak to peak value in Figure 5.11 is about 52 ppm, while the value in July of HPB is only 11 ppm. Moreover, the lowest CO_2 concentrations in HPB are still higher than 400 ppm, which approximates to the atmospheric concentration (Figure 1.1). The diurnal variations are more likely caused by the mixed layer increasing. During the daytime especially in the warm months, the PBL is more than 1000 m that the HPB measurement site is below the mixed layer, thus the enhancement of the photosynthesis in the low altitude would reduce the concentration at the HPB station. As a result, the HPB data will be periodically influenced by the local or regional emissions from lower altitudes.

6.5 Analysis of Summer Data

As the descriptions of the ZSF and HPB CO_2 data, because the high mountain and tall town measurement sites are not below the PBL all day long and the VPR activities are always running in the low altitudes, the diurnal variations on these two data sources are not as large as our CO_2 measurement results. These two data sources would not extract all of the VPR and PBL effects from the ground-based measurement results when the ground-based CO_2 concentration is subtracted by these two kinds of CO_2 data sources.

In this section, we propose two methods to estimate the CO_2 background concentration at the ground-based according to the weekly and diurnal patterns of the CO_2 variations. The ground-based CO_2 background concentration in this section is defined as the concentration at ground-based only without the anthropogenic activities. That is, the background concentration variations at a site caused by the effects including the biogenic activities and the PBL height varies, which is not the same as the concentrations observed at the high mountains or tall towers. For example, in the wintertime, the ground-based CO_2 background concentration would be flat because of the absence of VPR and little changes of PBL height. In summer, the CO_2 background concentration should have distinct diurnal cycles due to the active VPR activities and dramatic changes in PBL heights.

6.5.1 Weekend data as background (WKND)

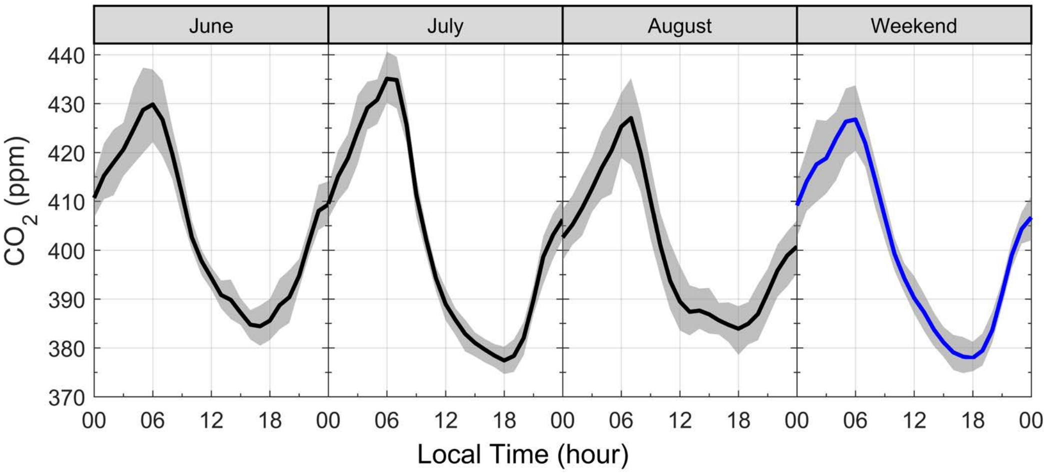

Figure 6.10: The workday and weekend CO_2 data in the summertime 2018 with 95% confidence intervals, the workdays' data are separated monthly.

In the summertime (JJA) of 2018, there are 27 days for weekends or holidays, and 65 workdays. The CO_2 data in the workdays and weekends are picked out for computing their mean diurnal cycles. The results are plotted in Figure 6.10, where the workdays' data are displayed in every month. From the graphs, we can learn that the weekend curve (the blue line in Figure 6.10) has an earlier peak concentration in the morning than the workdays, which is similar to the description in Section 5.4.3. The weekend data has smaller peak concentration in the morning than that in June and July. However, the amplitude of the workdays in August is narrower than the other month. Meanwhile, the peak concentration in August at around 6 am is as low as the curve during the weekends. It is likely due to the Bavarian vacation time (long school holidays) in Munich. During this period, not only the students do not go to school, but a lot of people are away from work and enjoy their vacations. Since most Bavarian families are on their long summer vacations in August, some companies even have the so-called "Werksferien" or "factory holidays" during this month. Therefore, there is less rush-hour traffic in the workday mornings in Munich and the CO_2 concentration is similar to weekends.

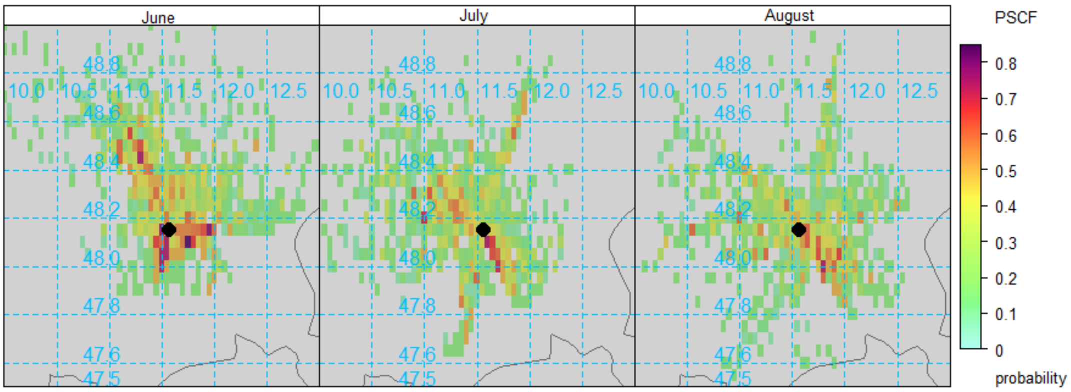

Figure 6.11: PSCF plots of summer workday data in 2018 with 75th percentile and six-hour backward trajectories.

The 12-hour backward trajectories in workdays of summer are computed with a constant height of 100 m. The PSCF plots of each month are presented in Figures 6.11. The PSCF maps indicate that the potential emission sources are mainly from the local areas. The PSCF in June has the highest probability among the summer months, and the sources are mostly from the south and east parts. In July, the probable emission source is addressed at the northwest and southeast of the measurement site. Meanwhile, the PSCF probability in August is the lowest, the red parts in the southeast of the measurement site illustrates that the emission is probably located at the south of the site which is the city center (Figure 5.2).

However, the CO_2 concentration difference between the workdays/holidays and weekdays can only represent a small part of human carbon emissions in urban areas. The huge proportions are the daily carbon consumption, such as emissions from landfill, road traffic, and electricity and energy productions. Using the concentrations in weekends/holidays to subtract the workday concentrations cannot completely separate the anthropogenic activities from the VPR and PBL effects.

6.5.2 Hourly lowest concentration as background (HLC)

In this section, the hourly lowest concentration (HLC) method is proposed to determine the background concentration in summer and winter. In HLC, the lowest concentrations in corresponding hours are treated as the background concentration. That is, taking the winter data as the example, the everyday concentration is assigned into 24 hours, each hour data of the period is set in the same group (90 values every group in winter 2018), then, the lowest concentration in each group is served as the hourly background concentration. This method intends to infer the CO_2 concentrations from the vegetation photosynthesis and respiration, as well as the CO_2 increment and decrement due to the meteorological condition variations. Among the process, the meteorological conditions are concerned as follows:

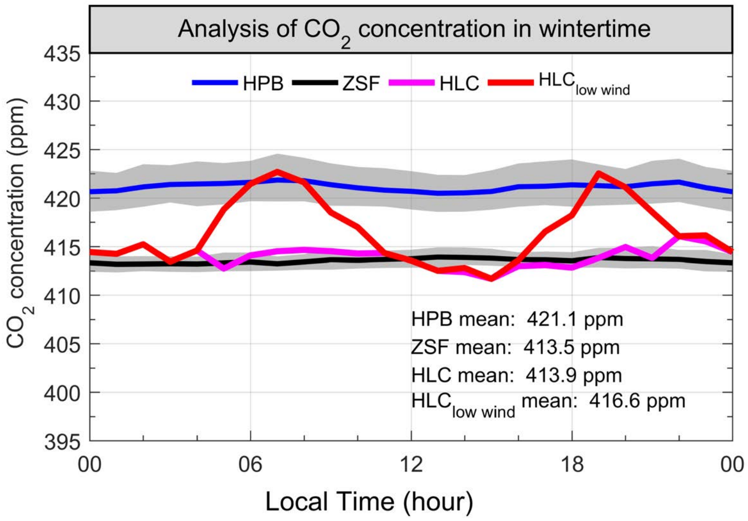

Figure 6.12: Winter background concentration analysis using the HLC method and comparing with the data measured at HPB and ZSF stations.

- ◇ **PBL height:** given that the PBL has great impact on the atmospheric CO_2 concentration and the mean PBL is pretty low at summer night (only around 100 m) and the entire day in winter, the PBL is set as below the mean values. However, The PBL in summer daytime is quite high that this setting condition will not affect much for the summer daytime.
- ◇ **Precipitation:** since the rain cleans the air while the heavy cloud leads to the shallow PBL, only the data without rainfall is considered.
- ◇ **Temperature:** the concentration at the highest temperature is ignored because the high temperature always results in the high PBL.
- ◇ **Wind speed:** high wind speed brings the clean air from the rural areas or the high altitude, although sometimes the street canyon effect increases the concentration. The processes of the winter CO_2 data with and without considering the wind speed factor (wind speed less than 3 m/s) are demonstrated in Figure 6.12.

The winter CO_2 concentrations are employed to compute the background concentrations using the HLC method. The concentrations are averaged hourly and analyzed combined with the meteorological data (PBL, rainfall, ambient temperature and wind speed). The computation results are plotted together with the CO_2 concentrations obtained from the HPB and ZSF stations. As can be seen from the curves in Figure 6.12, when the computation process has no wind speed limitation, the calculated

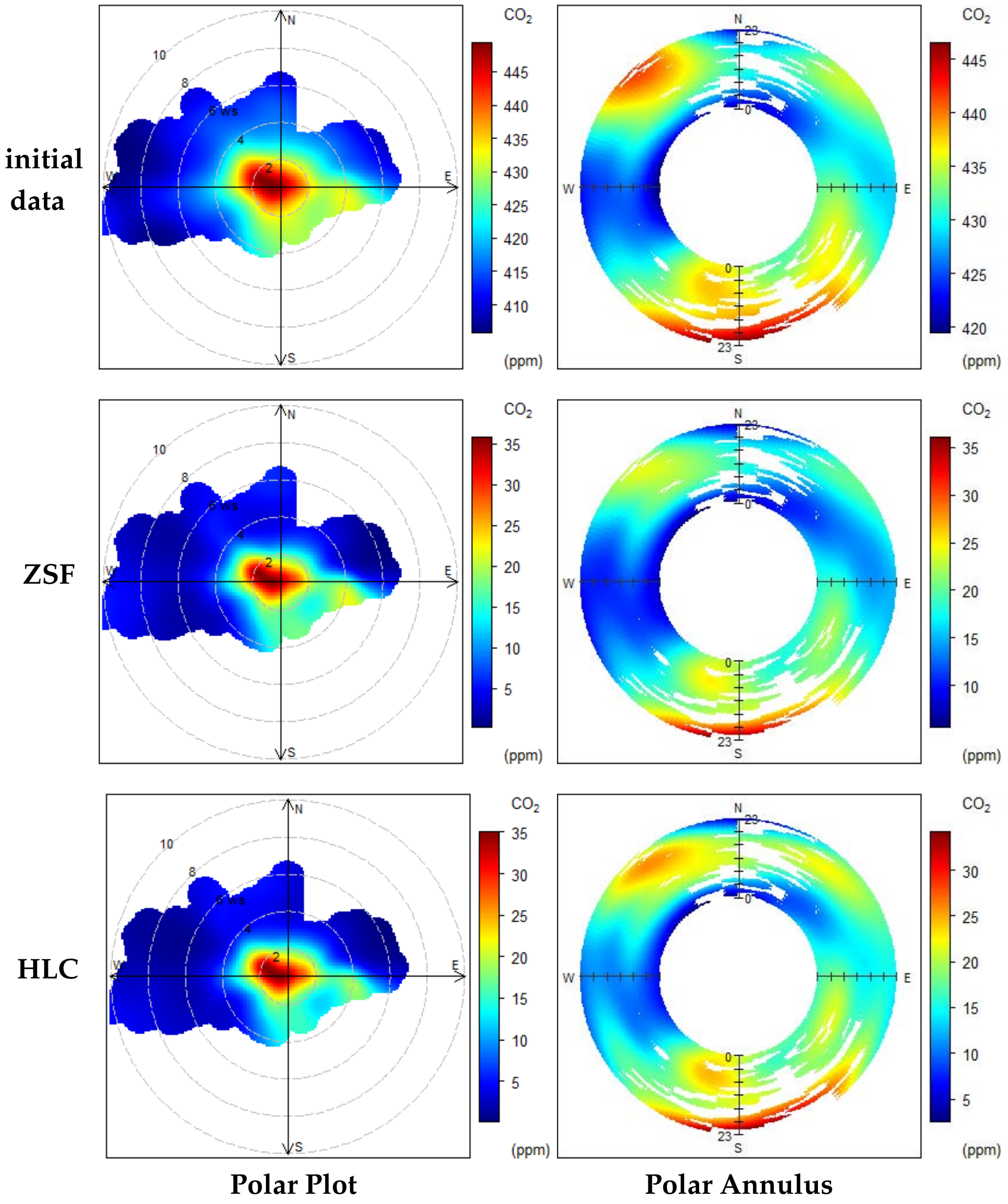

Figure 6.13: Polar plots and polar annuluses of the winter CO_2 concentrations (in one-hour interval), the second and third rows are subtracted by the background concentrations from the ZSF station and HLC method.

background concentration is approximately equal to the curve observed from the ZSF. It implies that the HLC concentration is approximately equal to the CO_2 concentration of the clean atmospheric air at a high altitude. In winter, the high wind speed would bring the fresh air from the remote place and blow away the pollutant in the city center. During 12:00 to 14:00, the HLC concentration is slightly lower than the ZSF curve; the reduction might be caused by the raise of PBL (Figure 5.8). However, when the wind speed is limited at less than 3 m/s, the HLC background concentration is captured as the red line in Figure 6.12. Similar to the original winter data, there are two peak concentrations occur in the morning and afternoon which corresponding to the rush-hour traffic. The results reveal that when the air in city center is almost static, the HLC concentration will also be affected by the anthropogenic emissions in the city center. The results indicate that high wind speed can bring the fresh air from remote places even from the high altitudes; on the other hand, the pollutant gases in the urban areas cannot be cleared away under low wind speed. In the HLC method, we will not make limitations on the wind speed.

Meanwhile, the polar plots and polar annuluses of the initial winter CO_2 concentration, and the CO_2 concentrations which have been subtracted by the concentration obtained from ZSF measurements and HLC method are demonstrated in Figure 6.13. The red parts in the figures are shown the similar results among the three methods. In the polar plots, we can learn that the high CO_2 concentrations are caused by the low wind speed or the air from the southeast direction. In the polar annuluses, it is clear that in the morning, the pollutant is mainly from the south, while from afternoon to midnight, the high CO_2 concentrations are primarily from the south, northwest, and northeast. According to the aforementioned discussion, the winter background CO_2 concentration determined by the HLC method is similar to the data measured at ZSF, therefore, the concentrations eliminated by the ZSF and HLC can obtain the same results. In the follows, we will analyze the summer data using the HLC method, and make comparisons among the ZSF, HPB, and WKND approaches using the different mapping methods. As the results discussed above, the limitations of meteorological conditions to determine the HLC concentration are summarized as:

- ◇ Below the mean PBL height;
- ◇ No precipitation;
- ◇ Ignore the highest temperature;
- ◇ No wind speed limitation.

6.5.3 Analysis of data in July 2018

In this section, the proposed HLC method will be used to infer the background concentration from the observed CO_2 concentration in July 2018, the results will be compared with the other methods as mentioned above, including: ZSF, HPB, and WKND. The six transport path clusters based on the 12-hour backward trajectories in July 2018 is shown in Figure 6.14. Due to the barrier of the Alps, the air parcels arrived at the measurement site are mainly from the north part, from approximately -90° to 90°. Similar to the wintertime episode, the trajectories in July 2018 are mainly from the west (Cluster 1: 20% and Cluster 2: 24.3%) and east (Cluster 5: 22.4%) directions with the fastest moving speed. Some air parcels are from the north (Cluster 3 and Cluster 4) with slower traveling speed. The Cluster 6 (6.9%) is the only trajectory coming from the south and traveling slowest.

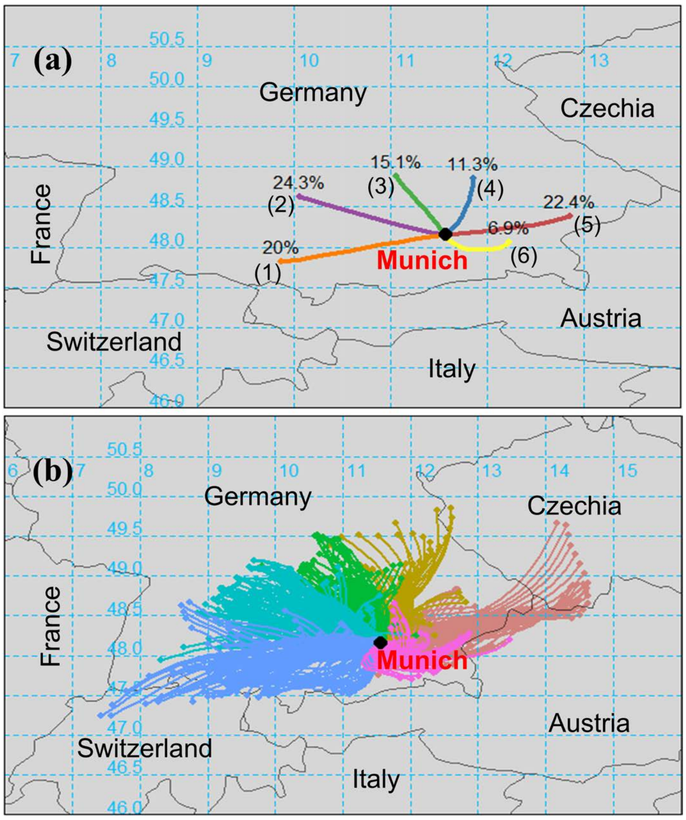

Figure 6.14: (a) Six cluster-mean backward trajectories arrive at the measurement site (July 2018). (b) All trajectories which have been grouped in the six clusters.

The determination of the July background concentration based on the HLC method is shown as the blue line in the middle of Figure 6.15. The initial July concentration is shown in the first panel and the corrected CO_2 concentration when the initial minus the background concentration is displayed in the third panel. The blue curve in the middle panel is the HLC calculated result. The curve has the maximum and minimum concentrations at about 6:00 and 18:00, respectively, with the peak-to-peak value of around 50 ppm.

The corrected concentrations in July are analyzed combining with the six-hour backward trajectories and the wind speed and direction. The mappings using the polar plot, polar annulus, PSCF, and CWT methods are exhibited in Figure 6.16. For comparisons,

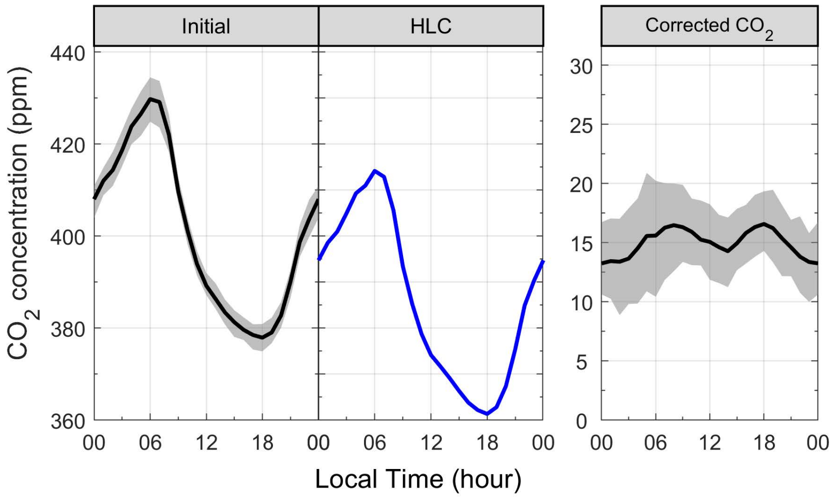

Figure 6.15: The analysis of July 2018 CO_2 concentration based on the HLC method, the first figure is the monthly averaged curve of July data, the second is the background concentration determined by the HLC method, the third figure is the CO_2 concentration when the background concentration is eliminated (the first figure minus the second one).

the initial July CO_2 concentration and the concentrations which have been corrected by different backgrounds (ZSF, HPB, WKND, and HLC) are demonstrated in the subplots. The plots in the first row are the analyses on the initial CO_2 concentration. As presented in the polar annulus, the high concentration occurs in the early morning which is similar to the description in previous chapter (Section 5.4 and Section 5.5). Thus, we can conclude that the high concentrations or the high probability of emission sources in the polar plot, polar annulus, PSCF, and CWT mappings of the initial data are dominated by the VPR and PBL effects. The situations in the second and third rows are the same, suggesting that the CO_2 concentrations obtained from ZSF and HPB stations cannot help to eliminate the VPR and PBL effects from the observed CO_2 concentrations.

When subtracted by the WKND concentration, a part of the anthropogenic emission CO_2 concentration can be achieved. The polar plot in the fourth row shows that the high concentration not only occurs at low wind speed, but also happens at some cases from the northwest and south with wind speed higher than 3 m/s. In the polar annulus, some of the highest concentrations are located in the north at 8:00 am. Meanwhile, some bright yellow annuluses can also slightly be found during the daytime. Unlike the PSCF plots in the initial data, ZSF and HPB methods that the potential emission sources are addressed at the south Munich, the PSCF plot in WKND method demonstrates that the probable emission sources are mainly from the north and southeast of Munich. This mapping result is consistent with that in wintertime (Figure 6.5).

The mapping results which use the HLC method to correct the July data are shown in the last row of Figure 6.16. The figures have the identical results with but more distinct than the WKND method. We can see that the high concentrations from the southwest and northwest are enhanced in the polar plot graph. The high wind speeds from these two directions can increase CO_2 concentration at the measurement site, indicating that some regional emissions from these directions would affect the air quality in Munich city center. In the polar annulus, the outer annulus is colored into bright yellow (approximately 20 ppm), which reveals that the anthropogenic CO_2 emission in the daytime can be highlighted in the HLC method. The PSCF plot is consistent with the CWT plot that the potential emission sources are primarily from the north and southeast directions. Compared to the analysis result of winter data, the predicting emission sources in winter and summer are the same: the main anthropogenic CO_2 emission sources are located in the north and southeast of Munich. Therefore, it can be concluded that the HLC method can effectively subtract the VPR and PBL effects in the summer data, and help to extract the anthropogenic CO_2 fraction from the strong natural factors. Using HLC, the anthropogenic activities in the warm months can be preliminarily studied.

In summary, as the strong influence from the VPR, it is hard to independently analyze the anthropogenic activities from the ground-based CO_2 concentration. The section has discussed several methods to eliminate the CO_2 concentration from the VPR and PBL effects, and finally analyze the local CO_2 emission in urban areas. The overviews of the methods are listed in Table 6.1.

Table 6.1: Comparisons of the methods to determine background concentration in summertime.

Method	Advantages	Disadvantages
ZSF	ZSF data are most of the time not affected by local or regional emissions.	ZSF data excludes the VPR and PBL effects.
HBP	Measurement in rural areas, some VPR effects can be detected.	HPB data is affected by the local emissions, and includes a small part of VPR and PBL effects in the afternoon.
WKND	Anthropogenic CO_2 concentration is obtained from the difference between weekends and workdays.	Cannot obtain the total anthropogenic CO_2 concentration.
HLC	Anthropogenic activities can be separated from VPR and PBL	Limitation conditions are hard to be determined; further models are needed to verify this method.

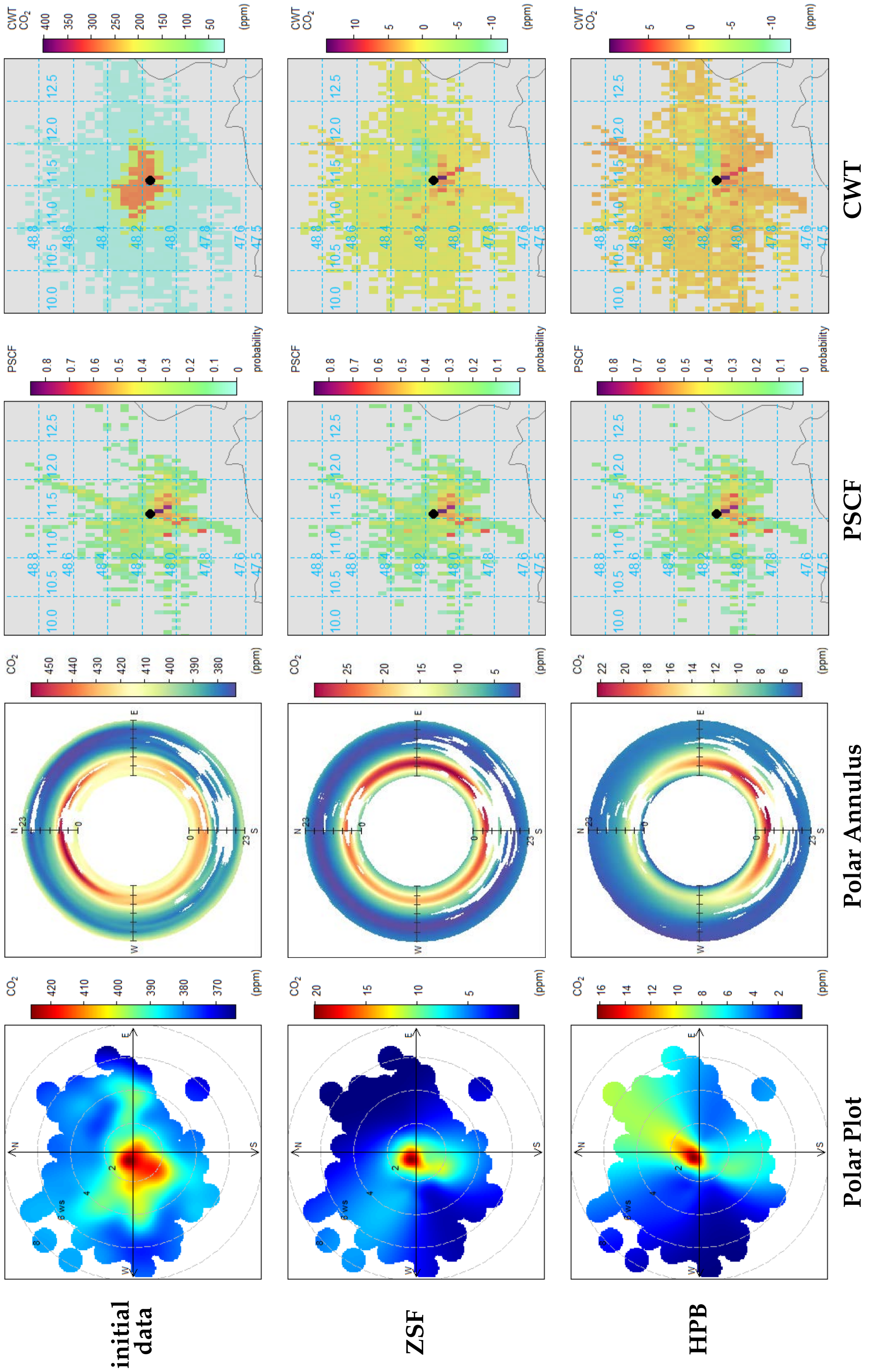
initial data
ZSF
HPB
Polar Plot
Polar Annulus
PSCF
CWT
CO_2
(ppm)
PSCF
probability
CWT CO_2
N
E
S
W
ws

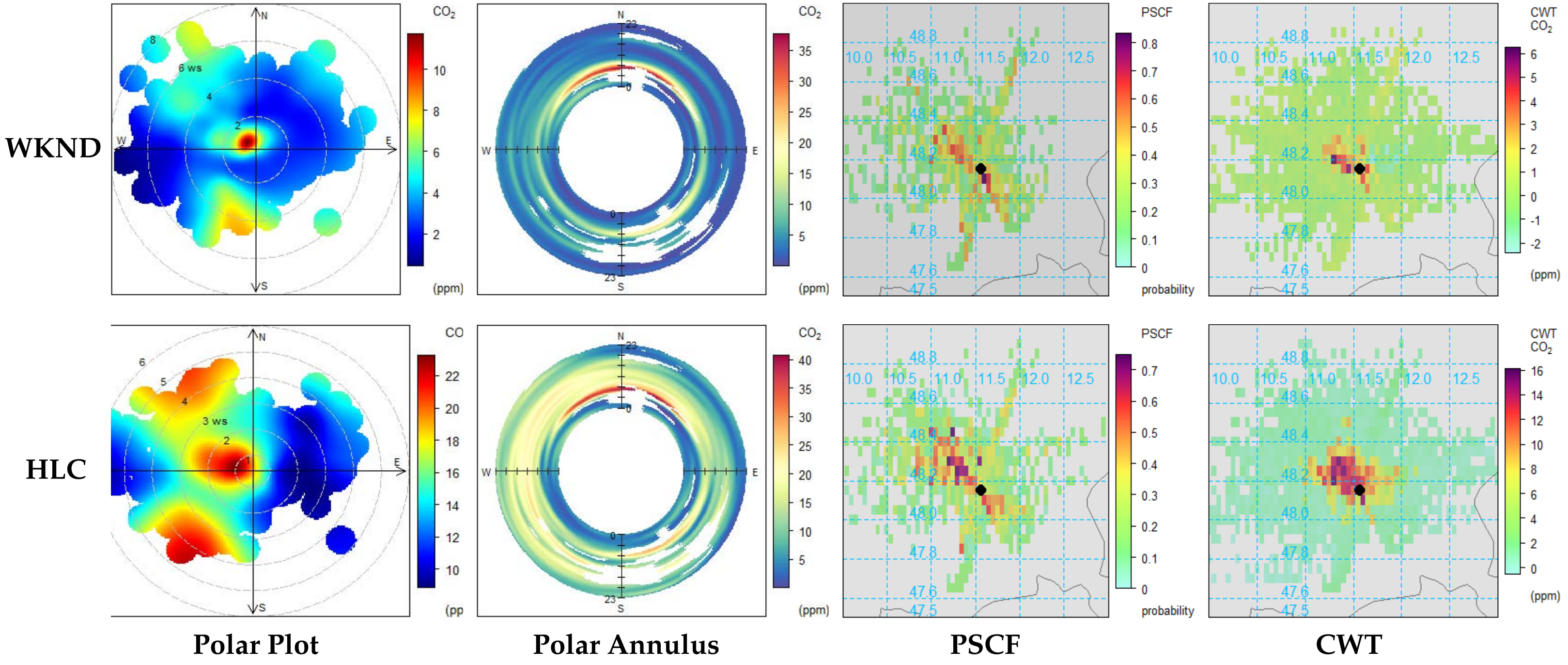

Figure 6.16: Analyses of the July data using the different mappings and different background concentrations.

Due to the above PBL location, the high mountain measurements (ZSF) have little influence from the regional or local emissions, the CO_2 concentrations observed at the ZSF station can be served as the atmospheric background concentration. However, the measurement results exclude the variations from the local or regional vegetation carbon sources and sinks, therefore, ZSF cannot be utilized to analyze the local anthropogenic activities. Similar to the high mountain measurement, the rural measurements in the tall tower (HPB) cannot be used for the urban emission analysis. Using the weekend data as the background (WKND), some of the human activities during the workdays can be extracted. Nevertheless, the daily anthropogenic activities cannot be captured in the WKND method. The hourly lowest concentration (HLC) approach can determine the natural effects at a higher accuracy, and then to study the anthropogenic activities. However, it is hard to set the meteorological limitations when determining the background concentration. Although the analysis results based on the HLC method are consistent with the WKND method, some models or simulations are needed to further verify the HLC method.

6.6 Conclusion

In this chapter, the HySPLIT model is introduced for computing the air parcel backward trajectories and studying the potential CO_2 emission sources in Munich.

Firstly, the basic theories of the HySPLIT, PSCF and CWT methods are introduced. The computation of the air parcel backward trajectory based on the HySPLIT model is operated in the supercomputer. Combined with the measured CO_2 concentration, the probable carbon emission sources in urban areas can be addressed by the PSCF and CWT methods.

The winter and summer CO_2 concentrations are studied in this chapter. Due to the absence of VPR activities and constant of meteorological conditions, the winter CO_2 concentrations are sensitive to the human activities so that the observed concentrations can be used for analyzing the anthropogenic activities in urban areas. The six-cluster backward trajectories indicate that the mainly trajectories at the measurement site are from the east and west. The PSCF mapping indicates that the main emission sources locate at the city center, especially on the north and southeast directions of the measurement site. The CWT shows that high CO_2 concentrations can be traced back to local emissions. However, the exact CWT results may be somewhat skewed by a huge proportion of trajectories from the east and west. Therefore, the PSCF method is more suitable for predicting emission sources. Combined with modeled details of air mass transportation, primary locations of pollutant emission sources can be determined.

In summer, the ground-based CO_2 concentrations measured in our system are strongly affected by the biogenic activities (VPR) and meteorological movements. Consequently, the anthropogenic activities are submerged by these factors and it is hard to learn the human carbon emissions in urban areas from the initial observed CO_2 concentrations. Four possible approaches are proposed in the study to eliminate the natural background concentrations from the observed CO_2 data: (1) the CO_2 concentration measured at high mountain station (Zugspitze, ZSF) is treated as the concentration at the free and clean troposphere; (2) the CO_2 concentration obtained from a tall town at a foothill of the Alps (Hohenpeißenberg, HPB) is served as the concentration at the rural areas; (3) the CO_2 concentration averaged from the weekend data is used as the background concentration during the workdays (WKND); (4) the proposed hourly lowest concentration (HLC) to determine the background concentration in summer.

The determination conditions of the HLC method are discussed using the winter data. the results come out that without the wind speed limitation, the HLC concentration in winter approximates to the concentration at ZSF. When eliminated by the HLC concentration, the polar plot and polar annulus results of the winter CO_2 are the same as that of the initial data and that subtracted by the ZSF data. The results reveal the validation of the HLC method.

The comparisons of the ZSF, HPB, WKDN and HLC approaches using the CO_2 concentration observed in July 2018 are illustrated in the last section. The outcomes show that the ZSF and HPB methods have similar polar plots, polar annuluses, PSCF, and CWT maps as the initial July CO_2 concentration, which reveal that the ZSF and HPB methods cannot effectively eliminate the VPR and PBL effects. On the other hand, the HLC approach has the similar mappings as but higher concentration/probabilities than the WKDN method, suggesting that the HLC method can be used for the urban CO_2 concentration analysis in the warm months.

However, the proposed HLC should be further validated using advanced models, for example, the WRF (Weather Research and Forecasting) VPRM (Vegetation Photosynthesis and Respiration Model). Moreover, we would like to mention that in the HySPLIT backward trajectory computation, the spatial resolution of the meteorological data (ERA5) which is utilized for supporting the wind field is not very high. Thus, the predictions of the emission locations are not in a high accuracy. To better understand the emission and distribution of CO_2 and other pollutant gases in cities, we suggest to build a sensor network to observe multiple gas species at different sites. Given the properties of compact, self-calibration, and precision, our developed sensor is suited for long-term pollutant sensing in urban areas.

7 Summary and Outlook

This study has developed an in-situ CO_2 concentration measurement system based on the TDLAS-WMS technique. The designed signal processing enables the system to determine the laser light intensity, normalize the harmonic signals, calibrate wavelength and infer the phase shifts and RAM signal during the concentration calculation. Using the long tuning range VCSEL and multi-harmonic detection, the measurement precision has been effectively enhanced. Therefore, the developed system have many unique properties, such as, compact, self-calibrated, high precision, high accuracy, high stability, and can simultaneously measure different gas species, and so on. The Allan Deviation method is utilized to evaluate the measurement precision. The accuracy of the system is verified by comparing with the commercial NDIR sensor. The developed system is employed for continuous measurement of CO_2 concentration in Munich for one year from February 2018 to January 2019. The seasonal, monthly, weekly and diurnal variations of ground-based CO_2 concentration have been studied. Moreover, the air parcel backward trajectories based on the HySPLIT model are imported to analyze the potential CO_2 emission sources in Munich. Due to the strong VPR and PBL effects in summer, the HLC method is proposed to separate the anthropogenic CO_2 emissions from the biogenic activities and meteorological variations. The preliminary results come out that the proposed HLC approach can be utilized to analyze the summer data, even though this approach should be further verified.

7.1 Summary

The main achievements for developing the TDLAS-WMS measurement system are listed as follows:

- ◇ The theories of TDLAS and WMS are presented in Chapter 2. The high order sinusoidal modulation intensities are taken into account in the harmonic formula derivations. The expressions of the multiple harmonics are derived under weak absorbance and absorption-free conditions. Subsequently, the relationship between the phase shift and the lock-in amplifier (LIA) reference signal phase is studied and then it is used to assign the concentration-dependent and concentration-independent signals into two axes of the LIA. Afterwards, the light intensity normalization, the RAM elimination, the wavelength calibration, and the first and multi-harmonic detections are put forward. Finally, the modulation index in the different harmonics are discussed, and the optimal modulation index for multi-harmonic detection is determined.

- ◇ A digital LIA is developed to produce the zeroth to fifth harmonics synchronously and to separate each harmonic in their own X and Y axes. The zeroth harmonic is utilized to normalize the other harmonics so that the central light intensity is eliminated from the harmonic signals. The harmonic signal captured in the procedure is the concentration-dependent signal that the measurement gets rid of the calibration process. The CO_2 and H_2O concentrations can be inferred from the acquired harmonic according to the LLSCF algorithm.

- ◇ The residual amplitude modulation (RAM) signal in the first harmonic is subtracted from the harmonic signal. The reformed first harmonic signal is then employed for the gas concentration detection. The first harmonic detection has the best noise performance among the single harmonic detections.

- ◇ The Allan Deviation is utilized to evaluate the measurement precision. The results have revealed that the multi-harmonic detection has a higher precision than the sole-harmonic detection. Multi-harmonic detection can improve the precision of about 2–3 times when compared with the traditional second harmonic detection. In terms of the detection limitation, the multi-harmonic detection with the first-to-third harmonics and up to three CO_2 absorption lines and one H_2O absorption line can obtain the highest precision of 0.02 ppm for CO_2 and 1.0 ppm for H_2O with a 10-minute integrating time. Moreover, the multi-harmonic detection which includes the first harmonic has higher precision than that excludes the first harmonic. The commercial NDIR sensor is served as a standard instrument to compare the measurement of the multi-harmonic detection. The experimental results have indicated the high accuracy of the developed system and the high consistency between these two sensors.

For the sensor applications, the continuous CO_2 concentration measurements is implemented in Munich city center for one year from February 2018 to January 2019. The additional meteorological data such as the ambient temperature, PBL heights, wind speed and direction, and the SIF data from OCO-2 satellite are used to support the analysis of the measurement results. The patterns of daily, weekly, monthly and seasonal variations are analyzed to study the carbon cycles in Munich. In the monthly analysis, the diurnal variations are distinct in the warm months. The diurnal cycles are affected by multiple factors, in which the VPR and PBL effects are dominated so that the anthropogenic activities effects are submerged in the warm months. In the wintertime, when the VPR is feeble and the PBL height becomes stable, the anthropogenic activities become pronounced. The weekly analyses exhibit that the rush-hour traffic is visible from the observed concentrations during the workdays. Special cases in the New Year's Eve of 2018 and 2019 are also discussed, and the results reveal that the ground-based CO_2 observation is sensitive to the PBL height in the wintertime.

To better understand the CO_2 emission and transportation in urban areas, the air mass backward trajectories based on the HySPLIT model are calculated during the whole study period. The trajectory clustering, PSCF and CWT methods are used to predict the probable emission sources in summer and winter. The studies of the winter CO_2 indicate that the potential carbon emissions in Munich are likely located at the north and southeast of the measurement site. Moreover, compared with the CWT, the PSCF method is superior in predicting the potential sources when the trajectories are unevenly distributed.

It is difficult to study the anthropogenic activities with only one measurement site in summer since the ground-based CO_2 concentration is strongly affected by the VPR and PBL effects. An HLC (hourly lowest concentration) method is put forward to infer the VPR and PBL effects. The determination of the background concentration in July 2018 is presented. The results are compared with the CO_2 concentrations measured at ZSF and HPB stations, and the WKND method. The results demonstrate that the proposed HLC method can determine the background concentration so that it can somewhat effectively subtract the VPR and PBL fractions from the observed CO_2 concentrations. Therefore, the HLC method can be utilized to correct the ground-based CO_2 concentration in warm months and to estimate the anthropogenic CO_2 emission sources in urban areas.

7.2 Outlook

The theory of the TDLAS-WMS, the design and performance of the measurement system, the continuous CO_2 concentration measurement results and the analysis based on different models and methods have been displayed in this study. Due to the self-calibrated characteristic, the proposed multi-harmonic detection is possible applied in measuring the other gas species, such as methane (CH_4) and carbon monoxide (CO) near the wavelengths of 1565 nm or 2365 nm. Only one measurement site and one kind of GHG are studied in the thesis, thus, it is a little difficult to analysis the carbon emissions in a higher accuracy. In the future works, a sensor network can be built and deployed for further studying the GHG and pollutants in urban areas.

Moreover, some improvements can be conducted in the future works.

- ◇ To compare the measurement results with the other sensors, such as, EM27/SUN column measurement and OCO-2 satellite remote sensing; and the other gas species, such as CO, CH_4 or nitrogen oxides (NOx) to explore the various pollutants in urban areas.
- ◇ Some other models, such as STILT (Stochastic Time-Inverted Lagrangian Transport) model [157], WRF (Weather Research and Forecasting) model [127], or CFD (Computational Fluid Dynamics) model [158–160], can be employed to simulate the air parcel backward or forward trajectories in higher spatial and temporal resolutions. These models can also be used to verify the HLC method.
- ◇ The structure of the TDLAS-WMS measurement system can be more compact and portable when the laser and photodetector drivers are combined into an electric circuit. The PCB hardware design of the system can be continued in the future.

In summary, because of the properties of compact, self-calibrated, and high precision and accuracy, the developed TDLAS-WMS multi-harmonic detection measurement system is significant for in-situ measuring the GHG and pollutant gases in industrial or research applications. The analysis models and methods of determining the potential emission sources presented in the thesis can also be utilized in the similar cases in further studies.

Acknowledgements

I sincerely thank my supervisor Prof. Dr.-Ing. Jia Chen, who offers me the opportunity to study in this wonderful research group and gives me useful supports and advice on my research. I would like to thank Ms. Pamela Ruschi, Ms. Rita von Grafenstein, Dr. Martin Jakobi, and Dr. Evelyn Wegner for their helps on my study, some even beyond their responsibilities.

I gratefully acknowledge VERTILAS GmbH for kindly providing the VCSEL laser in the TDLAS-WMS sensor and thank Dr. Christian Neumeyr and Mr. Jürgen Rosskopf for the valuable technical consultation and input. I want to thank Mr. Sheng Ye and Prof. Dr. Mark Wenig from Ludwig Maximilian University of Munich (LMU) for providing the Li-Cor 840A CO_2/H_2O gas analyzer, and Mr. Markus Garhammer (LMU) for supporting the weather data, and Dr. Stephan Hachinger from Leibniz Supercomputing Center (Leibniz-Rechenzentrum, LRZ) for helping the HYSPLIT trajectory calculation, and Ms. Homa Ghasemifard, Mr. Ye Yuan, and Prof. Dr. Annette Menzel from Professorship of Ecoclimatology for their advice on the model and data analyses. I thank Dr. Ludwig Ries from German Environment Agency (UBA) for providing the high mountain CO_2 data measured at the Zugspitze Schneefernerhaus (ZSF) station and Dr. Sabrina Arnold from Deutscher Wetterdienst (DWD) for providing the tall tower CO_2 data at the HohenPeißenBerg (HPB) Meteorological Observatory. I would like to thank Mr. Bernhard Obermaier and Mr. Rainer Bierbaum for their helps in building the experimental setup. I also want to thank my colleagues (Dr. Yingchun Wu, Ms. Yanfang Li, Mr. Yonglu Zhu, Dr. Yin Bai, Ms. Xinxu Zhao, Mr. Xiao Bi, Mr. Florian Dietrich, Dr. Shrutilipi Bhattacharjee, Dr. Min Lu, Dr. Yubo Huang, and so on) in Environmental Sensing and Modeling (ESM) and Measurement Systems and Sensor Technology (MST) groups for their useful discussions during the study. I especially thank Ms. Magdalena Altmann, a master student in my group, for her help in improving the German language in the Zusammenfassung. For the financial supports, I would like to thank the program of China Scholarships Council (CSC, 201608080018).

Finally, I heartfeltly thank my parents and my boyfriend, Dr. Rongzong Huang, for their permanent understanding and love.

Symbols

The symbols tabulated here are used throughout the work. Symbols that are only used locally (for example, for substitutions or intermediate results) are explained or defined in the respective context.

Symbol	**Unit**	**Definition**
a	[cm^{-1}]	modulation depth
atm	[Pa]	Standard atmosphere
A_k		k-th order Fourier component of the transmittance ($k \in \{0, 1, 2 \cdots\}$)
c	[m/s]	Light speed
c_G		Weights of the Gaussian profile
c_L		Weights of the Lorentzian profile
C		Gas concentration
$\overline{C_{ij}}$		Mean concentration of a grid cell (i, j)
C_{CO_2}		CO_2 concentration
C_{H_2O}		H_2O concentration
E_S	[mbar]	Saturation vapor pressure
$E_S(t_w)$	[mbar]	Saturation vapor pressure at wet-bulb temperature (t_w)
H_k		k-th order Fourier component of the spectral line shape ($k \in \{0, 1, 2 \cdots\}$)
i	[mA]	Tuning current
I_0		Incident laser light intensity
$\overline{I_0}$		Central light intensity
I_k		k-th order sinusoidal modulation intensity ($k \in \{1, 2, 3 \cdots\}$)
I_t		Transmitted laser light intensity
k_B	[m^{2}kgs^{-2}K^{-1}]	Boltzmann constant
L	[cm]	Absorbing path length
m		Modulation index
M	[g/mol]	Molar mass
Mr		Relative molecular mass
N_A	[mol^{-1}]	Avogadro constant
P	[atm]	Total gas pressure
$PSCF_{ij}$		Potential source contribution function probability of a grid cell (i, j)
R	[J/(mol·K)]	Ideal gas constant
S_{0f}		Zeroth harmonic

$\overline{S_{kf}}$		k-th harmonic normalized by the zeroth harmonic ($k \in \{1, 2, 3 \cdots\}$)
$S(T)$	[cm^{-2}/atm]	Line strength
t_D	[°C]	Dry-bulb temperature (atmospheric temperature)
t_w	[°C]	Wet-bulb temperature (humid temperature)
T	[K]	Temperature
v	[cm^{-1}]	Wavenumber
v_0	[cm^{-1}]	Center wavenumber of absorption line
$\overline{v}$	[cm^{-1}]	Central wavenumber
X_{1f}		X component of the first harmonic
X_k		k-th Fourier components of the light intensity ($k \in \{0, 1, 2 \cdots\}$)
Y_{1f}		Y component of the first harmonic
Y_k		k-th Fourier components of the light intensity ($k \in \{0, 1, 2 \cdots\}$)
$\alpha(v)$		Absorbance
β_k^{X}	[°]	Phases of the reference signal at the X axis ($k \in \{1, 2, 3 \cdots\}$)
β_k^{Y}	[°]	Phases of the reference signal at the Y axis ($k \in \{1, 2, 3 \cdots\}$)
γ	[cm^{-1}]	Line width
γ_G	[cm^{-1}]	Line width of the Gaussian profile
γ_L	[cm^{-1}]	Line width of the Lorentzian Profile
δ_{ki}		Kronecker delta
δv	[Hz]	Free spectral range (FSR)
η	[°]	Phase shift in wavelength
λ	[nm]	Wavelength
$\varsigma(\omega)$		Frequency dependency of the current-to-wavenumber tuning coefficient
σ_{Allan}		Allan Deviation
$\sigma_{\mathrm{Allan}}^{\mathrm{min}}$		Minimum Allan Deviation
$\tau(v)$		Laser transmission
τ_{opt}	[s]	Optimum integrating time
$\varphi(v)$	[cm]	Line profile
χ_{air}	[cm^{-1}/atm]	Coefficient of air collisional broadening
χ_{self}	[cm^{-1}/atm]	Coefficient of self collisional broadening
ψ_k	[°]	Phase shift between the wavelength and k-th order light intensity modulations ($k \in \{1, 2, 3 \cdots\}$)
ω	[rad/s]	Modulation angular frequency

Acronyms

a.g.l.	above ground level.
a.s.l.	above sea level.
ARL	Air Resources Laboratory.
CET	Central European Time.
CF	Concentration Field.
CFD	Computational Fluid Dynamics.
CPF	Conditional Probability Function.
CRDS	Cavity Ring Down Spectrometer.
CWT	Concentration Weighted Trajectory.
DBR	Distributed Bragg Reflector.
DFB	Distributed-Feedback.
DST	Daylight Saving Time.
FFT	Fast Fourier Transform.
FSR	Free Spectral Range.
GHG	Greenhouse Gas.
HITRAN	High Resolution Transmission.
HLC	Hourly Lowest Concentration.
HPB	HohenPeißenBerg.
HWHM	Halfwidth at Half Maximum.
HySPLIT	Hybrid Single Particle Lagrangian Integrated Trajectory.
LIA	Lock-In Amplifier.
LLSCF	Linear Least Square Curve Fitting.
LRZ	Leibniz Supercomputing Center (Leibniz-Rechenzenturm).
NDIR	Nondispersive Infrared.
NOAA	National Oceanic and Atmospheric Administration.
NRT	Near Real Time.

OCO-2	Orbiting Carbon Observatory - 2.
ODIAC	Open-source Data Inventory for Anthropogenic CO_2.
PBL	Planetary Boundary Layer.
PD	Photodetector.
ppm	Parts Per Million.
PSCF	Potential Source Contribution Function.
RAM	Residual Amplitude Modulation.
SIF	Solar-Induced Fluorescence.
SNR	Signal-to-Noise Ratio.
STILT	Stochastic Time-Inverted Lagrangian Transport.
TDLAS	Tunable Diode Laser Absorption Spectroscopy.
UTC	Coordinated Universal Time.
VCSEL	Vertical-Cavity Surface-Emitting Laser.
VPR	Vegetation Photosynthesis and Respiration.
WKND	Weekend.
WMS	Wavelength Modulation Spectroscopy.
WRF	Weather Research and Forecasting.
ZSF	Zugspitze Schneefernerhaus.

List of Figures

List of Tables

Bibliography

[1] R. K. Pachauri, L. Meyer, M. R. Allen, V. R. Barros, J. Broome, W. Cramer, R. Christ, J. A. Church, L. Clarke, Q. Dahe, P. Dasgupta, N. K. Dubash, et al. Climate change 2014: Synthesis report. contribution of working groups I, II and III to the fifth assessment report of the intergovernmental panel on climate change. Technical report, Intergovernmental Panel on Climate Change, 2014.

[2] NOAA. NOAA. `https://www.esrl.noaa.gov/gmd/ccgg/trends/full.html`, 2019.

[3] C. D. Keeling, R. B. Bacastow, A. E. Bainbridge, C. A. Ekdahl Jr, P. R. Guenther, L. S. Waterman, and J. F. Chin. Atmospheric carbon dioxide variations at Mauna Loa observatory, Hawaii. *Tellus*, 28(6):538–551, 1976.

[4] F. Bréon, G. Broquet, V. Puygrenier, F. Chevallier, I. Xueref-Remy, M. Ramonet, E. Dieudonné, M. Lopez, M. Schmidt, O. Perrussel, et al. An attempt at estimating Paris area CO_2 emissions from atmospheric concentration measurements. *Atmospheric Chemistry and Physics*, 15(4):1707–1724, 2015.

[5] K. McKain, S. Wofsy, T. Nehrkorn, J. Eluszkiewicz, J. Ehleringer, and B. Stephens. Assessment of ground-based atmospheric observations for verification of greenhouse gas emissions from an urban region. *Proceedings of the National Academy of Sciences*, 109(22):8423–8428, 2012.

[6] F. Institute. Fraunhofer in benediktbeuern glashuette und werkstatt. Website, 2008. Online available at `https://www.fraunhofer.de/content/dam/zv/de/publikationen/broschueren/FraunhoferinBenediktbeuern.pdf`; Retrieved 28. May 2018.

[7] R. Riekher. *Fraunhofer und der Beginn der Astrospektroskopie*. na, 2009.

[8] W. Zhang, Y. Tang, A. Shi, L. Bao, Y. Shen, R. Shen, and Y. Ye. Recent developments in spectroscopic techniques for the detection of explosives. *Materials*, 11(8):1364, 2018.

[9] K. Hungershoefer, F.-M. Breon, P. Peylin, F. Chevallier, P. Rayner, A. Klonecki, S. Houweling, and J. Marshall. Evaluation of various observing systems for the global monitoring of CO_2 surface fluxes. *Atmospheric Chemistry and Physics*, 10(21):10503–10520, 2010.

[10] H. H. Aumann and R. J. Pagano. Atmospheric infrared sounder on the Earth Observing System. *Optical Engineering*, 33(3):776–785, 1994.

[11] H. H. Aumann and C. R. Miller. Atmospheric infrared sounder (AIRS) on the Earth observing system. In *Advanced and Next-Generation Satellites*, volume 2583, pages 332–344. International Society for Optics and Photonics, 1995.

[12] T. Hamazaki, Y. Kaneko, A. Kuze, and K. Kondo. Fourier transform spectrometer for greenhouse gases observing satellite (GOSAT). In *Enabling sensor and platform technologies for spaceborne remote sensing*, volume 5659, pages 73–81. International Society for Optics and Photonics, 2005.

[13] F. Sakuma, C. Bruegge, D. Rider, D. Brown, S. Geier, S. Kawakami, and A. Kuze. OCO/GOSAT preflight cross-calibration experiment. *IEEE Transactions on Geoscience and Remote Sensing*, 48(1):585–599, 2010.

[14] J. Heymann, M. Reuter, M. Hilker, M. Buchwitz, O. Schneising, H. Bovensmann, J. Burrows, A. Kuze, H. Suto, N. Deutscher, et al. Consistent satellite XCO_2 retrievals from SCIAMACHY and GOSAT using the BESD algorithm. *Atmospheric Measurement Techniques*, 8(7):2961–2980, 2015.

[15] A. Eldering, S. Boland, B. Solish, D. Crisp, P. Kahn, and M. Gunson. High precision atmospheric CO_2 measurements from space: The design and implementation of OCO-2. In *2012 IEEE Aerospace Conference*, pages 1–10. IEEE, 2012.

[16] A. Liang, W. Gong, and G. Han. OCO-2 XCO_2 validation using TCCON data. In *Geoscience and Remote Sensing Symposium (IGARSS), 2016 IEEE International*, pages 830–833. IEEE, 2016.

[17] A. Liang, G. Han, W. Gong, J. Yang, and C. Xiang. Comparison of global XCO_2 concentrations from OCO-2 with TCCON data in terms of latitude zones. *IEEE Journal of Selected Topics in Applied Earth Observations and Remote Sensing*, 10(6):2491–2498, 2017.

[18] S. Bhattacharjee and J. Chen. Prediction of satellite-based column CO_2 concentration by combining emission inventory and LULC information. *IEEE Transactions on Geoscience and Remote Sensing*, pages 1–16, 2020. `doi:10.1109/TGRS.2020.2985047`.

[19] Y. Liu, D. Yang, and Z. Cai. A retrieval algorithm for TanSat XCO_2 observation: Retrieval experiments using GOSAT data. *Chinese Science Bulletin*, 58(13):1520–1523, 2013.

[20] Z. Cai, Y. Liu, and D. Yang. Analysis of XCO_2 retrieval sensitivity using simulated Chinese Carbon Satellite (TanSat) measurements. *Science China Earth Sciences*, 57(8):1919–1928, 2014.

[21] V. Velazco, M. Buchwitz, H. Bovensmann, M. Reuter, O. Schneising, J. Heymann, T. Krings, K. Gerilowski, and J. Burrows. Towards space based verification of CO_2 emissions from strong localized sources: fossil fuel power plant emissions as seen by a CarbonSat constellation. *Atmospheric Measurement Techniques*, 4(12):2809–2822, 2011.

[22] X. Wang, Z. Guo, Y. Huang, H. Fan, and W. Li. A cloud detection scheme for the Chinese carbon dioxide observation satellite (TANSAT). *Advances in Atmospheric Sciences*, 34(1):16–25, 2017.

[23] J. Kshtriya. *Autonomous ground target tracking, testing, commissioning and operations for greenhouse gas satellite demonstrator (GHGSat-D)*. PhD thesis, University of Toronto, 2017.

[24] S. Gousset, E. Le Coarer, N. Guérineau, L. Croizé, T. Laveille, and Y. Ferrec. NANOCARB-21: a miniature Fourier-transform spectro-imaging concept for a daily monitoring of greenhouse gas concentration on the Earth surface. In *International Conference on Space Optics—ICSO 2016*, volume 10562, page 105624U. International Society for Optics and Photonics, 2017.

[25] C. Deniel, B. Millet, F. Buisson, C. Pierangelo, D. Jouglet, F.-M. Bréon, P. Bousquet, F. Chevallier, C. Crevoisier, and G. Ehret. MERLIN and MICROCARB: Preparation of 2 space missions for CO_2 and CH_4. In *EGU General Assembly Conference Abstracts*, volume 19, page 5276, 2017.

[26] TCCON. TCCON. `http://www.tccon.caltech.edu/`, 2019.

[27] D. Wunch, G. C. Toon, J.-F. L. Blavier, R. A. Washenfelder, J. Notholt, B. J. Connor, D. W. Griffith, V. Sherlock, and P. O. Wennberg. The total carbon column observing network. *Philosophical Transactions of the Royal Society A: Mathematical, Physical and Engineering Sciences*, 369(1943):2087–2112, 2011.

[28] T. Borsdorff, H. Hu, P. Nédélec, I. Aben, J. Landgraf, et al. Carbon monoxide column retrieval for clear-sky and cloudy atmospheres: a full-mission data set from SCIAMACHY 2.3 μm reflectance measurements. *Atmospheric Measurement Techniques*, 10(5):1769–1782, 2017.

[29] S. Dohe. *Measurements of atmospheric CO_2 columns using ground-based FTIR spectra*. PhD thesis, Karlsruher Institut für Technologie (KIT), 2013.

[30] F. Hase, M. Frey, T. Blumenstock, J. Groß, M. Kiel, R. Kohlhepp, G. Mengistu Tsidu, K. Schäfer, M. Sha, and J. Orphal. Application of portable FTIR spectrometers for detecting greenhouse gas emissions of the major city Berlin. *Atmospheric Measurement Techniques*, 8(7):3059–3068, 2015.

[31] C. Viatte, T. Lauvaux, J. K. Hedelius, H. Parker, J. Chen, T. Jones, J. E. Franklin, A. J. Deng, B. Gaudet, K. Verhulst, et al. Methane emissions from dairies in the Los Angeles Basin. *Atmospheric Chemistry and Physics*, 17(12):7509–7528, 2017.

[32] M. Frey, M. K. Sha, F. Hase, M. Kiel, T. Blumenstock, R. Harig, G. Surawicz, N. M. Deutscher, K. Shiomi, J. E. Franklin, H. Bosch, J. Chen, M. Grutter, H. Ohyama, Y. Sun, A. Butz, G. Mengistu Tsidu, D. Ene, D. Wunch, Z. Cao, O. E. Garcia, M. Ramonet, F. Vogel, and J. Orphal. Building the COllaborative Carbon Column Observing Network (COCCON): long-term stability and ensemble performance of the EM27/SUN Fourier transform spectrometer. *Atmospheric Measurement Techniques*, 12(3):1513–1530, 2019.

[33] J. Chen, C. Viatte, J. Hedelius, T. Jones, J. Franklin, H. Parker, E. Gottlieb, P. Wennberg, M. Dubey, and S. Wofsy. Differential column measurements using compact solar-tracking spectrometers. *Atmospheric Chemistry and Physics*, 16(13):8479–8498, 2016.

[34] J. Hedelius, C. Viatte, D. Wunch, C. Roehl, G. Toon, J. Chen, T. Jones, S. Wofsy, J. Franklin, H. Parker, M. Dubey, and P. Wennberg. Assessment of errors and biases in retrievals of X_{co_2}, X_{ch_4}, X_{CO}, and X_{n_2o} from a 0.5 cm^{-1} resolution solar-viewing spectrometer. *Atmospheric Measurement Techniques*, 9(8):3527–3546, 2016.

[35] L. Heinle and J. Chen. Automated enclosure and protection system for compact solar-tracking spectrometers. *Atmospheric Measurement Techniques*, 11(4):2173–2185, 2018.

[36] F. Dietrich, J. Chen, B. Voggenreiter, and X. Zhao. Greenhouse gas emission estimate using a fully-automated permanent sensor network in Munich. In *EGU General Assembly Conference Abstracts*, page 19237, 2020.

[37] Y. Tohjima, K. Katsumata, I. Morino, H. Mukai, T. Machida, I. Akama, T. Amari, and U. Tsunogai. Theoretical and experimental evaluation of the isotope effect of NDIR analyzer on atmospheric CO_2 measurement. *Journal of Geophysical Research: Atmospheres*, 114:D13302, 2009.

[38] F. Jin, Y. Fang, T. Chen, D. Li, J. Kim, M.-K. Park, S. Park, and K.-R. Kim. In situ measurement of atmospheric carbon dioxide at Yanbian, China: Estimating its northeast Asian emission regions. *Science China Earth Sciences*, 55(10):1742–1754, 2012.

[39] T. Yasuda, S. Yonemura, and A. Tani. Comparison of the characteristics of small commercial NDIR CO_2 sensor models and development of a portable CO_2 measurement device. *Sensors*, 12(3):3641–3655, 2012.

[40] D. Gibson and C. MacGregor. A novel solid state non-dispersive infrared CO_2 gas sensor compatible with wireless and portable deployment. *Sensors*, 13(6):7079–7103, 2013.

[41] P. S. Bakwin, P. P. Tans, D. F. Hurst, and C. Zhao. Measurements of carbon dioxide on very tall towers: results of the NOAA/CMDL program. *Tellus B: Chemical and Physical Meteorology*, 50(5):401–415, 1998.

[42] E. Crosson. A cavity ring-down analyzer for measuring atmospheric levels of methane, carbon dioxide, and water vapor. *Applied Physics B*, 92(3):403–408, 2008.

[43] C. Yver Kwok, O. Laurent, A. Guemri, C. Philippon, B. Wastine, C. Rella, C. Vuillemin, F. Truong, M. Delmotte, V. Kazan, et al. Comprehensive laboratory and field testing of cavity ring-down spectroscopy analyzers measuring H_2O, CO_2, CH_4 and CO. *Atmospheric Measurement Techniques*, 8(9):3867–3892, 2015.

[44] L. Hazan, J. Tarniewicz, M. Ramonet, O. Laurent, and A. Abbaris. Automatic processing of atmospheric CO_2 and CH_4 mole fractions at the ICOS Atmosphere Thematic Centre. *Atmospheric Measurement Techniques*, 9(9):4719–4736, 2016.

[45] F. J. Duarte. *Tunable lasers handbook*. Elsevier, 1996.

[46] J. Jiang, M. Zhao, G. Ma, H. Song, C. Li, X. Han, and C. Zhang. TDLAS-based detection of dissolved methane in power transformer oil and field application. *IEEE Sensors Journal*, 18(6):2318–2325, 2018.

[47] C. Liu, Z. Cao, Y. Lin, L. Xu, and H. McCann. Online cross-sectional monitoring of a swirling flame using TDLAS tomography. *IEEE Transactions on Instrumentation and Measurement*, 67(6):1338–1348, 2018.

[48] J. Reid and D. Labrie. Second-harmonic detection with tunable diode lasers–comparison of experiment and theory. *Applied Physics B*, 26(3):203–210, 1981.

[49] S. So, D. Chang, O. Al'Rifai, G. Wysocki, A. Kosterev, and F. Tittel. Development of laser based spectroscopic trace-gas sensors for environmental sensor networks and medical exposure monitors. In *Quantum Electronics and Laser Science Conference*, page JTuA94. Optical Society of America, 2008.

[50] J. Chen, A. Hangauer, R. Strzoda, and M.-C. Amann. Laser spectroscopic oxygen sensor using diffuse reflector based optical cell and advanced signal processing. *Applied Physics B*, 100(2):417–425, 2010.

[51] A. Hangauer, J. Chen, R. Strzoda, M. Fleischer, and M.-C. Amann. Performance of a fire detector based on a compact laser spectroscopic carbon monoxide sensor. *Optics Express*, 22(11):13680–13690, 2014.

[52] J. Chen, A. Hangauer, R. Strzoda, and M.-C. Amann. Experimental characterization of the frequency modulation behavior of vertical cavity surface emitting lasers. *Applied Physics Letters*, 91(14):141105, 2007.

[53] J. Chen, A. Hangauer, and M.-C. Amann. Simplified model of the dynamic thermal tuning behavior of VCSELs. *IEEE Photonics Technology Letters*, 20(13):1082–1084, 2008.

[54] A. Hangauer, J. Chen, R. Strzoda, M. Ortsiefer, and M.-C. Amann. Wavelength modulation spectroscopy with a widely tunable InP-based 2.3 μm vertical-cavity surface-emitting laser. *Optics Letters*, 33(14):1566–1568, 2008.

[55] J. Chen, A. Hangauer, A. Bachmann, T. Lim, K. Kashani, R. Strzoda, and M.-C. Amann. CO and CH_4 sensing with single mode 2.3 μm GaSb-based VCSEL. In *2009 Conference on Lasers and Electro-Optics and Quantum electronics and Laser Science Conference*. IEEE, 2009. `doi:10.1364/CLEO.2009.CThI2`.

[56] J. Chen, A. Hangauer, R. Strzoda, and M.-C. Amann. Tunable diode laser spectroscopy with optimum wavelength scanning. *Applied Physics B*, 100(2):331–339, 2010.

[57] A. Hangauer, J. Chen, and M. Amann. Vertical-cavity surface-emitting laser light–current characteristic at constant internal temperature. *IEEE Photonics Technology Letters*, 23(18):1295–1297, 2011.

[58] A. Hangauer, J. Chen, R. Strzoda, and M.-C. Amann. The frequency modulation response of vertical-cavity surface-emitting lasers: experiment and theory. *IEEE Journal of Selected Topics in Quantum Electronics*, 17(6):1584–1593, 2011.

[59] G. Boehm, A. Bachmann, J. Rosskopf, M. Ortsiefer, J. Chen, A. Hangauer, R. Meyer, R. Strzoda, and M.-C. Amann. Comparison of InP-and GaSb-based VCSELs emitting at 2.3 μm suitable for carbon monoxide detection. *Journal of Crystal Growth*, 323(1):442–445, 2011.

[60] Y. Meng, T. Liu, K. Liu, J. Jiang, R. Wang, T. Wang, and H. Hu. A modified empirical mode decomposition algorithm in TDLAS for gas detection. *IEEE Photonics Journal*, 6(6):1–7, 2014.

[61] Y. Wang, Y. Wei, J. Chang, T. Zhang, T. Liu, T. Sun, and K. Grattan. Tunable diode laser absorption spectroscopy-based detection of propane for explosion early warning by using a vertical cavity surface enhanced laser source and principle component analysis approach. *IEEE Sensors Journal*, 17(15):4975–4982, 2017.

[62] H. Li, G. B. Rieker, X. Liu, J. B. Jeffries, and R. K. Hanson. Extension of wavelength-modulation spectroscopy to large modulation depth for diode laser absorption measurements in high-pressure gases. *Applied Optics*, 45(5):1052–1061, 2006.

[63] Z. Peng, Y. Ding, L. Che, X. Li, and K. Zheng. Calibration-free wavelength modulated TDLAS under high absorbance conditions. *Optics Express*, 19(23):23104–23110, 2011.

[64] L. Lan, Y. Ding, Z. Peng, Y. Du, and Y. Liu. Calibration-free wavelength modulation for gas sensing in tunable diode laser absorption spectroscopy. *Applied Physics B*, 117(4):1211–1219, 2014.

[65] C. Liu and L. Xu. Laser absorption spectroscopy for combustion diagnosis in reactive flows: A review. *Applied Spectroscopy Reviews*, 54(1):1–44, 2019.

[66] J. Liu, J. Jeffries, and R. Hanson. Wavelength modulation absorption spectroscopy with $2f$ detection using multiplexed diode lasers for rapid temperature measurements in gaseous flows. *Applied Physics B*, 78(3-4):503–511, 2004.

[67] A. J. McGettrick, K. Duffin, W. Johnstone, G. Stewart, and D. G. Moodie. Tunable diode laser spectroscopy with wavelength modulation: a phasor decomposition method for calibration-free measurements of gas concentration and pressure. *Journal of Lightwave Technology*, 26(4):432–440, 2008.

[68] W. Johnstone, A. J. McGettrick, K. Duffin, A. Cheung, and G. Stewart. Tunable diode laser spectroscopy for industrial process applications: System characterization in conventional and new approaches. *IEEE Sensors Journal*, 8(7):1079–1088, 2008.

[69] G. Stewart, W. Johnstone, J. Bain, K. Ruxton, and K. Duffin. Recovery of absolute gas absorption line shapes using tunable diode laser spectroscopy with wavelength modulation–Part I: Theoretical analysis. *Journal Lightwave Technology*, 29(6):811–821, 2011.

[70] T. Benoy, M. Lengden, G. Stewart, and W. Johnstone. Recovery of absorption line shapes with correction for the wavelength modulation characteristics of DFB lasers. *IEEE Photonics Journal*, 8(3):1–17, 2016.

[71] D. M. Sonnenfroh, W. T. Rawlins, M. G. Allen, C. Gmachl, F. Capasso, A. L. Hutchinson, D. L. Sivco, J. N. Baillargeon, and A. Y. Cho. Application of balanced detection to absorption measurements of trace gases with room-temperature, quasi-cw quantum-cascade lasers. *Applied Optics*, 40(6):812–820, 2001.

[72] A. L. Chakraborty, K. Ruxton, W. Johnstone, M. Lengden, and K. Duffin. Elimination of residual amplitude modulation in tunable diode laser wavelength modulation spectroscopy using an optical fiber delay line. *Optics Express*, 17(12):9602–9607, 2009.

[73] J. R. Bain, M. Lengden, G. Stewart, and W. Johnstone. Recovery of absolute absorption line shapes in tunable diode laser spectroscopy using external amplitude modulation with balanced detection. *IEEE Sensors Journal*, 16(3):675–680, 2016.

[74] A. Hangauer, J. Chen, and M.-C. Amann. Modeling of the n-th harmonic spectra used in wavelength modulation spectroscopy and their properties. *Applied Physics B*, 90(2):249–254, 2008.

[75] A. Hangauer, J. Chen, R. Strzoda, and M.-C. Amann. Multi-harmonic detection in wavelength modulation spectroscopy systems. *Applied Physics B*, 110(2):177–185, 2013.

[76] A. Hangauer. *Detection schemes, algorithms and device modeling for tunable diode laser absorption spectroscopy*. PhD thesis, Technische Universität München, 2013.

[77] Z. Peng, Y. Ding, J. Jia, L. Lan, Y. Du, and Z. Li. First harmonic with wavelength modulation spectroscopy to measure integrated absorbance under low absorption. *Optics Express*, 21(20):23724–23735, 2013.

[78] Z. Peng, Y. Ding, L. Che, and Q. Yang. Odd harmonics with wavelength modulation spectroscopy for recovering gas absorbance shape. *Optics Express*, 20(11):11976–11985, 2012.

[79] L. Lan, Y. Ding, Z. Peng, Y. Du, Y. Liu, and Z. Li. Multi-harmonic measurements of line shape under low absorption conditions. *Applied Physics B*, 117(2):543–547, 2014.

[80] Y. Du, L. Lan, Y. Ding, and Z. Peng. Measurement of the absolute absorbance based on wavelength modulation spectroscopy. *Applied Physics B*, 123(7):205, 2017.

[81] J. Chen, A. Hangauer, R. Strzoda, M. Fleischer, and M.-C. Amann. Low-level and ultralow-volume hollow waveguide based carbon monoxide sensor. *Optics Letters*, 35(21):3577–3579, 2010.

[82] J. Chen, A. Hangauer, R. Strzoda, and M. C. Amann. Resolution limits of laser spectroscopic absorption measurements with hollow glass waveguides. *Applied Optics*, 49(28):5254–5261, 2010.

[83] J. Chen. *Compact laser-spectroscopic gas sensors using vertical-cavity surface-emitting lasers*. PhD thesis, Technische Universität München, 2011.

[84] A. Hangauer, J. Chen, K. Seemann, P. Karge, R. Strzoda, and M. Amann. Compact VCSEL-based CO_2 and H_2O sensor with inherent wavelength calibration for safety and air-quality applications. In *Conference on Lasers and Electro-Optics*, page JThB3. Optical Society of America, 2010.

[85] J. Chen, A. Hangauer, R. Strzoda, and M.-C. Amann. VCSEL-based calibration-free carbon monoxide sensor at 2.3 μm with in-line reference cell. *Applied Physics B*, 102(2):381–389, 2011.

[86] L. Lan, J. Chen, X. Zhao, and H. Ghasemifard. VCSEL-based atmospheric trace gas sensor using first harmonic detection. *IEEE Sensors Journal*, 19(13):4923–4931, 2019.

[87] W. Demtröder. *Laser spectroscopy: basic concepts and instrumentation*. Springer Science & Business Media, 2013.

[88] L. S. Rothman, I. E. Gordon, A. Barbe, D. C. Benner, P. F. Bernath, M. Birk, V. Boudon, L. R. Brown, A. Campargue, J.-P. Champion, et al. The HITRAN 2008 molecular spectroscopic database. *Journal of Quantitative Spectroscopy and Radiative Transfer*, 110(9-10):533–572, 2009.

[89] Y. Liu, J. Lin, G. Huang, Y. Guo, and C. Duan. Simple empirical analytical approximation to the Voigt profile. *Journal of the Optical Society of America B*, 18(5):666–672, 2001.

[90] L. Lan, J. Chen, Y. Wu, Y. Bai, X. Bi, and Y. Li. Self-calibrated multiharmonic CO_2 sensor using VCSEL for urban in situ measurement. *IEEE Transactions on Instrumentation and Measurement*, 68(4):1140–1147, 2019.

[91] A. Savitzky and M. Golay. Smoothing and differentiation of data by simplified least squares procedures. *Analytical Chemistry*, 36(8):1627–1639, 1964.

[92] Vertilas. Products. `https://vertilas.com/content/products/`, 2019.

[93] Finisar. VCSEL technology. `https://www.myvcsel.com/technology`, 2019.

[94] D. Allan. Statistics of atomic frequency standards. *Proceedings of the IEEE*, 54(2):221–230, 1966.

[95] P. Werle, R. Mücke, and F. Slemr. The limits of signal averaging in atmospheric trace-gas monitoring by tunable diode-laser absorption spectroscopy (TDLAS). *Applied Physics B*, 57(2):131–139, 1993.

[96] R. Stull. *An introduction to boundary layer meteorology*, volume 13. Springer Science & Business Media, 2012.

[97] J. Moore and A. Jacobson. Seasonally varying contributions to urban CO_2 in the Chicago, Illinois, USA region: Insights from a high-resolution CO_2 concentration and $\delta^{13}C$ record. *Elementa: Science of the Anthropocene*, 3:000052, 2015.

[98] J. Xu, X. Lee, W. Xiao, C. Cao, S. Liu, X. Wen, J. Xu, Z. Zhang, and J. Zhao. Interpreting the $^{13}C/^{12}C$ ratio of carbon dioxide in an urban airshed in the Yangtze River Delta, China. *Atmospheric Chemistry and Physics*, 17(5):3385–3399, 2017.

[99] Oktoberfest. Oktoberfest. `https://www.oktoberfest2017.de/`, 2017.

[100] J. Chen, F. Dietrich, H. Maazallahi, A. Forstmaier, D. Winkler, M. E. Hofmann, H. Denier van der Gon, and T. Röckmann. Methane emissions from the Munich Oktoberfest. *Atmospheric Chemistry and Physics*, 20(6):3683–3696, 2020.

[101] Munich. Fireworks. `https://www.newyearsevelive.net/cities/munich.html`, 2019.

[102] L. Lan, H. Ghasemifard, Y. Yuan, S. Hachinger, X. Zhao, S. Bhattacharjee, X. Bi, Y. Bai, A. Menzel, and J. Chen. Assessment of urban CO_2 measurement and source attribution in Munich based on TDLAS-WMS and trajectory analysis. *Atmosphere*, 11(1):58, 2020.

[103] T. Oda, S. Maksyutov, and R. J. Andres. The Open-source Data Inventory for Anthropogenic CO_2, version 2016 (ODIAC2016): a global monthly fossil fuel CO_2 gridded emissions data product for tracer transport simulations and surface flux inversions. *Earth System Science Data*, 10(1):87–107, 2018.

[104] NIES. ODIAC. `http://www.odiac.org/index.html`, 2019.

[105] Google. Earth. `https://www.google.com/earth/`, 2019.

[106] WIKI. Munich. `https://en.wikipedia.org/wiki/Munich`, 2019.

[107] A. Dilley. On the computer calculation of vapor pressure and specific humidity gradients from psychrometric data. *Journal of Applied Meteorology*, 7(4):717–719, 1968.

[108] J. Sullivan and L. D. Sanders. Method for obtaining wet-bulb temperatures by modifying the psychrometric formula. *National Oceanic and Atmospheric Administration (NOAA)*, pages 1–8, 1974.

[109] D. C. Carslaw and K. Ropkins. Openair–an R package for air quality data analysis. *Environmental Modelling & Software*, 27:52–61, 2012.

[110] G. P. Brasseur and D. J. Jacob. *Modeling of Atmospheric Chemistry*. Cambridge University Press, 2017.

[111] J. H. Seinfeld and S. N. Pandis. *Atmospheric chemistry and physics: from air pollution to climate change*. John Wiley & Sons, 2016.

[112] S. Newman, S. Jeong, M. Fischer, X. Xu, C. Haman, B. Lefer, S. Alvarez, B. Rappenglueck, E. Kort, A. Andrews, et al. Diurnal tracking of anthropogenic CO_2 emissions in the Los Angeles basin megacity during spring 2010. *Atmospheric Chemistry and Physics*, 13(8):4359–4372, 2013.

[113] R. Kretschmer, C. Gerbig, U. Karstens, and F.-T. Koch. Error characterization of CO_2 vertical mixing in the atmospheric transport model WRF-VPRM. *Atmospheric Chemistry and Physics*, 12(5):2441–2458, 2012.

[114] A. Porcar-Castell, E. Tyystjärvi, J. Atherton, C. Van der Tol, J. Flexas, E. E. Pfündel, J. Moreno, C. Frankenberg, and J. A. Berry. Linking chlorophyll a fluorescence to photosynthesis for remote sensing applications: mechanisms and challenges. *Journal of Experimental Botany*, 65(15):4065–4095, 2014.

[115] X. Li, J. Xiao, and B. He. Chlorophyll fluorescence observed by OCO-2 is strongly related to gross primary productivity estimated from flux towers in temperate forests. *Remote Sensing of Environment*, 204:659–671, 2018.

[116] C. Frankenberg, A. Butz, and G. Toon. Disentangling chlorophyll fluorescence from atmospheric scattering effects in O_2 A-band spectra of reflected sun-light. *Geophysical Research Letters*, 38(3):L03801, 2011.

[117] C. Frankenberg, J. B. Fisher, J. Worden, G. Badgley, S. S. Saatchi, J.-E. Lee, G. C. Toon, A. Butz, M. Jung, A. Kuze, et al. New global observations of the terrestrial carbon cycle from GOSAT: Patterns of plant fluorescence with gross primary productivity. *Geophysical Research Letters*, 38(17):L17706, 2011.

[118] C. Frankenberg, C. O'Dell, J. Berry, L. Guanter, J. Joiner, P. Köhler, R. Pollock, and T. E. Taylor. Prospects for chlorophyll fluorescence remote sensing from the Orbiting Carbon Observatory-2. *Remote Sensing of Environment*, 147:1–12, 2014.

[119] A. O. Castro, J. Chen, C. S. Zang, A. Shekhar, J. C. Jimenez, S. Bhattacharjee, M. Kindu, V. H. Morales, and A. Rammig. OCO-2 solar-induced chlorophyll fluorescence variability across ecoregions of the Amazon Basin and the extreme drought effects of El Niño (2015–2016). *Remote Sensing*, 12(7):1202, 2020.

[120] NASA. OCO-2. `http://oco2.jpl.nasa.gov`, 2019.

[121] C. Frankenberg. *Solar induced fluorescence OCO-2 Lite files (B700) User Guide*. California Institute of Technology 2015, 2015.

[122] J. Staufer, G. Broquet, F.-M. Bréon, V. Puygrenier, F. Chevallier, I. Xueref-Rémy, E. Dieudonné, M. Lopez, M. Schmidt, M. Ramonet, et al. The first 1-year-long estimate of the Paris region fossil fuel CO_2 emissions based on atmospheric inversion. *Atmospheric Chemistry and Physics*, 16(22):14703–14726, 2016.

[123] R. Vogt, A. Christen, M. Rotach, M. Roth, and A. Satyanarayana. Temporal dynamics of CO_2 fluxes and profiles over a Central European city. *Theoretical and Applied Climatology*, 84(1-3):117–126, 2006.

[124] B. Lietzke and R. Vogt. Variability of CO_2 concentrations and fluxes in and above an urban street canyon. *Atmospheric Environment*, 74:60–72, 2013.

[125] N. Sparks and R. Toumi. Remote sampling of a CO_2 point source in an urban setting. *Atmospheric Environment*, 44(39):5287–5294, 2010.

[126] M. Á. García, M. L. Sánchez, and I. A. Pérez. Differences between carbon dioxide levels over suburban and rural sites in Northern Spain. *Environmental Science and Pollution Research*, 19(2):432–439, 2012.

[127] X. Zhao, J. Marshall, S. Hachinger, C. Gerbig, M. Frey, F. Hase, and J. Chen. Analysis of total column CO_2 and CH_4 measurements in Berlin with WRF-GHG. *Atmospheric Chemistry and Physics*, 19(17):11279–11302, 2019.

[128] World weather attribution. `https://www.worldweatherattribution.org/attribution-of-the-2018-heat-in-northern-europe/`, 2018.

[129] Munich.Landeshauptstadt. Traffic. `https://www.muenchen.de/rathaus/Stadtverwaltung/Referat-fuer-Stadtplanung-und-Bauordnung/Verkehrsplanung/Verkehrsmodell-VisMuc.html`, 2019.

[130] A. G. Williams, S. D. Chambers, F. Conen, S. Reimann, M. Hill, A. D. Griffiths, and J. Crawford. Radon as a tracer of atmospheric influences on traffic-related air pollution in a small inland city. *Tellus B: Chemical and Physical Meteorology*, 68(1):30967, 2016.

[131] A. Rice and G. Bostrom. Measurements of carbon dioxide in an Oregon metropolitan region. *Atmospheric Environment*, 45(5):1138–1144, 2011.

[132] Y. Yuan, L. Ries, H. Petermeier, T. Trickl, M. Leuchner, C. Couret, R. Sohmer, F. Meinhardt, and A. Menzel. On the diurnal, weekly, and seasonal cycles and annual trends in atmospheric CO_2 at Mount Zugspitze, Germany, during 1981–2016. *Atmospheric Chemistry and Physics*, 19(2):999–1012, 2019.

[133] I. Xueref-Remy, E. Dieudonné, C. Vuillemin, M. Lopez, C. Lac, M. Schmidt, M. Delmotte, F. Chevallier, F. Ravetta, O. Perrussel, et al. Diurnal, synoptic and seasonal variability of atmospheric CO_2 in the Paris megacity area. *Atmospheric Chemistry and Physics*, 18(5):3335–3362, 2018.

[134] D. C. Carslaw and S. D. Beevers. Investigating the potential importance of primary NO_2 emissions in a street canyon. *Atmospheric Environment*, 38(22):3585–3594, 2004.

[135] E. J. Westmoreland, N. Carslaw, D. C. Carslaw, A. Gillah, and E. Bates. Analysis of air quality within a street canyon using statistical and dispersion modelling techniques. *Atmospheric Environment*, 41(39):9195–9205, 2007.

[136] F. Massen and E.-G. Beck. Accurate estimation of CO_2 background level from near ground measurements at non-mixed environments. In *The Economic, Social and Political Elements of Climate Change*, pages 509–522. Springer, 2011.

[137] A. Stohl. Trajectory statistics-a new method to establish source-receptor relationships of air pollutants and its application to the transport of particulate sulfate in Europe. *Atmospheric Environment*, 30(4):579–587, 1996.

[138] R. R. Draxler and G. Hess. An overview of the HYSPLIT_4 modelling system for trajectories. *Australian Meteorological Magazine*, 47(4):295–308, 1998.

[139] Y.-J. Han, T. M. Holsen, and P. K. Hopke. Estimation of source locations of total gaseous mercury measured in New York State using trajectory-based models. *Atmospheric Environment*, 41(28):6033–6047, 2007.

[140] Y. Wang, X. Zhang, R. R. Draxler, et al. TrajStat: GIS-based software that uses various trajectory statistical analysis methods to identify potential sources from long-term air pollution measurement data. *Environmental Modelling and Software*, 24(8):938–939, 2009.

[141] A. Stein, R. R. Draxler, G. D. Rolph, B. J. Stunder, M. Cohen, and F. Ngan. NOAA's HYSPLIT atmospheric transport and dispersion modeling system. *Bulletin of the American Meteorological Society*, 96(12):2059–2077, 2015.

[142] J. K. Hedelius, J. Liu, T. Oda, S. Maksyutov, C. M. Roehl, L. T. Iraci, J. R. Podolske, P. W. Hillyard, J. Liang, K. R. Gurney, et al. Southern California megacity CO_2, CH_4, and CO flux estimates using ground-and space-based remote sensing and a Lagrangian model. *Atmospheric Chemistry and Physics*, 18(22):16271–16291, 2018.

[143] H. Ghasemifard, F. R. Vogel, Y. Yuan, M. Luepke, J. Chen, L. Ries, M. Leuchner, C. Schunk, S. Noreen Vardag, and A. Menzel. Pollution events at the high-altitude mountain site Zugspitze-Schneefernerhaus (2670 m a.s.l.), Germany. *Atmosphere*, 10(6):330, 2019.

[144] L. L. Ashbaugh, W. C. Malm, and W. Z. Sadeh. A residence time probability analysis of sulfur concentrations at Grand Canyon National Park. *Atmospheric Environment (1967)*, 19(8):1263–1270, 1985.

[145] N. J. Pekney, C. I. Davidson, L. Zhou, and P. K. Hopke. Application of PSCF and CPF to PMF-modeled sources of PM2.5 in Pittsburgh. *Aerosol Science and Technology*, 40(10):952–961, 2006.

[146] C. A. Brereton and M. R. Johnson. Identifying sources of fugitive emissions in industrial facilities using trajectory statistical methods. *Atmospheric Environment*, 51:46–55, 2012.

[147] N. Liu, Y. Yu, J. He, and S. Zhao. Integrated modeling of urban–scale pollutant transport: application in a semi–arid urban valley, Northwestern China. *Atmospheric Pollution Research*, 4(3):306–314, 2013.

[148] H. Ghasemifard, Y. Yuan, M. Luepke, C. Schunk, J. Chen, L. Ries, M. Leuchner, and A. Menzel. Atmospheric CO_2 and $\delta^{13}C$ measurements from 2012 to 2014 at the Environmental Research Station Schneefernerhaus, Germany: Technical corrections, temporal variations and trajectory clustering. *Aerosol and Air Quality Research*, 19:657–670, 2019.

[149] A. Lupu and W. Maenhaut. Application and comparison of two statistical trajectory techniques for identification of source regions of atmospheric aerosol species. *Atmospheric Environment*, 36(36-37):5607–5618, 2002.

[150] Y. K. Hsu, T. M. Holsen, and P. K. Hopke. Comparison of hybrid receptor models to locate PCB sources in Chicago. *Atmospheric Environment*, 37(4):545–562, 2003.

[151] V. P. Kabashnikov, A. P. Chaikovsky, T. L. Kucsera, and N. S. Metelskaya. Estimated accuracy of three common trajectory statistical methods. *Atmospheric Environment*, 45(31):5425–5430, 2011.

[152] I. Cheng, L. Zhang, P. Blanchard, J. Dalziel, and R. Tordon. Concentration-weighted trajectory approach to identifying potential sources of speciated atmospheric mercury at an urban coastal site in Nova Scotia, Canada. *Atmospheric Chemistry and Physics*, 13(12):6031–6048, 2013.

[153] K. Dimitriou, E. Remoundaki, E. Mantas, and P. Kassomenos. Spatial distribution of source areas of PM2.5 by Concentration Weighted Trajectory (CWT) model applied in PM2.5 concentration and composition data. *Atmospheric Environment*, 116:138–145, 2015.

[154] V. Salamalikis, A. Argiriou, and E. Dotsika. Stable isotopic composition of atmospheric water vapor in Patras, Greece: A concentration weighted trajectory approach. *Atmospheric Research*, 152:93–104, 2015.

[155] B. Wolf, C. Chwala, B. Fersch, J. Garvelmann, W. Junkermann, M. J. Zeeman, A. Angerer, B. Adler, C. Beck, C. Brosy, et al. The SCALEX campaign: Scale-crossing land surface and boundary layer processes in the TERENO-preAlpine observatory. *Bulletin of the American Meteorological Society*, 98(6):1217–1234, 2017.

[156] Y. Yuan, L. Ries, H. Petermeier, M. Steinbacher, A. J. Gómez-Peláez, M. C. Leuenberger, M. Schumacher, T. Trickl, C. Couret, F. Meinhardt, et al. Adaptive selection of diurnal minimum variation: a statistical strategy to obtain representative atmospheric CO_2 data and its application to European elevated mountain stations. *Atmospheric Measurement Techniques*, 11(3):1501–1514, 2018.

[157] J. Lin, C. Gerbig, S. Wofsy, A. Andrews, B. Daube, K. J. Davis, and C. Grainger. A near-field tool for simulating the upstream influence of atmospheric observations: The Stochastic Time-Inverted Lagrangian Transport (STILT) model. *Journal of Geophysical Research: Atmospheres*, 108(D16), 2003.

[158] F. Toja-Silva, J. Chen, S. Hachinger, and F. Hase. CFD simulation of CO_2 dispersion from urban thermal power plant: Analysis of turbulent Schmidt number and comparison with Gaussian plume model and measurements. *Journal of Wind Engineering and Industrial Aerodynamics*, 169:177–193, 2017.

[159] F. Toja-Silva, C. Pregel-Hoderlein, and J. Chen. On the urban geometry generalization for CFD simulation of gas dispersion from chimneys: Comparison with Gaussian plume model. *Journal of Wind Engineering and Industrial Aerodynamics*, 177:1–18, 2018.

[160] F. Toja-Silva, T. Kono, C. Peralta, O. Lopez-Garcia, and J. Chen. A review of computational fluid dynamics (CFD) simulations of the wind flow around buildings for urban wind energy exploitation. *Journal of Wind Engineering and Industrial Aerodynamics*, 180:66–87, 2018.

Publications

Journal

[1] **L. Lan**, H. Ghasemifard, Y. Yuan, S. Hachinger, X. Zhao, S. Bhattacharjee, X. Bi, Y. Bai, A. Menzel, and J. Chen, Assessment of urban CO_2 concentrations and source attributions in Munich based on TDLAS-WMS sensor and trajectory analysis, *Atmosphere*, 2020, 11(1): 58.

[2] **L. Lan**, J. Chen, X. Zhao, and H. Ghasemifard, VCSEL-based atmospheric trace gas sensor using first harmonic detection, *IEEE Sensors Journal*, 2019, 19(13): 4923–4931.

[3] **L. Lan**, J. Chen, Y. Wu, Y. Bai, X. Bi, and Y. Li, Self-calibrated multiharmonic CO_2 sensor using VCSEL for urban *in-situ* measurement, *IEEE Transactions on Instrumentation and Measurement*, 2019, 68(4): 1140–1147.

[4] Y. Du, **L. Lan**, Y. Ding, and Z. Peng, Measurement of the absolute absorbance based on wavelength modulation spectroscopy, *Applied Physics B - Lasers and Optics*, 2017, 123: 205.

[5] Y. Wu, M. Brunel, R. Li, **L. Lan**, W. Ao, J. Chen, X. Wu, and G. Gréhan, Simultaneous amplitude and phase contrast imaging of burning fuel particle and flame with digital inline holography: Model and verification, *Journal of Quantitative Spectroscopy and Radiative Transfer*, 2017, 199: 26–35.

Conference

[1] **L. Lan**, J. Chen, X. Zhao, Y. Bai, H. Ghasemifard, and S. Hachinger, Continuous urban *in-situ* CO_2 measurement at Munich using TDLAS-WMS method and VCSEL laser, *EGU 2019 General Assembly*, Vienna, Austria, Apr. 7–12, 2019.

[2] J. Chen, F. Dietrich, **L. Lan**, Y. Bai, A. Forstmaier, and L. Setili, Greenhouse Gas Monitoring in Munich and Development of CO_2 and NOx Sensors, *German-Sino Symposium*, "Development of New Monitoring Strategies for the Investigation of Acute Air Pollution and Bioaerosol Episodes and Reducing Their Impacts on Human Health", Germany, 2018.

Workshop presentation

[1] **L. Lan**, TDLAS for carbon dioxide measurement, *Sommerseminar 2016*, Munich, Germany, Jul. 1, 2016. (oral presentation)

[2] **L. Lan** and J. Chen, Environmental Sensing and Modeling, *TUM-IAS General Assembly 2017*, Burghausen, Germany, May. 4–5, 2017. (poster presentation)

[3] **L. Lan**, F. Toja-Silva, J. Chen, and S. Hachinger, Computational fluid dynamics (CFD) simulation of CO_2 emission from a thermal power plant in an urban environment, *TUM-IAS General Assembly 2017*, Burghausen, Germany, May. 4–5, 2017. (poster presentation)

Supervised Works

[1] Jagadeesh Kumar: Hardware Design for a TDLAS Measurement System (Aug.2017 – Feb. 2018)

[2] Nguyen Martin: Hardware Design and Testing of a VCSEL Laser Diode System (Apr. 2018 – Sep. 2018)